Functional and structural polypharmacology of indazole-based privileged ligands to tackle the undruggability of membrane transporters

Katja Stefan, Sachin Puri, Muhammad Rafehi, Ganesh Latambale, Maria Neif, Franziska Tägl, Nike Sophia Arlt, Zeinab Nezafat Yazdi, Éva Bakos, Xiang Chen, Bohan Zhang, Wouroud Ismail Al-Khalil, Hauke Busch, Zhe-Sheng Chen, Csilla Özvegy-Laczka, Vigneshwaran Namasivayam, Kapil Juvale, Sven Marcel Stefan

Research paper

Functional and structural polypharmacology of indazole-based privileged ligands to tackle the undruggability of membrane transporters

Katja Stefan [a,b,1], Sachin Puri [c,d,1], Muhammad Rafehi [e,f,g,1], Ganesh Latambale [c], Maria Neif [g], Franziska Tägl [g], Nike Sophia Arlt [g], Zeinab Nezafat Yazdi [h], Éva Bakos [h], Xiang Chen [i], Bohan Zhang [i], Wouroud Ismail Al-Khalil [g], Hauke Busch [j], Zhe-Sheng Chen [i], Csilla Özvegy-Laczka [h], Vigneshwaran Namasivayam [a,k,***] (ID), Kapil Juvale [c,**], Sven Marcel Stefan [a,b,l,*]

[a] University of Lübeck and University Medical Center Schleswig-Holstein, Lübeck Institute of Experimental Dermatology, Medicinal Chemistry and Systems Polypharmacology, Ratzeburger Allee 160, 23538, Lübeck, Germany
[b] University of Oslo and Oslo University Hospital, Department of Pathology, Rikshospitalet, Sognsvannsveien 20, 0372, Oslo, Norway
[c] SVKM's NMIMS, Shobhaben Pratapbhai Patel School of Pharmacy & Technology Management, V.L. Mehta Road, Vile Parle (W), Mumbai, 400056, India
[d] SVKM's NMIMS, School of Pharmacy & Technology Management, Plot no. B4, Green Industrial Park, Polepally SEZ, TSIIC, Jadcherla, Mahbubnagar, Dist. Telangana 509 301, Hyderabad, 509301, India
[e] University Hospital of Augsburg, Stenglinstr. 2, 86156 Augsburg, Germany
[f] Department of Medical Education Augsburg, Faculty of Medicine, University of Augsburg, Am Medizincampus 2, 86156, Augsburg, Germany
[g] University Medical Center Göttingen, Institute of Clinical Pharmacology, Robert-Koch-Str. 40, 37075, Göttingen, Germany
[h] Institute for Molecular Sciences, Research Centre for Natural Sciences, HUN-REN, Magyar tudósok krt. 2., H-1117, Budapest, Hungary
[i] St. John's University, College of Pharmacy and Health Sciences, Department of Pharmaceutical Sciences, New York City, New York, USA
[j] University of Lübeck and University Medical Center Schleswig-Holstein, Lübeck Institute of Experimental Dermatology, Medical Systems Biology, Ratzeburger Allee 160, 23538, Lübeck, Germany
[k] University of Bonn, Pharmaceutical Institute, Department of Pharmaceutical and Cellbiological Chemistry, An der Immenburg 4, 53121, Bonn, Germany
[l] Medical University of Lublin, Department of Biopharmacy, Chodzki 4a, 20-093, Lublin, Poland

ABSTRACT

Despite the significant roles of solute carrier (SLC) and ATP-binding cassette (ABC) transporters in human health and disease, most remain poorly characterized as intrinsic and/or xenobiotic ligands are unknown, rendering them as 'undruggable'. Polypharmacology, defined as the simultaneous engagement of multiple targets by a single ligand, offers a promising avenue for discovering novel lead compounds addressing these emerging pharmacological challenges – a major focus in contemporary medicinal chemistry. While common structural motifs among phylogenetically diverse proteins have been proposed to underlie polypharmacology through the concept of 'multitarget binding sites', a comprehensive analysis of these functional and structural aspects from a medicinal chemistry perspective has yet to be undertaken. In our study, we synthesized 65 distinct indazole derivatives and evaluated their activity across a broad biological assessment platform encompassing 17 specific and polyspecific SLC and ABC transporters. Notably, ten indazoles exhibited cross-target activity against challenging transporter targets associated with neurodegeneration (ABCA1), metabolic reprogramming (MCT4), and cancer multidrug resistance (ABCC10). Furthermore, molecular blind docking experiments and advanced binding site analyses revealed, for the first time, conserved binding motifs across monocarboxylate transporters (MCTs),

* Corresponding author. University of Lübeck and University Medical Center Schleswig-Holstein, Lübeck Institute of Experimental Dermatology, Medicinal Chemistry and Systems Polypharmacology, Ratzeburger Allee 160, 23538, Lübeck, Germany.
** Corresponding author. SVKM's NMIMS, Shobhaben Pratapbhai Patel School of Pharmacy & Technology Management, V.L. Mehta Road, Vile Parle (W), Mumbai, 400056, India.
*** Corresponding author. University of Lübeck and University Medical Center Schleswig-Holstein, Lübeck Institute of Experimental Dermatology, Medicinal Chemistry and Systems Polypharmacology, Ratzeburger Allee 160, 23538, Lübeck, Germany.
E-mail addresses: vigneshwaran.namasivayam@uksh.de, vnamasiv@uni-bonn.de (V. Namasivayam), kjuvale@gmail.com (K. Juvale), sven.stefan@uni-luebeck.de, sven.stefan@umlub.pl (S.M. Stefan).
[1] These authors contributed equally.

organic anion transporting polypeptides (OATPs), organic cation transporters (OCTs), and ABC transporters, characterized by specific and recurring residues of tyrosine, phenylalanine, serine, and threonine. These findings highlight not only the potential of polypharmacology in drug discovery but also provide insights into the structural underpinnings of ligand binding across membrane transporters.

Abbreviations

ABC	ATP-binding cassette	MPP$^+$	1-methyl-4-phenylpyridinium
ASP$^+$	4-(4-(dimethylamino)styryl)-*N*-methylpyridinium	MRP	multidrug resistance-associated protein
ATP	adenosine triphosphate	MTT	3-(4,5-dimethylthiazol-2-yl)-2,5-diphenyltetrazolium bromide
BCRP	breast cancer resistance protein	NAT	noradrenaline transporter
3-BP	3-bromopyruvate	25-NBD-cholesterol	25-[*N*-[(4-nitro-2,1,3-benzoxadiazol-7-yl) methylamino]-27-norcholesterol
calcein AM	calcein acetoxymethyl ester		
CHC	hydroxy-4-cyanocinammic acid	OAT	organic anion transporter
DAT	dopamine transporter	OATP	organic anion transporting polypeptide
DHPDS	6,8-dihydroxypyrene-1,3-disulfonate	OCT	organic cation transporter
EC$_{50}$	half-maximal reversal concentration	P-gp	P-glycoprotein
GI$_{50}$	half-maximal growth inhibition concentration	SEM	standard error of the mean
IC$_{50}$	half-maximal inhibition concentration	SERT	serotonin transporter
MCT	monocarboxylate transporter	SLC	solute carrier
MDR	multidrug resistance	SR101	sulforhodamine 101
MPC	mitochondrial pyruvate carrier	TLC	thin layer chromatography

1. Introduction

SLC and ABC transporters are biologically and physiologically important protein superfamilies that facilitate the absorption, distribution, and elimination of critical biochemicals and drugs in the human body. Furthermore, an emerging body of evidence pinpoints to an existing remote sensing and signaling network of SLC and ABC transporters, contributing to intra-tissue, inter-organ, and inter-organismal remote communication and homeostasis [1,2]. Dysfunction and/or dysregulation of SLC [3–5] and ABC [3,5,6] transporters are associated with highly prevalent human diseases of malignant [4,5], metabolic [4,6], or neurological [3,4] nature. Moreover, countless orphan diseases are connected to SLC and ABC transporter defects [7–16].

The targeted development of therapeutics addressing either a rescue of misfolded transporters (by 'correctors' or 'potentiators') or a functional modulation (by 'inhibitors' or 'activators') is hampered by three main factors:

(i) >450 and 48 SLC and ABC transporters exist, respectively; however, the majorities (>340/32) can be considered as 'undruggable targets' and cannot or only barely (≤10 compounds) be addressed by small-molecule modulators [17,18]. This lack of small-molecule modulators hinders not only to target the transporters of interest and medical relevance, but also impedes proper studies of their physiology and pathology (lack of tracers);

(ii) the emerging technological advances in cryo-EM provided many new insights into the structural aspects of SLC and ABC transporters. However, structural information on most human SLC and ABC transporters is still unavailable, hindering targeted structure-based approaches; and

(iii) the 'specificity paradigm' ('one drug-one target' concept) impeded the development of alternative approaches to address undruggable targets. While no doubts exist that highly potent and selective agents are desired to study the respective SLC or ABC transporters, polypharmacological agents are often neglected without using their strong potential with respect to the exploration of emerging but yet undruggable targets or the development of targeted polytherapeutics [19–21].

A small number of drugs and drug-like molecules were described in the literature to target several SLC and ABC transporters simultaneously [22–25], and thus, suggest common structural motifs that can be referred to as 'multitarget binding sites' [17,23,26–28]. These molecules are of various structural and pharmacological classes, such as benzbromarone (**1**) [22–25], erlotinib (**2**) [22,24,25], MK571 (**3**) [22,23,25], quercetin (**4**) [23–25,29], ritonavir (**5**) [22,25,30], and verapamil (**6**) [22–24], and Fig. 1 A–F visualizes these molecules. Conserved protein foldings ('superfolds') and binding sites ('supersites') have already been discovered at the very beginning of the structural exploration of the proteome [31–33]. Multitarget binding sites have been proposed specifically for ABC transporters earlier [17,23,26–28]. A computational pilot study gave first structural hints [23], and a functional study on non-human (*i.e.*, bacterial) ABC transporters allowed for the translation of polypharmacological agents between species [34]. An expansion to other protein families such as SLC transporters was concluded [28].

In order to explore membrane transporter-mediated polypharmacology and potential multitarget binding sites [17,23,26–28], we synthesized 65 structurally diverse indazole derivatives which were initially assessed against the SLC transporter monocarboxylate transporter 1 (MCT1, SLC16A1), as well as the ABC transporters ABCB1 (P-glycoprotein, P-gp), ABCC1 (multidrug resistance-associated protein 1, MRP1), and ABCG2 (breast cancer resistance protein, BCRP). Qualified hit molecules with rich polypharmacology were validated in an extended biological assessment platform comprising the rather specific monoamine transporters noradrenaline transporter (NAT), dopamine transporter (DAT), serotonin transporter (SERT; *SLC6A2–4*), as well as the rather polyspecific organic anion transporting polypeptides OATP1A2 (*SLCO1A2, SLC21A3*), OATP1B1 (*SLCO1B1, SLC21A6*), OATP1B3 (*SLCO1B3, SLC21A8*), OATP2B1 (*SLCO2B1, SLC21A9*) and organic cation transporters 1–3 (OCT1–3, *SLC22A1–3*). Additionally, the barely druggable ABC transporter ABCA1 [27,35] – a major key player and emerging drug target in Alzheimer's disease [27,36] – was included into this extended biological assessment platform to validate the privileged character of the compounds. Moreover, the efficacy of

selected indazoles against MCT1-, ABCB1-, ABCC1-, and ABCG2-expressing cells was assessed to evaluate whether their functional polypharmacology can be translated into a different bioactivity space. Furthermore, the efficacy against cells expressing the barely druggable transporters MCT4 [37,38] – a hot target in current commercial research on metabolic reprogramming in cancer [39] – and ABCC10 (MRP7) [40,41] – a major contributor to multidrug resistance (MDR) in cancer [42] – was determined. These functional analyses were complemented with structural experiments applying blind molecular docking and available cryo-EM structures of assessed SLC and ABC transporters to identify first evidence of multitarget binding sites amongst phylogenetically and functionally distinct membrane transporters.

2. Results

2.1. Rationale

In our effort to develop structurally and functionally novel antineoplastic agents, we recently discovered indole derivatives 22 (**7**) and 23 (**8**; both Fig. 2 A) as polypharmacological ligands which inhibited MCT1, ABCB1, ABCC1, and ABCG2 [43]. This finding made compounds **7–8** rare examples of synthesis-derived pan-SLC/ABC transporter modulators. On the other hand, the indole-like scaffold indazole is associated to polypharmacology against various drug targets [44,45], particularly membrane transporters [46]. These polypharmacological membrane transporter inhibitors include, for example, AB-PINACA [**9**; Fig. 2 B; OCT1, organic anion transporter 3 (OAT3, *SLC22A8*)] [47], bindarit (**10**; Fig. 2 C; MCT4) [38], brilanestrant (**11**; Fig. 2 D; OATP1B1, OATP1B3) [48,49], *N*-heteroaryl indazole 2 (**12**; Fig. 2 E; ABCG2) [50], indazole-3-carboxamine 11d (**13**; Fig. 2 F; SERT) [51], and lonidamide (**14**; Fig. 2 G; MCT1–2, MCT4, mitochondrial pyruvate carrier (MPC, *SLC54*) [52]. These examples showed not only biological activities of various indazoles against phylogenetically and functionally distinct membrane transporters, but also had certain substructural elements (*e. g.*, aliphatic-aromatic side chains, amide bonds, *etc.*), particularly at positions 1 and 3 of the indazole scaffold, that re-occurred between these indazoles and/or resembled structural elements of our previously reported polypharmacological indole derivatives [43]. Given the intense polypharmacology of indazoles and structural similarity between known membrane transporter inhibitors, we concluded this scaffold and known substituents as a suitable starting point for the exploration of membrane transporter-mediated polypharmacology and potential multitarget binding sites [17,23,26–28].

2.2. Chemistry

The entire synthesis route of indazoles is given in Fig. 3. The first two sets of indazoles (3-carboxamides) were synthesized as reported earlier [53] *via* acid-amine coupling giving 3-carboxamidoindazoles (step ii) followed by a nucleophilic substitution reaction of the corresponding 2-bromo-*N*-phenyl acetamide (set 1; compounds **15–22**) or 2-bromo-*N*-phenylpropanamide (set 2; compounds **23–58** [53]).

For the third set of molecules (3-phenyl derivatives), indazole 3-acrboxylic acid underwent decarboxylative bromination in excellent yields (step iii), followed by palladium-catalyzed Suzuki-Miyaura coupling to obtain 3-aryl-1*H*-indazoles (step iv). These were further reacted with 2-bromo-*N*-phenylacetamide to obtain *N*-alkylated-3-aryl-indazole derivatives (**59–68**) *via* a nucleophilic substitution reaction.

The fourth set of the compounds (3-carbohydrazides) derived from the reaction of indazole-3-carboxylic acid with substituted benzyl chloride/bromide providing *N*-benzylindazole-3-carboxylic acid (step v). Treatment with hydrazine hydrate resulted in indazole carbohydrazide derivatives (step vi), and reaction with substituted aromatic aldehydes yielded Schiff bases **69–79**.

It should be taken note that indazoles bear a tautomeric relationship between 1*H*- and 2*H*-indazole [45,54], posing a risk to obtain multiple products and/or minor yields of the intended products. However, three aspects need consideration:

(i) The equilibrium is tending to a large part toward the 1*H*-tautomer due to loss of aromaticity of the 2*H*-tautomer, making 1*H*-indazole irrespective of the substitution pattern at the indazole moiety thermodynamically much more stable [54];

(ii) the syntheses of 2-substituted indazoles has been documented in the literature, however, required rather harsh conditions [*e.g.*, trifluoromethanesulfonic acid, copper(II) triflate, *etc.*] [55], which has not been used within the present work;

(iii) the risk of obtaining unexpected and/or unintended side products can be approached by the application and combination of spectroscopic, spectrometric, and chromatographic techniques (*e.g.*, FTIR, ^{1}H NMR, ^{13}C NMR, MS, and HPLC). Clear spectra and chromatograms were obtained for all synthesized compounds (Supplementary Figs. 1–231), excluding the formation of side products, and thus, the formation of 2*H*-substituted indazoles even to a small extent.
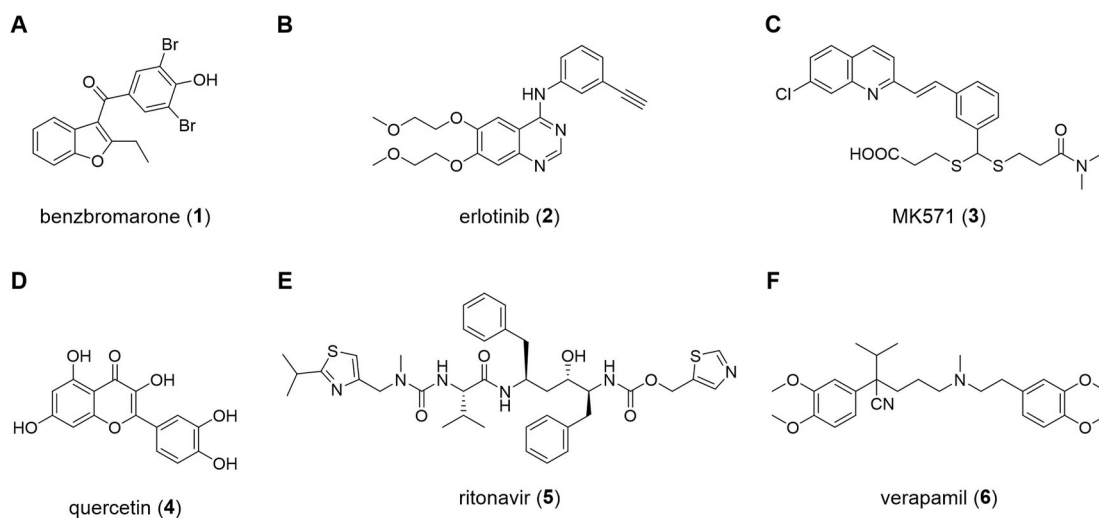
Fig. 1. Molecular formulae of known polypharmacological agents addressing several SLC and ABC transporters simultaneously; **A** benzbromarone (**1**) [22–25]; **B** erlotinib (**2**) [22,24,25]; **C** MK571 (**3**) [22,23,25]; **D** quercetin (**4**) [23–25,29]; and **E** ritonavir (**5**) [22,25,30]; **F** verapamil (**6**) [22–24].
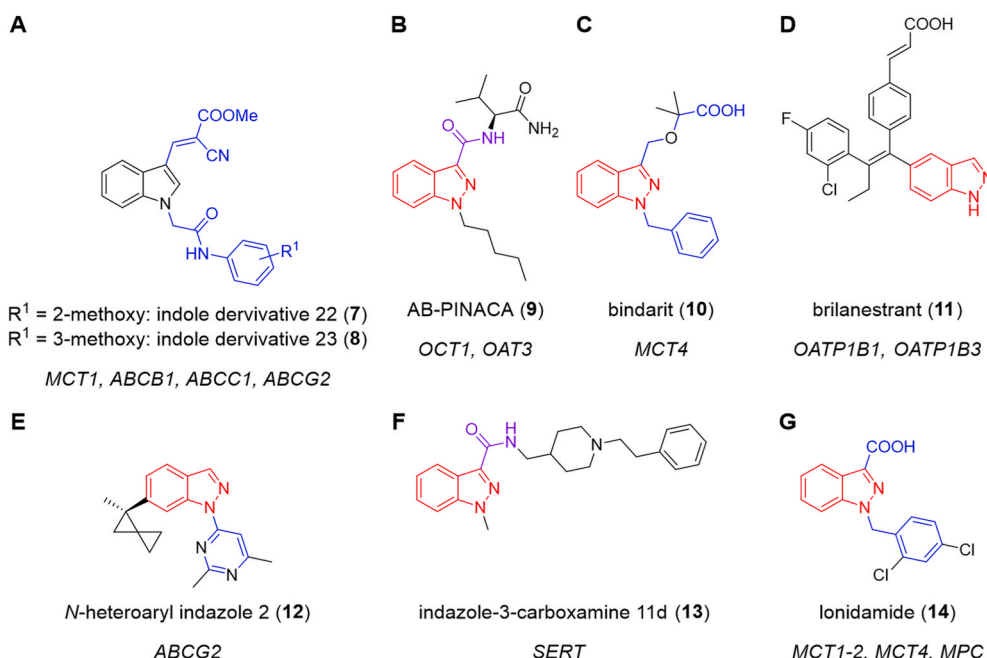
Fig. 2. Indazole(-like) compounds from the literature that demonstrated polypharmacology against phylogenetically and functionally distinct membrane transporters; **A** indole derivatives 22–23 (**7–8**) [43] found in our previous work to target MCT1, ABCB1, ABCC1, and ABCG2; **B** AB-PINACA (**9**) targeting OCT1 and OAT3 [47]; **C** bindarit (**10**) targeting MCT4 [38]; **D** brilanestrant (**11**) targeting OATP1B1 and OATP1B3 [48,49]; **E** *N*-heteroaryl indazole 2 (**12**) targeting ABCG2 [50]; **F** indazole-3-carboxamine 11d (**13**) targeting SERT [51]; and **G** lonidamide (**14**) targeting MCT1–2, MCT4, and mitochondrial pyruvate carrier (MPC, *SLC54*)] [52]. Red: Common indazole scaffold; blue: Structural commonalities between indole- and indazole-based polypharmacological membrane transporter inhibitors; violet: Structural commonalities amongst polypharmacological indazole-based membrane transporter inhibitors.

2.3. Biological evaluation

2.3.1. Functional assessment of indazoles against MCT1, ABCB1, ABCC1, and ABCG2

In our previous study, we discovered indole derivatives **7** and **8** (Fig. 2 A) as polypharmacological agents against MCT1, ABCB1, ABCC1, and ABCG2 [43]. We used the same assessment platform as starting point to extract a number of candidate molecules for further polypharmacological profiling. Bioactivities against MCT1, ABCB1, ABCC1, and ABCG2 were determined in 3-bromopyruvate (3-BP) [43], calcein acetoxymethyl ester (calcein AM) [17,26,28,43,56,57], daunorubicin [26,28,43,56,57], and pheophorbide A [17,26,28,43,56,57] assays using MCT1-expressing A-549 [43], ABCB1-expressing A2780/ADR [17,26,28,43,56,57], ABCC1-expressing H69AR [17,26,28,43,56,57], and ABCG2-expressing MDCK II BCRP [17,26,28,43,56,57] cells. Fig. 4 shows the entire screening results of the compounds tested against MCT1 (**A**), ABCB1 (**B**), ABCC1 (**C**), and ABCG2 (**D**). Compounds that reached an inhibition value of 20 % [+ standard error of the mean (SEM)] were further investigated with concentration-effect curves. Half-maximal inhibition concentration (IC$_{50}$) values were calculated and summarized in Supplementary Table 1.

In total, 41, 36, 16, and 40 of the 65 compounds inhibited MCT1, ABCB1, ABCC1, and ABCG2, respectively. Additionally, 13 compounds targeted MCT1 only. Furthermore, 5 and 9 inhibitors of ABCB1 and ABCG2, respectively, were identified which were selective over the other two evaluated ABC transporters, while 3 of the 5 and 9 each, respectively, also targeted MCT1. Moreover, we found 1, 16, and 1 dual ABCB1/ABCC1, ABCB1/ABCG2, and ABCC1/ABCG2 inhibitors, respectively, of which 1, 3, and 0, respectively, also targeted MCT1. Amongst the 65 evaluated compounds, 28 molecules were identified that targeted both transporter superfamilies. Markedly, the structural class of indazoles comprised 14 triple ABCB1/ABCC1/ABCG2 inhibitors (~21.5 % of evaluated compounds), of which 8 additionally targeted MCT1. Two of the other 6 triple inhibitors, compounds **31** and **32**, had a pronounced activity (~40–50 %) in the initial screening. Fig. 5 A shows

the substitution pattern of the hit molecules **15–16**, **18–20**, **53**, **57**, and **68** as well as **31–32**.

In order to confirm a concentration dependency of the observed effects, compounds **15–16**, **18–20**, **53**, **57**, and **68** as well as **31–32** were evaluated at various concentrations. The respective concentration-effect curves of the compounds determined in the 3-BP (MCT1), calcein AM (ABCB1), daunorubicin (ABCC1), and pheophorbide A assays (ABCG2) can be found in Supplementary Figs. 232–235. Representative concentration-effect curves of compound **57** as one of the most potent inhibitors can be seen in Fig. 5 B. As bioactivity measurements in transporter assays, particularly with respect to ABC transporters [43], depend on the tracers used, the hit compounds were tested in alternative assays, particularly, daunorubicin (ABCB1) [26,28,43], rhodamine 123 (ABCC1) [56], and Hoechst 33342 (ABCG2) [26,28,57–59] assays. Supplementary Figs. 236–238 provide the respective concentration-effect curves of the 10 hit compounds. Apart from compounds **53** and **68**, which showed no activity in the alternative ABCC1 assay, all compounds confirmed their bioactivity against ABCB1, ABCC1, and ABCG2 in the alternative assays. Fig. 5 C shows the corresponding concentration-effect curves of compound **57**. The IC$_{50}$ values of all active compounds are summarized in Supplementary Table 1, and Table 1 visualizes the bioactivities of hit compounds **15–16**, **18–20**, **53**, **57**, and **68** as well as **31–32**. Interestingly, the biological assessment revealed that compounds **20** and **57**, as well as **31–32** were so-called 'Class 7' molecules [17,22,23,26,28,57] (inhibiting each ABC transporter with IC$_{50}$ values of less than 10 μM). To this date, only 56 molecules with this ability are known [22,60,61].

2.3.2. Extended biological assessment platform for selected indazoles

A key feature of privileged ligands is polypharmacology beyond the initially addressed/drugged target landscape. Moreover, structural commonalities between SLC and ABC transporters should reflect in functional similarities of privileged ligands. In order to functionally explore the postulated multitarget binding sites [17,23,26–28], compounds **15–16**, **18–20**, **53**, **57**, and **68** as well as **31–32** were selected for
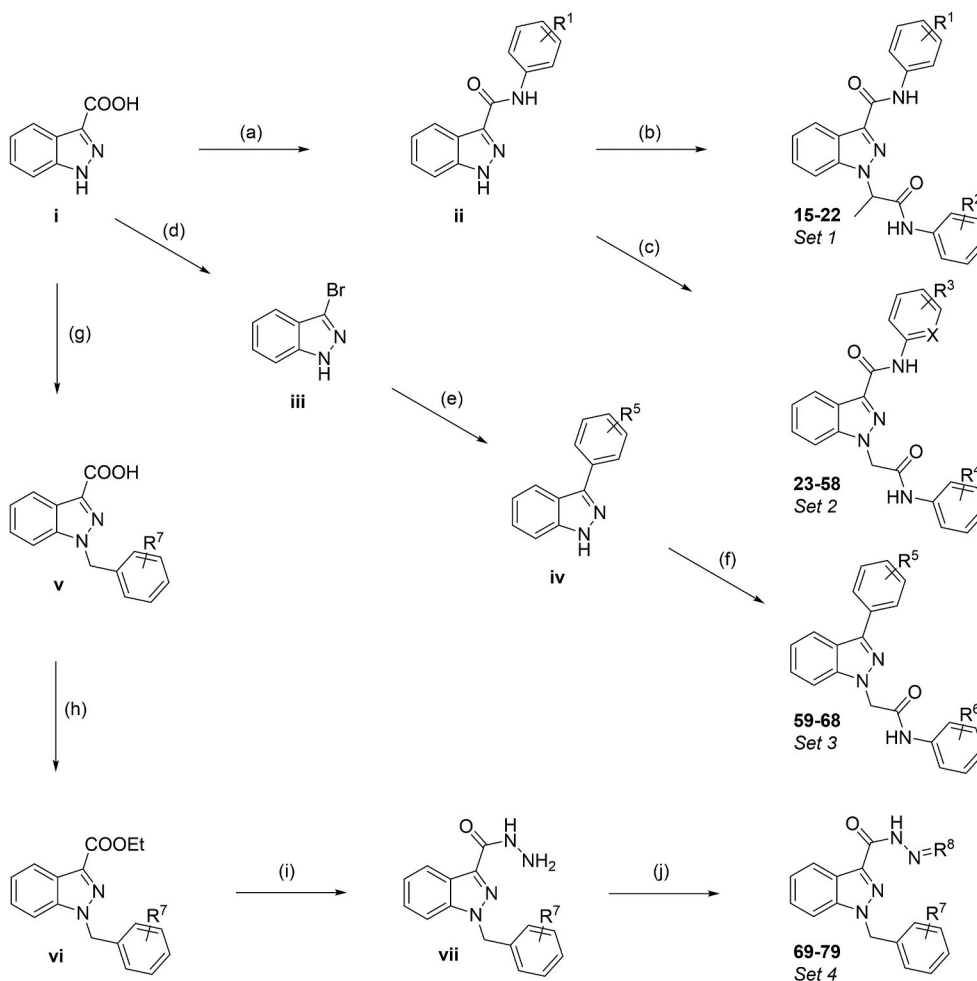
Fig. 3. Schematic representation of the conducted synthesis steps to obtain compound sets 1 (**15–22**), 2 (**23–58** [53]), 3 (**59–68**), and 4 (**69–79**): (a) starting compound **i** (1*H*-indazole-3-carboxylic acid), aryl amino derivative (1.1 eq.), 1-ethyl-3-(3-dimethylaminopropyl) carbodiimide hydrochloride (EDC · HCl; 1.2 eq.) hydroxybenzotriazole (HOBt; 1.2 eq.), DMF, reflux, 2 h, yield: ~80–90 %; (b) intermediate **ii**, substituted 2-bromo-*N*-aryl-propanamide (1.3 eq.), K$_2$CO$_3$ (1.5 eq.), DMF, rt, 4–6 h, yield: ~60–70 %; (c) intermediate **ii**, substituted 2-bromo-*N*-aryl-acetamide (1.3 eq.), K$_2$CO$_3$ (1.5 eq.), DMF, rt, 3–4 h, yield: ~80–90 %; (d) starting compound **i** (1*H*-indazole-3-carboxylic acid), *N*-bromo succinimide (NBS; 1.0 eq.), DMF, 0 °C–rt, 16 h, yield: 90 %; (e) intermediate **iii** (3-bromo-1*H*-indazole), substituted boronic acid derivative (1.2 eq.), CsCO$_3$ (2.5 eq.), Pd(PPh$_3$)$_4$ (5 mol-%) dioxane/water (3:1), reflux, 12 h, yield ~45–50 %; (f) intermediate **iv**, substituted 2-bromo-*N*-aryl-acetamide (1.3 eq.), K$_2$CO$_3$ (4.0 eq.), DMF, rt, 4–6 h, yield: ~70–80 %; (g) starting compound **i** (1*H*-indazole-3-carboxylic acid), benzyl chloride derivative (1.3 eq.), aqueous NaOH (1.0 eq.), reflux, 1–2 h, yield: ~90 %; (h) intermediate **v**, concentrated H$_2$SO$_4$, EtOH, reflux, 16 h, yield: 70 %; (i); intermediate **vi**, hydrazine · H$_2$O (1.0 eq.), EtOH, reflux, 16 h, yield: 73 %; (j) intermediate **vii**, aryl aldehyde derivative (1.0 eq.), GAA, EtOH, reflux, 16 h, yield: ~54–58 %.

a broader assessment of their polypharmacological profiles. The assessment platform included both the rather specific transporters NAT, DAT and SERT, as well as the rather polyspecific OATP1A2, OATP1B1, OATP1B3, OATP2B1, and OCT1–3 – which have independently been shown to be targeted by indazole-bearing compounds [38,47–52]. Additionally, we included ABCA1 into the extended biological assessment platform to have also a representative of barely druggable membrane transporters present. For this purpose, 1-methyl-4-phenylpyridinium (MPP$^+$; NAT, DAT, and SERT) [62], sulforhodamine 101 (SR101; OATP1A2) [63], 6,8-dihydroxypyrene-1,3-disulfonate (DHPDS; OATP1B1 and OATP1B3) [63], pyranine (OATP2B1) [63], 4-(4-(dimethylamino)styryl)-*N*-methylpyridinium (ASP$^+$; OCT1–3) [64], and 25-[*N*-[(4-nitro-2,1,3-benzoxadiazol-7-yl) methylamino]-27-norcholesterol (25-NBD-cholesterol; ABCA1) [35] assays were applied using either HEK293- [62,64] or A431-transfected [63,65] cells expressing the respective transporter of interest, or ABCA1-expressing J774A.1 cells [27,35].

All screening results can be obtained from Supplementary Fig. 239. While the compounds showed generally no activity against the monoamine transporters NAT, DAT, and SERT as well as against OCT1, they

were all very active against OATPs and moderately active against OCT2 (except for compound **20**), and compounds **57** and **32** showed additionally weak inhibitory activities against OCT3. Surprisingly, 4 of the 10 selected indazoles (**20**, **53**, **57**, and **68**; 40 %) demonstrated potent (IC$_{50}$ ≤ 20 μM) inhibition of ABCA1, for which before our recent report [35] only 14 inhibitors with activities in mostly triple-digit micromolar concentration ranges were known [27]. Interestingly, lead compound **57** demonstrated inhibition against all assessed transporters except for NAT, DAT, SERT, and OCT1. Supplementary Figs. 240–246 provides entire concentration-effect curves of hit molecules, and representative curves of lead compound **57** are depicted in Fig. 5 D–**E**. The IC$_{50}$ values of all active compounds are summarized in Supplementary Table 1, and Table 2 provides the bioactivities of hit compounds **15–16**, **18–20**, **53**, **57**, and **68** as well as **31–32**.

2.3.3. Efficacy of selected indazoles against MCT1-, ABCB1-, ABCC1-, and ABCG2-expressing cell lines

Privileged ligands project their polypharmacology not only toward a new/unknown target space but also toward a different/alternative bioactivity space. Functional MCT1, ABCB1, ABCC1, and ABCG2
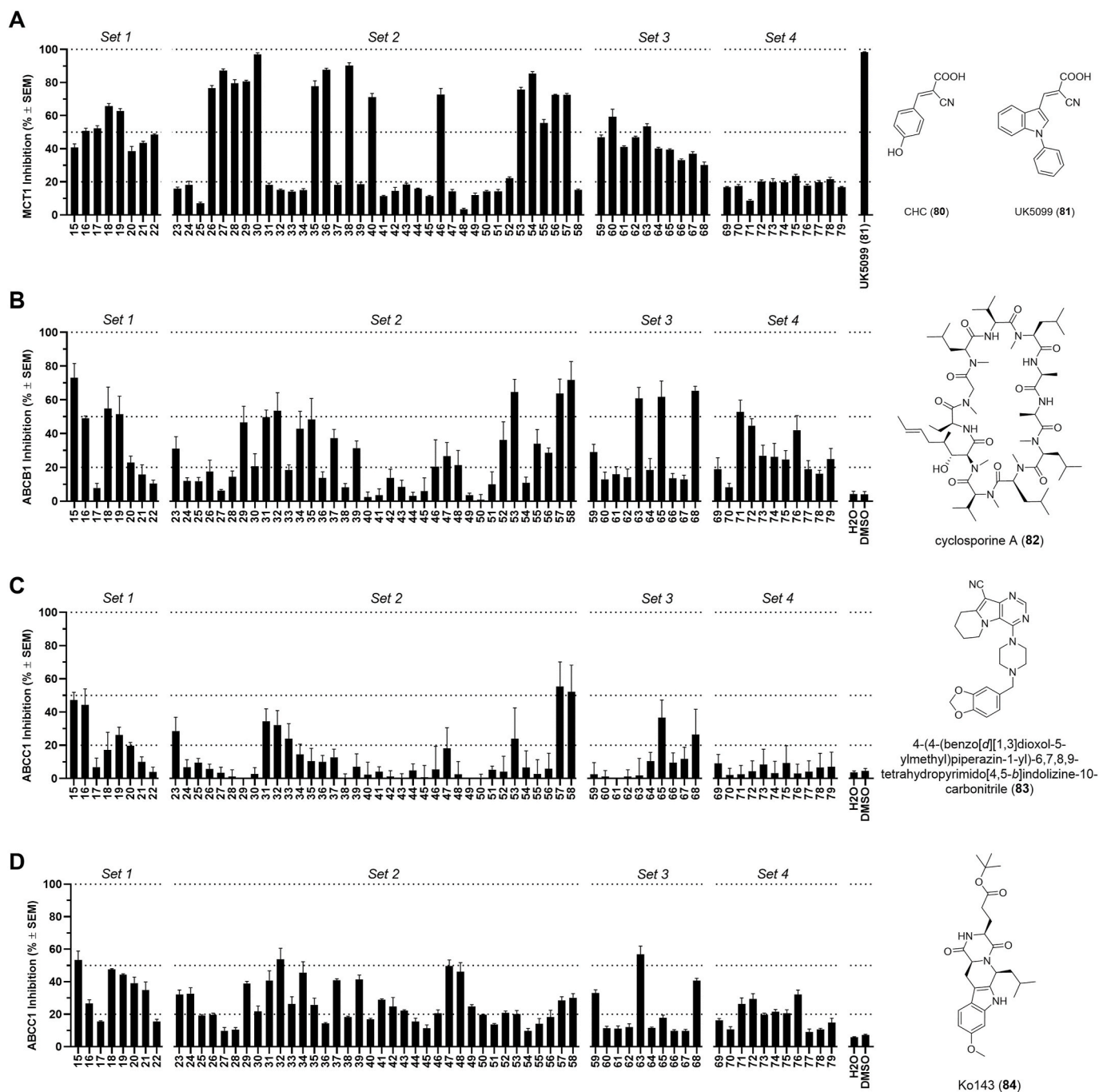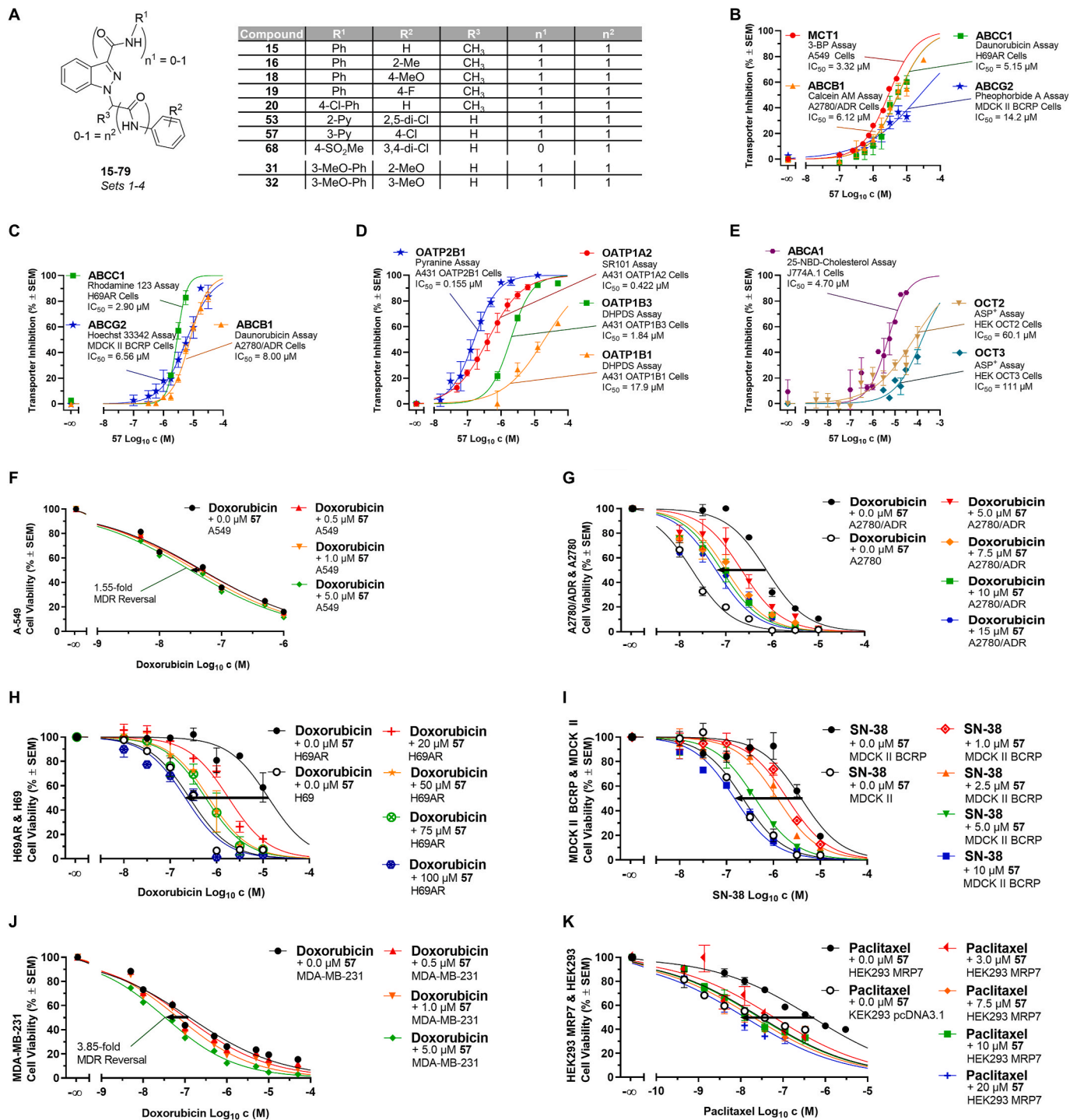
Fig. 4. Screening of compound sets 1 (**15–22**), 2 (**23–58**), 3 (**59–68**), and 4 (**69–79**). **A** The bioactivity of compounds **15–79** (5 μM) against MCT1 was assessed applying a functional 3-BP cell viability assay and MCT1-expressing A-549 cells. The effect of hydroxy-4-cyanocinammic acid [CHC (**80**); 100 %] and buffer medium (0 %) in the presence of 3-BP (50 μM) without test compounds were used for normalization purposes; additionally shown is the reference MCT1 inhibitor UK5099 (**81**). **B** The bioactivity of compounds **15–79** (10 μM) against ABCB1 was determined using a calcein AM assay and ABCB1-expressing A2780/ADR cells. The effects of 10 μM cyclosporine A (**82**; 100 %) and buffer medium (0 %) served as positive and negative controls, respectively. **C** The bioactivity of compounds **15–79** (10 μM) against ABCC1 was determined using a daunorubicin assay and ABCC1-expressing H69AR cells. The effects of 10 μM compound 4-(4-(benzo[d] [1,3]dioxol-5-ylmethyl)piperazin-1-yl)-6,7,8,9-tetrahydropyrimido [4,5-b]indolizine-10-carbonitrile (**83**; 100 %) and buffer medium (0 %) served as positive and negative controls, respectively. **D** The bioactivity of compounds **15–79** (10 μM) against ABCG2 was determined using a pheophorbide A assay and ABCG2-expressing MDCK II BCRP cells. The effects of 10 μM Ko143 (**84**; 100 %) and buffer medium (0 %) served as positive and negative controls, respectively. Shown are mean ± SEM values of at least three independent experiments.

inhibition may increase the susceptibility toward antineoplastic agents of cell lines expressing either of these transporters [43]. In order to validate compounds **15–16**, **18–20**, **53**, **57**, and **68** in alternative cellular models, we conducted 3-(4,5-dimethylthiazol-2-yl)-2,5-diphenyltetrazolium bromide-(MTT)-based MDR reversal assays applying MCT1-expressing A-549, ABCB1-expressing A2780/ADR,

ABCC1-expressing H69AR, and ABCG2-expressing MDCK II BCRP cells using the antineoplastic agents doxorubicin (MCT1 [43], ABCB1 [43], and ABCC1 [56]) and SN-38 (ABCG2 [58,59,66]). Compounds **31–32** were additionally assessed against ABCB1-, ABCC1-, and ABCG2-expressing cells.

Compounds **15**, **18**, **53**, and **57** slightly increased doxorubicin-

A. General structure and compound table:

Compound	R¹	R²	R³	n¹	n²
15	Ph	H	CH₃	1	1
16	Ph	2-Me	CH₃	1	1
18	Ph	4-MeO	CH₃	1	1
19	Ph	4-F	CH₃	1	1
20	4-Cl-Ph	H	CH₃	1	1
53	2-Py	2,5-di-Cl	H	1	1
57	3-Py	4-Cl	H	1	1
68	4-SO₂Me	3,4-di-Cl	H	0	1
31	3-MeO-Ph	2-MeO	H	1	1
32	3-MeO-Ph	3-MeO	H	1	1

(caption on next page)

Fig. 5. In-depth functional assessment of qualified indazoles against membrane transporters. **A** Generalized molecular structure of the 65 synthesized indazole derivatives including substitution patterns of the positions R^{1-3} and linkers n^{1-2} of hit molecules **15–16**, **18–20**, **53**, **57**, and **68** as well as **31–32**. **B** Concentration-effect curves of compound **57** against MCT1 (red circles), ABCB1 (orange triangles), ABCC1 (green squares), and ABCG2 (blue stars) determined in 3-BP, calcein AM, daunorubicin, and pheophorbide A assays, respectively, applying MCT1-expressing A-549, ABCB1-expressing A2780/ADR, ABCC1-expressing H69AR, and ABCG2-expressing MDCK II BCRP cells, respectively. **C** Concentration-effect curves of compound **57** against ABCB1 (orange triangles), ABCC1 (green squares), and ABCG2 (blue stars) determined in alternative daunorubicin, rhodamine 123, and Hoechst 33342 assays, respectively, applying ABCB1-expressing A2780/ADR, ABCC1-expressing H69AR, and ABCG2-expressing MDCK II BCRP cells, respectively. **D** Concentration-effect curves of compound **57** against OATP1A2 (red circles), OATP1B1 (orange triangles), OATP1B3 (green squares), and OATP2B1 (blue stars) determined in SR101, DHPDS, DHPDS, and pyranine assays, respectively, applying OATP1A2-, OATP1B1-, OATP1B3-, or OATP2B1-expressing A431 cells, respectively. **E** Concentration-effect curves of compound **57** against OCT2 (brown triangles), OCT3 (turquoise routes), and ABCA1 (violet hexagons) determined in either ASP^+ (OCT2–3) or 25-NBD-cholesterol (ABCA1) assays applying either OCT2- or OCT3-expressing HEK293 cells or ABCA1-expressing J774A.1 cells, respectively. **F** Concentration-dependent efficacy of lead compound **57** at 0.5 μM (dotted circles), 1.0 μM (dotted routes), and 5.0 μM (downward triangles) in combination with doxorubicin against MCT1-expressing A-549 cells. **G** Concentration-dependent efficacy of lead compound **57** at 5.0 μM (downward triangles), 7.5 μM (routes), 10 μM (squares), and 15 μM (hexagons) in combination with doxorubicin against ABCB1-expressing A2780/ADR cells. **H** Concentration-dependent efficacy of lead compound **57** at 20 μM (plus signs), 50 μM (stars), 75 μM (crossed circles), and 100 μM (crossed hexagons) in combination with doxorubicin against ABCC1-expressing H69AR cells. **I** Concentration-dependent efficacy of lead compound **57** at 1.0 μM (dotted routes), 2.5 μM (upward triangles), 5.0 μM (downward triangles), and 10 μM (squares) in combination with SN-38 against ABCG2-expressing MDCK II BCRP cells. **J** Concentration-dependent efficacy of lead compound **57** at 0.5 μM (dotted circles), 1.0 μM (dotted routes), and 5.0 μM (downward triangles) in combination with doxorubicin against MCT4-expressing MDA-MB-231 cells. **K** Concentration-dependent efficacy of lead compound **57** at 3.0 μM (leftward triangles), 10 μM (closed squares), and 20 μM (plus signs) in combination with doxorubicin against ABCC10-expressing HEK293 MRP7 cells. Data are expressed as mean ± SEM of at least three independent experiments; Dox = doxorubicin; Pac = paclitaxel.

mediated cancer cell toxicity in MCT1-expressing A-549 cells, however, compounds **16**, **19–20**, and **68** seemed to increase cell viability at higher concentrations (Supplementary Fig. 247). Such effects have been observed before [59] and may be caused by metabolic reprogramming or genetic changes that counteract the effect of cellular toxicity by MCT1 inhibition. Nevertheless, all compounds had a strong impact on cell viability at a concentration of 10 μM due to pyruvate and lactate deprivation as a result of MCT1 inhibition (Supplementary Fig. 248) [43]. Lead compound **57** showed the second largest potentiation of doxorubicin-mediated cancer cell toxicity which led to a 1.55-fold MDR reversal in MCT1-expressing A-549 cells (Fig. 5 F), which is an acceptable value considering potent MCT1-targeting MDR reversers [43]. To validate the found results, the compounds were also assessed in MTT-based cell viability assays at various concentrations in two MCT1-expressing cell lines, A-549 and MCF-7 [43], and Supplementary Figs. 249–250 show the individual concentration-effect curves of the tested compounds. Here, lead compound **57** had half-maximal growth inhibition (GI_{50}) values of 28.6 μM (A-549) and 10.8 μM (MCF-7) [53].

With respect to ABCB1, all evaluated compounds except for **20** and **68** could translate their ABCB1 inhibition into efficacy against ABCB1-expressing cells. The concentration-dependency of reversal of doxorubicin-mediated MDR by lead compound **57** is visualized in Fig. 5 G, and Supplementary Fig. 251 provides the concentration-effect curves of all MDR reversal assays using compounds **15–16**, **18–19**, **53**, and **57**, as well as **31–32**. Lead compound **57** sensitized ABCB1-expressing A2780/ADR cells by half at 4.67 μM (Supplementary Fig. 252 F), which is well in alignment of its IC_{50} values against ABCB1 [6.12 μM (calcein AM assay) and 8.00 μM (daunorubicin assay)]. Supplementary Fig. 252 shows the concentration-dependency of reversal of ABCB1-mediated MDR by all tested compounds.

Regarding ABCC1, all compounds were able to reverse ABCC1-mediated MDR against doxorubicin using ABCC1-expressing H69AR cells, although at much higher concentrations than against ABCB1. Supplementary Fig. 253 provides the entire set of concentration-effect curves of compounds **15–16**, **18–20**, **53**, **57**, and **68**, as well as **31–32**, and Fig. 5 H provides the concentration-effect curves of lead compound **57**. Its EC_{50} value of 6.86 μM (Supplementary Fig. 254 G) perfectly matches with its IC_{50} values [5.15 μM (daunorubicin assay) and 2.90 μM (rhodamine 123 assay)]. Supplementary Fig. 254 demonstrates concentration-dependency of reversal of ABCC1-mediated MDR for all evaluated compounds.

Concerning ABCG2, all evaluated compounds except for **16**, **20**, and **68** could reverse ABCG2-mediated MDR. Fig. 5 I shows the concentration-effect curves of SN-38 without and with different concentrations of compound **57**, while Supplementary Fig. 255 visualizes the concentration-effect curves of compounds **15**, **18–19**, **53**, and **57**, as

well as **31**. Lead compound **57** had an EC_{50} value of 1.05 μM as demonstrated in Supplementary Fig. 256 E. This value is > 13-times and > 5-times lower than the IC_{50} values of 14.2 μM (pheophorbide assay) and 6.56 μM (Hoechst 33342 assay), respectively. This effect can be explained by a higher intrinsic toxicity of compound **57** against MDCK II BCRP cells that adds up to its efficacy. Supplementary Fig. 256 demonstrates concentration-dependency of reversal of ABCG2-mediated MDR for all evaluated compounds. Supplementary Table 1 and Table 3 provide the efficacy values of hit compounds **15–16**, **18–20**, **53**, **57**, and **68** as well as **31–32**.

2.3.4. Efficacy of selected indazoles against MCT4-and ABCC10-expressing cell lines

Privileged ligands may not only translate between different bioactivity spaces (*i.e.*, functional assays *vs* efficacy assays) with respect to well-studied drug targets (*i.e.*, ABCB1, ABCC1, and ABCG2), but may also achieve this translation toward the undruggable or barely druggable target space. As a proof of concept, we assessed selected indazoles against two such barely druggable targets: MCT4 and ABCC10. These targets have sparked both commercial and academic research interests, however, the number of inhibitors shared with the scientific communities on public repositories is very minor [37,38,40,41].

All evaluated compounds increased doxorubicin-mediated cancer cell toxicity significantly stronger in MCT4-expressing MDA-MB-231 cells than in MCT1-expressing A-549 cells. Fig. 5 J visualizes the effect of lead compound **57** on doxorubicin-mediated cell toxicity in MDA-MB-231 cells, which was the strongest of all evaluated compounds (3.85-fold), and Supplementary Fig. 257 demonstrates the concentration-dependent efficacy of all evaluated compounds. Inhibition of MCT4 results in lactate overload and acidification of the cytosol with subsequent cell death [43]. This cell death of MDA-MB-231 cells could be achieved for all evaluated compounds (Supplementary Fig. 258) and the observed effects were also concentration-dependent (Supplementary Fig. 259). The strong MDR reversing capability of lead compound **57** reflected in considerable cell toxicity ($GI_{50} = 30.0$ μM) as already shown earlier [53].

Compounds **15–16**, **18–20**, **53**, **57**, and **68** as well as **31–32** were also tested for their capability to reverse ABCC10-mediated MDR in ABCC10-expressing HEK293 MRP7 cells, which was accomplished by compounds **16**, **18**, **20**, and lead compound **57** (Supplementary Fig. 260). Fig. 5 K highlights the MDR reversal capability of lead compound **57**; all concentrations used (3 μM–20 μM) almost entirely sensitized ABCC10-expressing HEK293 MRP7 cells toward the antineoplastic agent paclitaxel, and the EC_{50} was estimated to be ~0.3 μM (Supplementary Fig. 261). Table 4 summarizes all data obtained from these experiments.

Table 1
Activity values of hit compounds **15–16**, **18–20**, **53**, **57**, and **68** as well as **31–32** against MCT1, ABCB1, ABCC1, and ABCG2 determined in functional 3-BP (MCT1), calcein AM (ABCB1), daunorubicin (ABCB1 and ABCC1), rhodamine 123 (ABCC1), pheophorbide A (ABCG2), and Hoechst 33342 (ABCG2) assays. Data are expressed as mean $\pm$ SEM of at least three independent experiments; *n.e.* = no effect.

Compound	MCT1 3-BP (μM)	ABCB1 Calcein AM (μM)	ABCB1 Daunorubicin (μM)	ABCC1 Daunorubicin (μM)	ABCC1 Rhodamine 123 (μM)	ABCG2 Pheophorbide A (μM)	ABCG2 Hoechst 33342 (μM)
15	12.6 $\pm$ 0.6	1.58 $\pm$ 0.18	4.07 $\pm$ 0.23	9.95 $\pm$ 1.30	2.04 $\pm$ 0.29	13.0 $\pm$ 1.1	11.6 $\pm$ 1.9
16	6.76 $\pm$ 0.10	1.92 $\pm$ 0.29	5.39 $\pm$ 0.18	11.2 $\pm$ 1.56	3.67 $\pm$ 0.20	32.7 $\pm$ 1.7	34.1 $\pm$ 4.4
18	4.34 $\pm$ 0.03	2.49 $\pm$ 0.25	8.49 $\pm$ 0.45	8.93 $\pm$ 1.35	9.55 $\pm$ 0.54	27.1 $\pm$ 2.9	6.83 $\pm$ 0.94
19	4.49 $\pm$ 0.13	1.16 $\pm$ 0.23	7.00 $\pm$ 0.58	9.04 $\pm$ 1.08	3.94 $\pm$ 0.40	30.3 $\pm$ 4.5	5.62 $\pm$ 0.73
20	11.1 $\pm$ 0.5	7.57 $\pm$ 0.66	12.1 $\pm$ 1.0	5.48 $\pm$ 0.53	6.61 $\pm$ 0.73	7.89 $\pm$ 1.0	2.17 $\pm$ 0.26
53	1.89 $\pm$ 0.03	0.626 $\pm$ 0.090	1.74 $\pm$ 0.25	0.492 $\pm$ 0.207	*n.e.*	1.17 $\pm$ 0.10	1.03 $\pm$ 0.10
57	3.32 $\pm$ 0.40	6.12 $\pm$ 0.78	8.00 $\pm$ 0.39	5.15 $\pm$ 0.61	2.90 $\pm$ 0.14	14.2 $\pm$ 1.3	6.56 $\pm$ 0.87
68	16.6 $\pm$ 0.3	0.688 $\pm$ 0.069	1.06 $\pm$ 0.09	2.10 $\pm$ 0.46	*n.e.*	5.05 $\pm$ 0.57	1.43 $\pm$ 0.23
31	*n.e.*	1.56 $\pm$ 0.23	2.18 $\pm$ 0.26	2.19 $\pm$ 0.24	3.79 $\pm$ 0.34	1.66 $\pm$ 0.12	6.29 $\pm$ 0.89
32	*n.e.*	1.10 $\pm$ 0.11	1.43 $\pm$ 0.10	1.48 $\pm$ 0.20	2.66 $\pm$ 0.18	1.33 $\pm$ 0.19	2.07 $\pm$ 0.25

Table 2
Activity values of hit compounds **15–16**, **18–20**, **53**, **57**, and **68** as well as **31–32** against NAT, DAT, SERT, OATP1A2, OATP1B1, OATP1B3, OATP2B1, OCT1, OCT2, OCT3, and ABCA1 in functional MPP$^+$ (NAT, DAT, and SERT), SR101 (OATP1A2), DHPDS (OATP1B1 and OATP1B3), pyranine (OATP2B1), ASP$^+$ (OCT1–3), and 25-NBD-cholesterol (ABCA1) assays. Data are expressed as mean $\pm$ SEM of at least three independent experiments; *n.e.* = no effect.

Compound	NAT MPP$^+$ (μM)	DAT MPP$^+$ (μM)	SERT MPP$^+$ (μM)	OATP1A2 SR101 (μM)	OATP1B1 DHPDS (μM)	OATP1B3 DHPDS (μM)	OATP2B1 Pyranine (μM)	OCT1 ASP$^+$ (μM)	OCT2 ASP$^+$ (μM)	OCT3 ASP$^+$ (μM)	ABCA1 NBD-cholesterol (μM)
15	*n.e.*	*n.e.*	*n.e.*	1.20 $\pm$ 0.05	8.48 $\pm$ 0.74	1.78 $\pm$ 0.14	0.420 $\pm$ 0.060	*n.e.*	43.9 $\pm$ 5.4	*n.e.*	*n.e.*
16	*n.e.*	*n.e.*	*n.e.*	0.710 $\pm$ 0.070	6.95 $\pm$ 0.79	0.788 $\pm$ 0.035	0.170 $\pm$ 0.033	*n.e.*	51.3 $\pm$ 10.8	*n.e.*	*n.e.*
18	*n.e.*	*n.e.*	*n.e.*	0.991 $\pm$ 0.082	7.58 $\pm$ 0.63	3.36 $\pm$ 0.35	0.387 $\pm$ 0.015	*n.e.*	118 $\pm$ 16	*n.e.*	*n.e.*
19	*n.e.*	*n.e.*	*n.e.*	1.01 $\pm$ 0.09	6.42 $\pm$ 0.31	2.92 $\pm$ 0.08	0.265 $\pm$ 0.011	*n.e.*	66.0 $\pm$ 9.3	*n.e.*	*n.e.*
20	*n.e.*	*n.e.*	*n.e.*	7.93 $\pm$ 1.45	13.3 $\pm$ 1.2	12.8 $\pm$ 0.9	0.402 $\pm$ 0.034	*n.e.*	*n.e.*	*n.e.*	42.2 $\pm$ 3.9
53	*n.e.*	*n.e.*	*n.e.*	1.32 $\pm$ 0.19	16.8 $\pm$ 1.8	14.1 $\pm$ 2.6	0.167 $\pm$ 0.028	*n.e.*	50.3 $\pm$ 8.1	*n.e.*	13.0 $\pm$ 0.8
57	*n.e.*	*n.e.*	*n.e.*	0.422 $\pm$ 0.08	17.9 $\pm$ 2.5	1.84 $\pm$ 0.04	0.155 $\pm$ 0.022	*n.e.*	60.1 $\pm$ 8.4	111 $\pm$ 18	4.70 $\pm$ 0.69
68	*n.e.*	*n.e.*	*n.e.*	2.18 $\pm$ 0.24	14.8 $\pm$ 1.8	11.2 $\pm$ 0.7	0.826 $\pm$ 0.101	*n.e.*	56.8 $\pm$ 5.9	*n.e.*	2.97 $\pm$ 0.45
31	*n.e.*	*n.e.*	*n.e.*	0.237 $\pm$ 0.033	5.66 $\pm$ 0.56	1.80 $\pm$ 0.08	0.124 $\pm$ 0.017	*n.e.*	11.8 $\pm$ 2.2	76.4 $\pm$ 11.2	*n.e.*
32	*n.e.*	*n.e.*	*n.e.*	0.420 $\pm$ 0.038	4.96 $\pm$ 0.21	2.29 $\pm$ 0.09	0.583 $\pm$ 0.073	*n.e.*	20.8 $\pm$ 1.2	*n.e.*	*n.e.*

2.4. Computational analyses

Compound **57** showed broad biological activity against both the initial and extended sets of membrane transporters assessed. The activity values ranged consistently between single-digit- and sub-micromolar concentrations [except for ABCG2 and OATP1B1 (low double-digit micromolar concentrations), OCT2 (moderately high double-digit micromolar concentration), and OCT3 (low triple-digit micromolar concentration). Lead compound **57** was additionally able to translate its functional activity into efficacy against cell lines expressing the respective transporters, and the calculated EC$_{50}$ values mostly matched with the results from the functional assays. Strikingly, compound **57** projected its polypharmacology toward the undruggable or barely druggable target space, *i.e.*, ABCA1, MCT4, and ABCC10. Its broad polypharmacology and apparent inherent character of a privileged ligand interconnecting phylogenetically and functionally distant protein targets suggested functional commonalities between ABC and SLC transporters of various subfamilies, and supported the notion of the postulated multitarget binding sites [17,23,26–28]. Thus, we performed blind molecular docking with compound **57** using recently published

Table 3
Efficacy values of hit compounds **15–16**, **18–20**, **53**, **57**, and **68** as well as **31–32** determined in MCT1-, ABCB1-, ABCC1-, and ABCG2-expressing A-549, A2780/ADR, H69AR, and MDCK II BCRP cells, respectively, provided as folds reversal compared to doxorubicin treatment alone (A-549, MCT1), half-maximal growth inhibition concentrations (GI$_{50}$; A-549, MCT1), and half-maximal reversal concentrations (EC$_{50}$; A2780/ADR, ABCB1; H69AR, ABCC1; and MDCK II BCRP, ABCG2). Data are expressed as mean $\pm$ SEM of at least three independent experiments; *n.e.* = no effect; *n.t.* = not tested.

| Compound	MCT1 Reversal (Fold)	A-549 GI$_{50}$ (μM)	MCF-7 GI$_{50}$ (μM)	ABCB1 EC$_{50}$ (μM)	ABCC1 EC$_{50}$ (μM)	ABCG2 EC$_{50}$ (μM)
15	1.69 $\pm$ 0.02	7.87 $\pm$ 0.06	11.5 $\pm$ 0.2	3.83 $\pm$ 0.46	6.84 $\pm$ 0.79	0.504 $\pm$ 0.091
16	*n.e.*	17.4 $\pm$ 0.1	14.2 $\pm$ 0.1	3.89 $\pm$ 0.34	13.4 $\pm$ 2.5	*n.e.*
18	1.50 $\pm$ 0.03	15.8 $\pm$ 0.2	7.88 $\pm$ 0.09	4.75 $\pm$ 0.42	9.64 $\pm$ 1.42	0.939 $\pm$ 0.033
19	*n.e.*	12.7 $\pm$ 0.2	11.8 $\pm$ 0.1	4.39 $\pm$ 0.36	6.60 $\pm$ 1.74	1.95 $\pm$ 0.51
20	*n.e.*	11.7 $\pm$ 0.4	10.4 $\pm$ 0.1	*n.e.*	12.3 $\pm$ 1.8	*n.e.*
53	1.35 $\pm$ 0.03	37.1 $\pm$ 0.6	*n.t.*	0.0895 $\pm$ 0.0580	33.1 $\pm$ 10.3	0.326 $\pm$ 0.072
57	1.55 $\pm$ 0.01	28.6 $\pm$ 0.3	10.8 $\pm$ 0.5	4.67 $\pm$ 0.59	6.86 $\pm$ 0.88	1.05 $\pm$ 0.18
68	*n.e.*	8.14 $\pm$ 0.73	8.46 $\pm$ 0.27	*n.e.*	3.15 $\pm$ 0.92	0.604 $\pm$ 0.047
31	*n.t.*	*n.t.*	*n.t.*	3.34 $\pm$ 0.22	5.53 $\pm$ 1.69	0.603 $\pm$ 0.047
32	*n.t.*	*n.t.*	*n.t.*	2.01 $\pm$ 0.28	8.55 $\pm$ 2.02	*n.e.*

Table 4
Efficacy values of hit compounds **15–16**, **18–20**, **53**, **57**, and **68** as well as **31–32** against MCT4- and ABCC10-expressing MDA-MB-231 and HEK293 MRP7 cells, respectively, provided as folds reversal compared to doxorubicin treatment alone (MDA-MB-231; MCT4), GI_{50} values (MDA-MB-231; MCT4), and EC_{50} values (HEK293 MRP7; ABCC10). Data are expressed as mean $\pm$ SEM of at least three independent experiments. *n.e.* = no effect; *n.t.* = not tested.

Compound	MCT4 Reversal (Fold)	MDA-MB-231 GI_{50} (μM)	ABCC10 EC_{50} (μM)
15	3.24 ± 0.00	*n.t.*	*n.e.*
16	2.66 ± 0.04	*n.t.*	$\sim$0.3
18	2.91 ± 0.02	22.7 ± 0.1	$\sim$0.3
19	2.77 ± 0.06	21.5 ± 0.2	*n.e.*
20	2.12 ± 0.01	23.7 ± 0.2	$\sim$0.3
53	3.52 ± 0.01	29.9 ± 0.2	*n.e.*
57	3.85 ± 0.02	30.0 ± 0.4	$\sim$0.3
68	2.72 ± 0.05	7.99 ± 0.42	*n.e.*
31	*n.t.*	*n.t.*	*n.e.*
32	*n.t.*	*n.t.*	*n.e.*

cryo-EM structures of tested transporters (*i.e.*, MCT1 [67], ABCB1 [68], ABCC1 [69], ABCG2 [70], OATP1B1 [71], OATP1B3 [72], OCT2 [73], OCT3 [74], and ABCA1 [75] to explore potential structural commonalities as performed earlier [23].

Visualization of the protein structures revealed the transmembrane helices (TMs) as the minimal consensus features between the two structurally distinct superfamilies of SLC and ABC transporters (Fig. 6 A). Thus, we decided to use this space spanning the membrane bilayer as grid box for molecular docking as most studies on transporters found binding sites in these domains [23]. By superimposing the top ranking docking poses of compound **57** from each blind docking experiment it could be shown that, at a first glance, the individual putative binding poses seemed to be different for each target protein (Fig. 6 B). However, commonalities in the interaction patterns could be observed when grouping the target proteins into the subgroups (i) MCT1, (ii) ABCs, (iii) OATPs, and (iv) OCTs:

(i) Compound **57** possibly interacted with the phenylalanine residues Phe 278, Phe 367, and Phe 375 of MCT1 through hydrophobic interactions, while the ligand pose could be stabilized *via* the tyrosine residues Tyr 34, Tyr 70, and Tyr 266 through π-π stacking. In addition, the serines Ser 154 and Ser 371 potentially provided hydrogen bonds for ligand interaction. Fig. 6 C and Supplementary Fig. 262 A–C show the possible localization of compound **57** within MCT1, while Supplementary Fig. 262 D provides a detailed potential interaction diagram;

(ii) similar to MCT1, phenylalanine residues in ABCB1 (Phe 343), ABCC1 (Phe 594), ABCG2 (Phe 439), and ABCA1 (Phe 755) provided possible hydrophobic interactions as well as π-π stacking (ABCA1 only). The presence of phenylalanine in all four target proteins suggests that this residue plays a critical role in stabilizing the hydrophobic regions of the ligand within the ABC transporter family. Further π-π stacking could be mediated by tyrosine residues particularly present in ABCB1 (Tyr 950) and ABCA1 (Tyr 650). An identical amino acid at this position is lacking for ABCC1 and ABCG2, however, the combination of other phenylalanine (Phe 340 and Phe 439, respectively) and serine/threonine residues (Thr 1240 and Ser 440, respectively) may compensate the lacking tyrosine residues. Furthermore, serine and threonine residues seem to promote (water-mediated) H-bond interactions between compound **57** and ABCB1 (Ser 344), ABCC1 (Ser 373/Thr 1241), ABCG2 (Ser 535/Thr 538), and ABCA1 (Ser 1772), which for their part indicated a conserved mechanism for polar stabilization of (multitarget) ligands across this group of transporters. Fig. 6 D as well as Supplementary Figs.
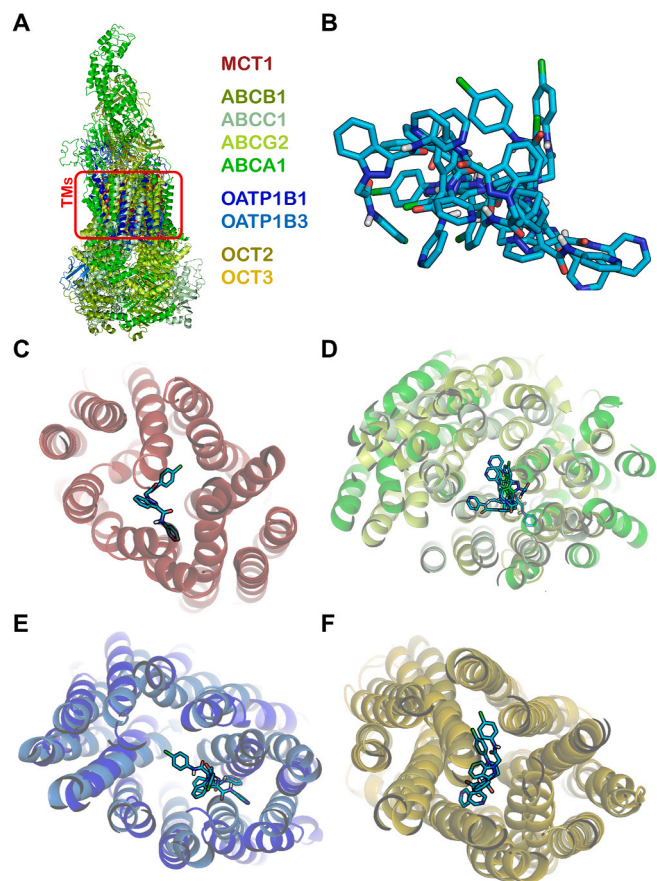
Fig. 6. Blind molecular docking of lead compound **57** using available cryo-EM structures of human MCT1 [67] (PDB ID 6LZ0), human ABCB1 [68] (PDB ID 7O9W), bovine ABCC1 [69] (PDB ID 8F4B), human ABCG2 [70] (PDB ID 8BHT), human OATP1B1 [71] (PDB ID 8K6L), human OATP1B3 [72] (PDB ID 8PG0), human OCT2 [73] (PDB ID 8ET9), human OCT3 [74] (PDB ID 7ZH6), and human ABCA1 [75] (PDB ID 7TDT). **A** Superimposed protein structures of analyzed membrane transporters outlining the minimal consensus features [transmembrane helices (TMs); red: grid box used for blind molecular docking]. **B** Superimposed top ranking docking poses of compound **57** as obtained in individual docking experiments. Additionally shown are the possible localizations of compound **57** within MCT1 (**C**), ABCs (**D**), OATPs (**E**), and OCTs (**F**).

263 A–C, 264 A–C, 265 A–C, and 266 A–C show the possible localizations of compound **57** within the assessed ABC transporters ABCB1, ABCC1, ABCG2, and ABCA1, respectively, while Supplementary Figs. 263 D, 364 D, 365 D, and 366 D provide detailed potential interaction diagrams;

(iii) in agreement to our observations with respect to MCT1 and ABC transporters, potential phenylalanine interactions between the ligand and OATP1B1 (Phe 356) and OATP1B3 (Phe 352) may stabilize compound **57**'s hydrophobic regions with aromatic π-π stacking and hydrophobic interactions, respectively. Particularly possible hydrophobic interactions with tyrosine residues in OATP1B1 (*i.e.*, Tyr 352 and Tyr 422) and OATP1B3 (*i.e.*, Tyr 425, Tyr 537, and Tyr 625) were pronounced in our docking studies, assigning tyrosine a general key role in (multitarget) ligand recognition between both transporter superfamilies. Interestingly, the glutamine residue Gln 541 is a highly conserved amino acid in both OATP1B1 and OATP1B3 that possibly formed polar interactions with compound **57**. Although glutamines have not been found as possible interaction partners in the other

transporter groups, the glutamines in OATPs may replicate a conserved H-bond interaction also found for MCT1 and ABC transporters. Fig. 6 E as well as Supplementary Figs. 267 A–C and 268 A–C show the possible localizations of compound **57** within OATP1B1 and OATP1B3, while Supplementary Figs. 267 D and 268 D provide detailed potential interaction diagrams;

(iv) finally, similar to the putative interactions found for MCT1, ABC transporters, and OATPs, we were able to identify recurring interaction patterns with phenylalanines, tyrosines, and serines/ threonines. The phenylalanine residues Phe 447 (OCT2) and Phe 450 (OCT3) showed aromatic π-π stacking and hydrophobic interactions, respectively. Additional phenylalanine residues (OCT2: Phe 33, Phe 160, Phe 245; OCT3: Phe 32, Phe 36, Phe 165, Phe 250) are present in the binding pocket providing a more hydrophobic environment. Furthermore, the tyrosine residues Tyr 362 (OCT2) and Tyr 454 (OCT3) potentially exhibited both hydrophobic and/or π-π stacking interactions with compound **57**. Finally, similar to MCT1 and ABC transporters, both serines and threonines possibly formed H-bonds promoting polar interactions between OCT2 (Thr 444) and OCT3 (Thr 447 or Thr 251) and compound **57**. Fig. 6 F as well as Supplementary Figs. 269 A–C and 270 A–C show the possible localizations of compound **57** within OATP1B1 and OATP1B3, while Supplementary Figs. 269 D and 270 D provide detailed potential interaction diagrams.

In summary, our comprehensive docking analyses revealed several amino acids, particularly phenylalanines, tyrosines, serines, and threonines scattered within the various binding pockets of the different transporters (Fig. 7). We could identify 6 amino acid groups that consisted of three identical and/or similar amino acids with each amino acid belonging to a different transporter that mediated the same or similar putative interactions between compound **57** and the respective transporters. The essentially around the entire molecular structure of compound **57** located amino acid groups strongly suggest that these are part of the proposed multitarget binding sites [17,23,26–28] between functionally and/or phylogenetically distant membrane transporters.

3. Discussion and conclusions

Many SLC and ABC transporters are associated with both prevalent [3–6] and orphan human diseases [7–16], such as the herein investigated ABC transporters [3,5,6], OATPs [76], and OCTs [77–80]. However, the vast majority of these disease-modifying proteins are undruggable (SLCs: ≫70 %; ABCs: ≫60 %), as no modulators (*e.g.*, inhibitors, activators, partial modulators, correctors, potentiators, stabilizers, *etc.*) and/or intrinsic substrates are known [17,18]. In between are targets for which some knowledge has accumulated and a modest number of modulators is available. However, even in these cases, opportunity space is limited, either due to the difficulty to identify (potent) modulators (*e.g.*, ABCA1 [27,35] and ABCC10 [40,41]), or the simply limited number of reports available to the public (*e.g.*, MCT4 [37,38]). Reasons for undruggability may be insufficient medical data (lack of evidence that a target is associated to a disease-of-interest, outlining it as not worth investigating), technical challenges arising from the target assessment pipeline (lack of suitable high-throughput assaybility), or simply lack of resources (funding, time, personnel) that ultimately lead to a neglected target space – and a lack of proper studies of its physiology and role in human health and disease. Apart from classical medicinal chemistry workflows (target identification, hit identification, and lead optimization in the context of the 'specificity paradigm'), new approaches and strategies are necessary to identify new starting points in drug development and enrich the medicinal chemistry repertoire to tackle target undruggability [19–21,81].

It is known that proteins even of phylogenetic distance share common structural motifs ('superfolds') and attract common sets of ligands ('privileged ligands'/'supersites') [31–33]. From a structural perspective, particularly undruggable targets are unknown, hampering structure-based drug design approaches. Polypharmacology bears the chance to use molecular-structural features ('superpatterns' [21]) of multitarget agents to particularly address 'supersites' ('multitarget binding sites' [17,23,26–28]). Preliminary work has demonstrated that particularly indazole may be an optimal scaffold to exert polypharmacology against SLC and ABC transporters [43,52]. The aim of the present work was to functionally explore indazole [38,44–52] as privileged scaffold of the polypharmacolome [21] of SLC and ABC transporters.
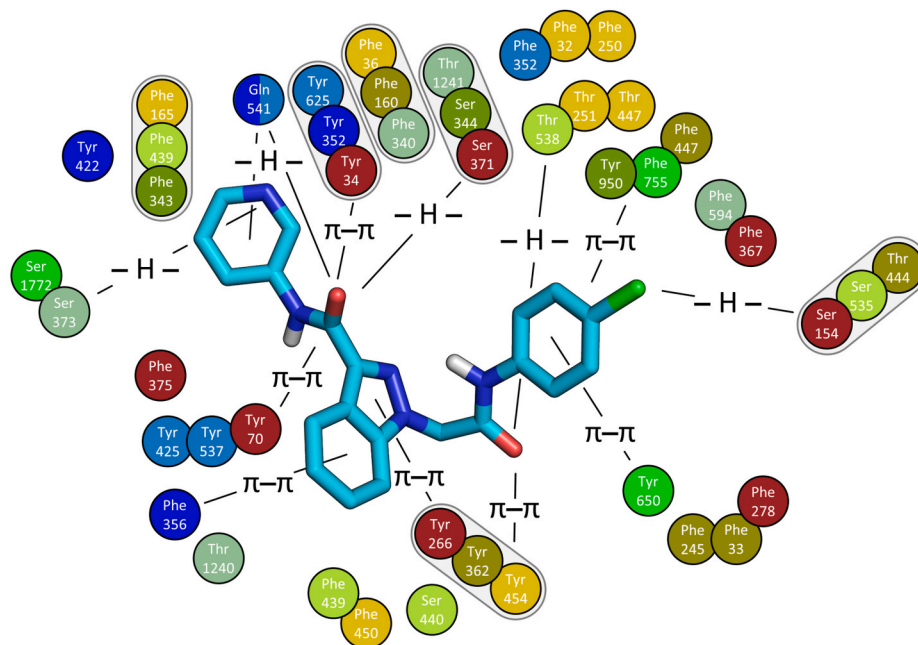

Fig. 7. Common potential interactions between compound **57** and amino acids of the analyzed transporters; grey zones: suggested amino acids as part of the proposed multitarget binding sites amongst membrane transporters [17,23,26–28].

On average, 51.2 % of the within this work synthesized and evaluated 65 indazoles targeted the initial transporters assessed (MCT1: 63.1 %; ABCB1: 55.4 %; ABCC1: 24.6 %; ABCG2: 61.5 %). These hit rates are comparably high considering other medicinal chemistry works, even for computational models that systematically harness molecular-structural dependencies between small-molecules and target structures [17,28, 57]. These initial results confirmed that indazoles are pharmacologically rich, particularly considering membrane transporters [38,44–52]. *Vice versa*, the rate for the identification of selective agents (at least selective over the herein assessed transporters) was rather low (MCT1: 21.5 %; ABCB1: 3.08 %; ABCC1: 0.00 %; ABCG2: 9.23 %; average: 8.45 %), and only 5 compounds (*i.e.*, **25**, **44**–**45**, **51**, **70**; 7.69 %) were found inactive. In total, 43.1 % of the compounds targeted both superfamilies of the initially assessed transporters, and 12.3 % addressed all targets of the initial assessment. The latter number seems low in the context of multitargeticity as outlined above, however, it needs to be considered that four different targets had to be addressed (with in part distinct ligand preferences).

We selected 10 molecules with desired and rich polypharmacological profiles, 8 of which targeted all 4 initially assessed transporters with considerable potency and further two showed extraordinary inhibitory activity ($IC_{50} < 10$ μM) in the context of triple ABCB1, ABCC1, and ABCG2 inhibition. To this date, only 56 molecules with this ability are known [22,60,61], and the structural, molecular, and functional dependencies are in focus of current investigations to which indazoles contribute substantially.

These 10 molecules, compounds **15**–**16**, **18**–**20**, **53**, **57**, **68** as well as **31**–**32**, inhibited on average 51.0 % of the extended biological assessment platform (NAT: 0.00 %; DAT: 0.00 %; SERT: 0.00 %; OATP1A2: 100 %; OATP1B1: 100 %; OATP1B3: 100 %; OATP2B1: 100 %; OCT1: 0 %; OCT2: 90 %; OCT3: 20 %). Two aspects are worth highlighting.

(i) the hit rate is similar to the overall hit rate of all 65 indazoles against the initial targets MCT1, ABCB1, ABCC1, and ABCG2. Considering that the number of tested compounds has been drastically reduced (65 → 10), the extended target landscape is functionally and entirely different (MCTs & ABCs → OATPs & OCTs), and the number of overall targets – despite having increased to 14 – is still minor compared to the entire SLC (>450) and ABC (48) transporter proteomes, the hit rate is comparably high;

(ii) interestingly, indazoles projected their polypharmacology mostly toward polyspecific transporters (*i.e.*, ABCB1, ABCC1, ABCG2, OATP1A2, OATP1B1, OATP1B3, OATP2B1), while specific transporters (*i.e.*, NAT, DAT, and SERT) were not affected. The monoamine transporters NAT, DAT, and SERT do not belong to the 'major facilitator superfamily' to which MCTs, OATPs, and OCTs belong, which may be one reason why the highly specific MCTs were inhibited by indazoles while the specific monoamine transporters were not. These findings certainly do not mean that the proposed multitarget binding sites [17,23,26–28] do not exist; however, it became apparent that the opportunity space within the polypharmacolome cannot be entirely explored given the structural limitation of the assessed targets and the molecular limitation stemming from the rather homogenous indazole derivatives. Thus, broader functional assessment of compounds in larger assessment platforms are necessary to completely decipher the role of polypharmacology in medicinal chemistry.

Strikingly, the selected indazoles were able to project their polypharmacology toward barely druggable targets, *i.e.*, ABCA1 (20, 53, 57, and 68; hit rate: 40.0 %), MCT4 (**15**–**16**, **18**–**20**, **53**, **57**, and **68**; hit rate: 80.0 %) and ABCC10 (16, 18, 20, and 57; hit rate: 40.0 %). These findings demonstrated that small-molecules specifically designed to be polypharmacological can address particularly undruggable or barely druggable transporters for which (almost) no small-molecule

modulators are known and/or available to the public [27,35,37,38,40, 41]. The resultant activity values particularly with respect to ABCA1 ($IC_{50} < 20$ μM) and ABCC10 ($EC_{50} \ll 1$ μM) stood out in the literature context of these transporters. Specifically, compound 57 addressed most assessed transporters (14 of 17; overall hit rate: 82.7 %) and therefore represents an excellent template molecule for ongoing functional, but also structural work to assess the polypharmacolome of membrane transporters and other protein classes (*e.g.*, tyrosine kinases, G-protein coupled receptors, ion channels, *etc.*).

Apart from the pharmacological and potential therapeutic relevance of multitarget drugs, the question of their molecular and structural background is of high interest for both the development of more effective drugs deliberately engaging multiple targets and more safe drugs omitting off-target effects. While multitarget binding sites [17,23, 26–28] amongst ABC transporters were suggested before that may apply to other protein families as well, and common structural motifs amongst phylogenetically unrelated proteins were discovered already three decades ago, real structural proof for these hypotheses are lacking. Our study provided a first attempt to combine functional and structural biology through *in vitro* and *in silico* approaches to elucidate important aspects of potential multitarget binding sites [17,23,26–28]. Our blind molecular docking approaches revealed potentially critical amino acids, and particularly phenylalanines and tyrosines (aromatic π-π stacking and hydrophobic interactions) as well as serines and threonines (polar H-bond interactions) are distributed amongst the potential binding pockets of the assessed target proteins. These amino acid patterns resulted in a signature that seems to be complementary to chemical patterns ('superpatterns' [21]) and may found the very basis of structural polypharmacology.

However, it needs to be taken into account that the number of possible interactions between ligands and their targets is limited. From this perspective, interaction patterns between ligands and their targets may resemble even between structurally, functionally, and/or phylogenetically distant protein (super)families. Also, specific interaction patterns determined with the same ligand (*e.g.* compound **57**) may stem from the molecular-structural limitation of the ligand itself that may lead to a limited number of interactions only. However, our results made us confident for four reasons: (i) we identified a relatively high number of interactions for each top ranking docking pose of compound **57** and the respective target; (ii) given that high number of interactions, the number of different interactions was comparably low, focusing certain amino acids only; (iii) the interaction with those amino acids were systematically scattered amongst the biologically assessed target landscape; and (iv) the possibly interacting amino acids occupied mostly similar positions relative to the ligand pose. Nevertheless, more data is warranted, particularly the application of more (indazole-based) privileged ligands with similar bioactivity profiles and the determination of protein structures (*e.g.*, x-ray and cryo-EM) with co-crystallized/co-localized multitarget ligands.

In essence, the present study proved that the targeted development of polypharmacological agents toward a defined set of targets or target combinations indeed leads to output molecules that bear the polypharmacological profiles-of-interest. Particularly undruggable targets (*e.g.*, membrane transporters or others) in mind, polypharmacology provides added value to medicinal chemistry and may provide structurally novel lead molecules for both target identification and validation efforts as well as the drug development pipelines of the future.

4. Materials and methods

4.1. Chemistry

4.1.1. Materials

Chemicals and solvents were obtained from Omkar Traders (Mumbai, India), Sigma-Aldrich (Mumbai, India), and Sisco Research Laboratories (Mumbai, India) and have been used without further

purification. The reactions were performed under inert atmosphere, and reaction progress was followed by thin layer chromatography (TLC) applying aluminum plate coated with silica gel 60 F$_{254}$ (Merck Millipore, Billerica, MA, USA). The mobile phase was a mixture of chloroform (95 %) and methanol (5 %), and the developed TLC plate was inspected under an UV cabinet (Desaga, Biostep, Burkhardtsdorf, Germany) at 254 nm. Column chromatography using silica gel (60–120 μm; Merck, Mumbai, India) and flash chromatography (Combifash RF, Teledyne ISCO, NE, Lincoln, USA) were used for purification purposes applying dichloromethane (98 %) and methanol (2 %) as mobile phase.

The identity of compounds **15–79** was determined by FTIR (Spectrum RXI, PerkinElmer Spectra, Waltham, MA, USA) and/or ^{1}H NMR/^{13}C NMR spectroscopy (Bruker Advance DX 400/126 MHz, Billerica, MA, USA). Chemical shifts (δ) are given in ppm and the multiplicity is provided as singlet (s), doublet (d), doublet of doublets (dd), triplet (t), triplet of doublets (td), pentet (p), and multiplet (m). The molecular mass of compounds has been determined using LC-MS analysis (LCMS-8040, Schimadzu, Kyoto, Japan), and all compounds are >95 % pure by HPLC analysis (Schimadzu, Kyoto, Japan). Melting points were additionally determined using a melting point apparatus (Veego, Mumbai, India). Of note, compounds **23–58** have been synthesized earlier [53].

4.1.2. 1-(1-Oxo-1-(phenylamino)propan-2-yl)-N-phenyl-1H-indazole-3-carboxamide (15)

Beige solid; yield: 65.1 %; melting point: 180 °C-182 °C; ^{1}H NMR (500 MHz, DMSO-d_6): δ (ppm) 10.38 (s, 1H), 10.14 (s, 1H), 8.22 (d, J = 8.1 Hz, 1H), 7.89–7.70 (m, 4H), 7.59–7.52 (m, 2H), 7.39–7.27 (m, 5H), 7.10–7.00 (m, 2H), 5.69 (q, J = 7.0 Hz, 1H), 1.97 (d, J = 7.1 Hz, 3H); MS (ESI+): exact mass calculated for C$_{23}$H$_{20}$N$_4$O$_2$: 384.15, found: 385.25 [M+H]$^+$ and 407.25 [M+Na]$^+$; purity (HPLC): 98.9 %.

4.1.3. 1-(1-Oxo-1-(o-tolylamino)propan-2-yl)-N-phenyl-1H-indazole-3-carboxamide (16)

Yellow solid; yield: 68.1 %; melting point: 187 °C-189 °C; ^{1}H NMR (500 MHz, DMSO-d_6): δ (ppm) 10.13 (s, 1H), 9.66 (s, 1H), 8.23 (d, J = 8.1 Hz, 1H), 7.89–7.74 (m, 3H), 7.49 (t, J = 7.7 Hz, 1H), 7.32 (dt, J = 14.8, 7.5 Hz, 4H), 7.21–7.05 (m, 4H), 5.77 (q, J = 7.0 Hz, 1H), 2.09 (s, 3H), 1.99 (d, J = 7.0 Hz, 3H); MS (ESI+): exact mass calculated for C$_{24}$H$_{22}$N$_4$O$_2$: 398.17, found: 399.30 [M+H]$^+$ and 421.30 [M+Na]$^+$; purity (HPLC): 99.2 %.

4.1.4. 1-(1-Oxo-1-(p-tolylamino)propan-2-yl)-N-phenyl-1H-indazole-3-carboxamide (17)

Brown solid; yield: 70.0 %; melting point: 192 °C-194 °C; ^{1}H NMR (400 MHz, DMSO-d_6): δ (ppm) 10.58 (s, 1H), 10.14 (s, 1H), 8.21 (d, J = 8.1 Hz, 1H), 7.82 (dd, J = 18.9, 8.3 Hz, 3H), 7.52–7.42 (m, 3H), 7.32 (dt, J = 15.2, 7.6 Hz, 3H), 7.07 (d, J = 8.0 Hz, 3H), 5.81–5.70 (m, 1H), 2.20 (s, 3H), 1.96 (d, J = 7.0 Hz, 3H); MS (ESI+): exact mass calculated for C$_{24}$H$_{22}$N$_4$O$_2$: 398.17, found: 399.30 [M+H]$^+$ and 421.30 [M+Na]$^+$; purity (HPLC): 100 %.

4.1.5. 1-(1-((4-methoxyphenyl)amino)-1-oxopropan-2-yl)-N-phenyl-1H-indazole-3-carboxamide (18)

Yellow solid; yield: 67.2 %; melting point: 191 °C-193 °C; ^{1}H NMR (500 MHz, DMSO-d_6): δ (ppm) 10.21 (s, 1H), 10.13 (s, 1H), 8.22 (dt, J = 8.2, 1.1 Hz, 1H), 7.89–7.80 (m, 2H), 7.74 (d, J = 8.6 Hz, 1H), 7.50–7.42 (m, 3H), 7.38–7.28 (m, 3H), 7.13–7.03 (m, 1H), 6.89–6.81 (m, 2H), 5.72–5.62 (m, 1H), 3.67 (s, 3H), 1.96 (d, J = 7.1 Hz, 3H); MS (ESI+): exact mass calculated for C$_{24}$H$_{22}$N$_4$O$_3$: 414.16, found: 415.30 [M+H]$^+$ and 437.30 [M+Na]$^+$; purity (HPLC): 98.5 %.

4.1.6. 1-(1-((4-fluorophenyl)amino)-1-oxopropan-2-yl)-N-phenyl-1H-indazole-3 carboxamide (19)

White powder; yield: 68.2 %; melting point: 183 °C-185 °C; ^{1}H NMR (500 MHz, DMSO-d_6): δ (ppm) 10.39 (s, 1H), 10.13 (s, 1H), 8.30–8.19 (m, 1H), 7.89–7.81 (m, 2H), 7.74 (d, J = 8.5 Hz, 1H), 7.61–7.53 (m, 2H), 7.46 (ddd, J = 8.3, 6.9, 1.2 Hz, 1H), 7.32 (dt, J = 11.6, 7.6 Hz, 3H), 7.10 (dt, J = 13.9, 8.2 Hz, 3H), 5.68 (q, J = 7.0 Hz, 1H), 1.96 (d, J = 7.1 Hz, 3H); ^{13}C NMR (126 MHz, DMSO-d_6): δ 168.42, 160.97, 159.71, 157.79, 141.29, 139.02, 137.67, 135.26, 129.05, 127.35, 124.06, 123.44, 123.33, 122.30, 122.03, 121.97, 120.90, 120.64, 115.91, 115.73, 111.20, 59.01, 17.27; MS (ESI+): exact mass calculated for C$_{23}$H$_{19}$FN$_4$O$_2$: 402.14, found: 403.25 [M+H]$^+$ and 425.25 [M+Na]$^+$; purity (HPLC): 98.8 %.

4.1.7. N-(4-chlorophenyl)-1-(1-oxo-1-(phenylamino)propan-2-yl)-1H-indazole-3-carboxamide (20)

Yellow solid; yield: 69.2 %; melting point: 163 °C-165 °C; ^{1}H NMR (500 MHz, DMSO-d_6): δ (ppm) 10.36 (s, 1H), 10.31 (s, 1H), 8.21 (d, J = 8.1 Hz, 1H), 7.96–7.85 (m, 2H), 7.75 (d, J = 8.5 Hz, 1H), 7.55 (d, J = 7.7 Hz, 2H), 7.51–7.43 (m, 1H), 7.43–7.25 (m, 5H), 7.04 (t, J = 7.3 Hz, 1H), 5.76–5.64 (m, 1H), 1.97 (d, J = 7.0 Hz, 3H); MS (ESI+): exact mass calculated for C$_{23}$H$_{19}$ClN$_4$O$_2$: 418.12, found: 419.25 [M+H]$^+$ and 441.20 [M+Na]$^+$; purity (HPLC): 98.6 %.

4.1.8. N-(4-chlorophenyl)-1-(1-oxo-1-(p-tolylamino)propan-2-yl)-1H-indazole-3-carboxamide (21)

Yellow solid; yield: 66.2 %; melting point: 157 °C-159 °C; ^{1}H NMR (500 MHz, DMSO-d_6): δ (ppm) 10.31 (s, 2H), 8.20 (d, J = 8.1 Hz, 1H), 8.01–7.84 (m, 2H), 7.74 (d, J = 8.5 Hz, 1H), 7.54–7.22 (m, 6H), 7.08 (d, J = 8.1 Hz, 2H), 5.98–5.53 (m, 2H), 2.20 (s, 3H), 1.96 (d, J = 7.0 Hz, 3H); MS (ESI+): exact mass calculated for C$_{24}$H$_{21}$ClN$_4$O$_2$, 432.13, found 433.25 [M+H]$^+$ and 455.25 [M+Na]$^+$; purity (HPLC): 100 %.

4.1.9. N-(4-chlorophenyl)-1-(1-((4-methoxyphenyl)amino)-1-oxopropan-2-yl)-1H-indazole-3-carboxamide (22)

White solid; yield: 68.2 %; melting point: 171 °C-173 °C; ^{1}H NMR (400 MHz, DMSO-d_6): δ (ppm) 10.31 (s, 1H), 10.21 (s, 1H), 8.30–8.12 (m, 2H), 7.96–7.87 (m, 2H), 7.75 (d, J = 8.5 Hz, 1H), 7.52–7.29 (m, 5H), 6.93–6.82 (m, 2H), 5.74–5.62 (m, 1H), 3.67 (s, 3H), 1.95 (d, J = 7.0 Hz, 3H); MS (ESI+): exact mass calculated for C$_{24}$H$_{21}$ClN$_4$O$_2$: 432.13, found: 433.25 [M+H]$^+$ and 455.25 [M+Na]$^+$; purity (HPLC): 100 %.

4.1.10. 1-(2-((2-methoxyphenyl)amino)-2-oxoethyl)-N-phenyl-1H-indazole-3-carboxamide (23)

Brown solid; yield: 83.0 %; melting point: 146 °C-148 °C; IR (neat, cm^{-1}): 3385.43, 3277.00, 1681.86, 1593.36, 1532.70, 1493.14; ^{1}H NMR (500 MHz, DMSO-d_6): δ (ppm) 10.37 (s, 1H), 9.72 (s, 1H), 8.28 (d, J = 8.2 Hz, 1H), 7.93 (dd, J = 20.5, 8.1 Hz, 3H), 7.83 (d, J = 8.6 Hz, 1H), 7.52 (t, J = 7.7 Hz, 1H), 7.36 (t, J = 7.7 Hz, 3H), 7.10 (d, J = 8.5 Hz, 3H), 6.90 (t, J = 7.4 Hz, 1H), 5.64 (s, 2H), 3.88 (s, 3H); MS (ESI+): exact mass calculated for C$_{23}$H$_{20}$N$_4$O$_3$: 400.15, found: 401.30 [M+H]$^+$ and 423.30 [M+Na]$^+$, purity (HPLC): 98.2 %.

4.1.11. 1-(2-((3-methoxyphenyl)amino)-2-oxoethyl)-N-phenyl-1H-indazole-3-carboxamide (24)

Brown solid; yield: 83.0 %; melting point: 157 °C-159 °C; IR (neat, cm^{-1}): 3255.82, 3074.48, 1650.92, 1539.67, 1244.67, 1151.85, 756.73; ^{1}H NMR (500 MHz, DMSO-d_6): δ (ppm) 10.52 (s, 1H), 10.33 (d, J = 1.9 Hz, 1H), 8.28 (d, J = 8.2 Hz, 1H), 7.90 (d, J = 8.0 Hz, 2H), 7.82 (d, J = 8.9 Hz, 1H), 7.53 (dd, J = 8.6, 6.5 Hz, 1H), 7.40–7.29 (m, 4H), 7.25 (td, J = 8.2, 1.9 Hz, 1H), 7.16–7.07 (m, 2H), 6.68 (dd, J = 8.2, 2.4 Hz, 1H), 5.53 (s, 2H), 3.72 (s, 3H); MS (ESI+): exact mass calculated for C$_{23}$H$_{20}$N$_4$O$_3$: 400.15, found: 401.30 [M+H]$^+$ and 423.30 [M+Na]$^+$; purity (HPLC); 100 %.

4.1.12. 1-(2-((2-chorophenyl)amino)-2-oxoethyl)-N-phenyl-1H-indazole-3-carboxamide (25)

White solid; yield: 82.1 %; melting point: 176 °C-178 °C; IR (neat, cm^{-1}): 3260.16, 1671.92, 1596.07, 1533.59, 1495.72, 1478.02, 1443.23; ^{1}H NMR (500 MHz, DMSO-d_6): δ (ppm) 10.36 (s, 1H), 10.08 (s,

1H), 8.27 (d, *J* = 8.1 Hz, 1H), 7.91 (d, *J* = 8.0 Hz, 2H), 7.83 (d, *J* = 8.5 Hz, 1H), 7.78 (dd, *J* = 8.2, 1.6 Hz, 1H), 7.58–7.49 (m, 2H), 7.40–7.29 (m, 4H), 7.20 (td, *J* = 7.8, 1.6 Hz, 1H), 7.11 (t, *J* = 7.4 Hz, 1H), 5.62 (s, 2H); MS (ESI+): exact mass calculated for $C_{22}H_{17}ClN_4O_2$: 404.10, found: 405.25 [M+H]$^+$ and 427.25 [M+Na]$^+$; purity (HPLC): 100 %.

4.1.13. 1-(2-((4-chlorophenyl)amino)-2-oxoethyl)-N-phenyl-1H-indazole-3-carboxamide (26)

White solid; yield: 81.0 %; melting point: 179 °C-181 °C; IR (neat, cm^{-1}): 3309.29, 1668.06, 1534.28, 1491.74, 1247.37, 754.64; ^{1}H NMR (500 MHz, DMSO-d_6): δ (ppm) 10.66 (s, 1H), 10.35 (s, 1H), 8.28 (d, *J* = 8.2 Hz, 1H), 7.91 (d, *J* = 8.0 Hz, 2H), 7.82 (d, *J* = 8.5 Hz, 1H), 7.65 (d, *J* = 8.5 Hz, 2H), 7.52 (t, *J* = 7.7 Hz, 1H), 7.43–7.32 (m, 4H), 7.31 (s, 1H), 7.11 (t, *J* = 7.4 Hz, 1H), 5.54 (s, 1H); MS (ESI+): exact mass calculated for $C_{22}H_{17}ClN_4O_2$: 404.10, found: 405.25 [M+H]$^+$ and 427.25 [M+Na]$^+$; purity (HPLC); 100 %.

4.1.14. 1-(2-((2,5-dichlorophenyl)amino)-2-oxoethyl)-N-phenyl-1H-indazole-3-carboxamide (27)

White solid; yield: 81.0 %; melting point 155 °C-157 °C; IR (neat, cm^{-1}): 3400.21, 3323.49, 1687.80, 1588.75, 1533.00, 1444.70; ^{1}H NMR (500 MHz, DMSO-d_6) δ (ppm) 10.35 (s, 1H), 10.20 (s, 1H), 8.28 (d, *J* = 8.2 Hz, 1H), 7.97–7.88 (m, 3H), 7.84 (d, *J* = 8.5 Hz, 1H), 7.59 (d, *J* = 8.7 Hz, 1H), 7.57–7.50 (m, 1H), 7.36 (t, *J* = 7.9 Hz, 3H), 7.29 (dd, *J* = 8.6, 2.6 Hz, 1H), 7.11 (t, *J* = 7.3 Hz, 1H), 5.67 (s, 2H); MS (ESI+): exact mass calculated for $C_{22}H_{16}Cl_2N_4O_2$ 438.06, found 439.25 [M+H]$^+$ and 461.20 [M+Na]$^+$; purity (purity); 100 %.

4.1.15. 1-(2-((2,6-dichlorophenyl)amino)-2-oxoethyl)-N-phenyl-1H-indazole-3-carboxamide (28)

Brown solid; yield: 81.0 %; melting point: 169 °C-171 °C; IR (neat, cm^{-1}): 3256.50, 1686.16, 1665.32, 1598.61,1537.60; ^{1}H NMR (500 MHz, DMSO-d_6): δ (ppm) 10.39 (s, 1H), 10.35 (s, 1H), 8.27 (d, *J* = 8.2 Hz, 1H), 7.90 (d, *J* = 8.0 Hz, 2H), 7.73 (d, *J* = 8.5 Hz, 1H), 7.55 (dd, *J* = 14.6, 7.8 Hz, 3H), 7.41–7.33 (m, 4H), 7.12 (t, *J* = 7.3 Hz, 1H), 5.58 (s, 2H); MS (ESI+): exact mass calculated for $C_{22}H_{16}Cl_2N_4O_2$: 438.06, found: 439.25 [M+H]$^+$ and 461.20 [M+Na]$^+$; purity (HPLC); 100 %.

4.1.16. 1-(2-((3,5-dichlorophenyl)amino)-2-oxoethyl)-N-phenyl-1H-indazole-3-carboxamide (29)

White solid; yield: 81.0 %; melting point: 161 °C-163 °C; IR (neat, cm^{-1}): 3381.79, 3251.51, 1671.81, 1586.02, 1531.65, 1495.70, 1441.72; ^{1}H NMR (500 MHz, DMSO-d_6): δ (ppm) 10.87 (s, 1H), 10.32 (s, 1H), 8.28 (dd, *J* = 8.2, 2.6 Hz, 1H), 7.90 (dd, *J* = 8.4, 2.5 Hz, 2H), 7.82 (dd, *J* = 8.5, 2.3 Hz, 1H), 7.67 (d, *J* = 2.4 Hz, 2H), 7.53 (t, *J* = 7.8 Hz, 1H), 7.40–7.31 (m, 4H), 7.11 (t, *J* = 7.4 Hz, 1H), 5.55 (s, 2H); MS (ESI+): exact mass calculated for $C_{22}H_{16}Cl_2N_4O_2$: 438.06, found: 439.25 [M+H]$^+$ and 461.20 [M+Na]$^+$; purity (HPLC): 100 %.

4.1.17. 1-(2-((4-bromophenyl) amino)-2-oxoethyl)-N-phenyl-1H-indazole-3-carboxamide (30)

White solid; yield: 83.0 %. melting point: 167 °C-159 °C; IR (neat, cm^{-1}): 3306.44, 1668.60, 1531.98, 1302.99, 1247.11, 754.46; ^{1}H NMR (500 MHz, DMSO-d_6): δ (ppm) 10.68 (s, 1H), 10.33 (s, 1H), 8.28 (d, *J* = 8.2 Hz, 1H), 7.90 (d, *J* = 8.0 Hz, 2H), 7.82 (d, *J* = 8.5 Hz, 1H), 7.59 (d, *J* = 8.6 Hz, 2H), 7.53 (d, *J* = 8.2 Hz, 3H), 7.36 (t, *J* = 7.7 Hz, 3H), 7.11 (t, *J* = 7.4 Hz, 1H), 5.54 (s, 2H); MS (ESI+): exact mass calculated for $C_{22}H_{17}BrN_4O_2$: 448.05, found: 451.20 [M+2H]$^+$ and 473.20 [M+2H + Na]$^+$, purity (HPLC): 100 %.

4.1.18. N-(3-methoxyphenyl)-1-(2-((2-methoxyphenyl)amino)-2-oxoethyl)-1H-indazole-3-carboxamide (31)

White solid; yield: 83.8 %; melting point: 151 °C-153 °C; IR (neat, cm^{-1}): 3389.65, 3306.38, 1688.29, 1667.88, 1594.12, 1537.91, 1462.75; ^{1}H NMR (500 MHz, DMSO-d_6): δ (ppm) 10.32 (s, 1H), 9.71 (s, 1H), 8.27 (d, *J* = 8.1 Hz, 1H), 7.95 (d, *J* = 8.0 Hz, 1H), 7.83 (d, *J* = 8.5

Hz, 1H), 7.61 (d, *J* = 2.6 Hz, 1H), 7.52 (t, *J* = 7.6 Hz, 2H), 7.35 (t, *J* = 7.5 Hz, 1H), 7.25 (t, *J* = 8.1 Hz, 1H), 7.09 (q, *J* = 5.9, 5.1 Hz, 2H), 6.94–6.86 (m, 1H), 6.69 (dd, *J* = 8.3, 2.4 Hz, 1H), 5.63 (s, 2H), 3.88 (s, 3H), 3.77 (s, 3H); ^{13}C NMR (126 MHz, DMSO-d_6): δ 165.79, 160.92, 159.84, 149.81, 142.44, 140.40, 138.23, 129.77, 127.42, 127.13, 125.14, 123.20, 122.92, 122.14, 121.92, 120.75, 112.95, 111.67, 111.38, 109.50, 106.43, 56.15, 55.44; MS (ESI+): exact mass calculated for $C_{24}H_{22}N_4O_4$: 430.35, found: 431.35 [M+H]$^+$ and 453.45 [M+Na]$^+$; purity (HPLC): 100.%.

4.1.19. N-(3-methoxyphenyl)-1-(2-((3-methoxyphenyl)amino)-2-oxoethyl)-1H-indazole-3-carboxamide (32)

White solid; yield: 80.7 %; melting point: 145 °C-147 °C; IR (neat, cm^{-1}): 3383.59, 3289.49, 1667.33, 1593.31, 1532.75, 1478.21, 1454.22, 1433.21; ^{1}H NMR (500 MHz, DMSO-d_6): δ (ppm) 10.53 (s, 1H), 10.29 (s, 1H), 8.28 (d, *J* = 8.2 Hz, 1H), 7.82 (d, *J* = 8.5 Hz, 1H), 7.60 (t, *J* = 2.3 Hz, 1H), 7.53 (dd, *J* = 8.4, 6.6 Hz, 2H), 7.40–7.21 (m, 4H), 7.16–7.10 (m, 1H), 6.68 (ddd, *J* = 8.0, 5.0, 2.6 Hz, 2H), 5.52 (s, 2H), 3.77 (s, 3H), 3.72 (s, 3H); ^{13}C NMR (126 MHz, DMSO-d_6): δ 165.63, 160.90, 160.01, 159.84, 142.54, 140.38, 140.17, 138.24, 130.19, 129.77, 127.43, 123.18, 122.88, 122.13, 112.92, 111.77, 111.36, 109.63, 109.51, 106.40, 105.27, 55.44, 55.40; MS (ESI+): exact mass calculated for $C_{24}H_{22}N_4O_4$: 430.16, found: 431.35 [M+H]$^+$ and 453.45 [M+Na]$^+$; purity (HPLC): 100 %.

4.1.20. 1-(2-((2-chlorophenyl)amino)-2-oxoethyl)-N-(3-methoxyphenyl)-1H-indazole-3-carboxamide (33)

White solid; yield: 86.1 %; melting point: 175 °C-177 °C; IR (neat, cm^{-1}): 3402.05, 3252.66, 1673.96, 1610.01, 1593.98, 1539.36, 1494.38; ^{1}H NMR (500 MHz, DMSO-d_6): δ (ppm) 10.34 (d, *J* = 8.9 Hz, 1H), 10.08 (s, 1H), 8.29 (t, *J* = 8.6 Hz, 1H), 7.84 (q, *J* = 7.8, 6.4 Hz, 1H), 7.79 (d, *J* = 8.2 Hz, 1H), 7.62 (d, *J* = 8.7 Hz, 1H), 7.54 (q, *J* = 8.5, 7.8 Hz, 3H), 7.42–7.31 (m, 2H), 7.25 (dq, *J* = 22.0, 8.7, 7.9 Hz, 2H), 6.70 (d, *J* = 8.0 Hz, 1H), 5.65 (d, *J* = 8.9 Hz, 2H), 3.79 (d, *J* = 9.1 Hz, 3H); MS (ESI+): exact mass calculated for $C_{23}H_{19}ClN_4O_3$: 434.11, found: 435.30 [M+H]$^+$ and 457.35 [M+Na]$^+$; purity (HPLC): 98.7 %

4.1.21. 1-(2-((4-chlorophenyl)amino)-2-oxoethyl)-N-(3-methoxyphenyl)-1H-indazole-3-carboxamide (34)

White solid; yield: 81.4 %; melting point: 161 °C-163 °C; IR (neat, cm^{-1}): 3314.75, 1675.75, 1607.69, 1537.66, 1491.82, 1302.54, 1165.15, 753.43; ^{1}H NMR (500 MHz, DMSO-d_6): δ (ppm) 10.67 (d, *J* = 5.0 Hz, 1H), 10.29 (d, *J* = 5.1 Hz, 1H), 8.29 (d, *J* = 7.7 Hz, 1H), 7.83 (d, *J* = 8.1 Hz, 1H), 7.67–7.58 (m, 3H), 7.53 (d, *J* = 7.3 Hz, 2H), 7.44–7.32 (m, 3H), 7.30–7.21 (m, 1H), 6.69 (dt, *J* = 6.2, 3.1 Hz, 1H), 5.54 (s, 2H), 3.77 (s, 3H); MS (ESI+): exact mass calculated for $C_{23}H_{19}ClN_4O_2$: 434.11, found: 435.35 [M+H]$^+$ and 457.40 [M+Na]$^+$; purity (HPLC): 100 %.

4.1.22. 1-(2-((2,5-dichlorophenyl)amino)-2-oxoethyl)-N-(3-methoxyphenyl)-1H-indazole-3-carboxamide (35)

White solid; yield: 85.4 %; melting point: 177 °C-179 °C; IR (neat, cm^{-1}): 3280.87, 1676.71, 1584.01, 1531.81, 1493.68, 1463.50, 1404.63; ^{1}H NMR (500 MHz, DMSO-d_6): δ (ppm) 10.31 (d, *J* = 5.5 Hz, 1H), 10.24 (s, 1H), 8.28 (d, *J* = 7.7 Hz, 1H), 8.03–7.92 (m, 1H), 7.93–7.80 (m, 1H), 7.64–7.55 (m, 2H), 7.53 (q, *J* = 7.0, 6.0 Hz, 2H), 7.36 (q, *J* = 7.0, 6.6 Hz, 1H), 7.27 (ddt, *J* = 14.5, 8.4, 4.4 Hz, 2H), 6.70 (dt, *J* = 6.5, 3.2 Hz, 1H), 5.66 (s, 2H), 3.78 (d, *J* = 5.6 Hz, 3H); MS (ESI+): exact mass calculated for $C_{22}H_{16}Cl_2N_4O_2$: 468.07, found: 469.25 [M+H]$^+$ and 491.35 [M+Na]$^+$; purity (HPLC): 97.4 %.

4.1.23. 1-(2-((2,6-dichlorophenyl)amino)-2-oxoethyl)-N-(3-methoxyphenyl)-1H-indazole-3-carboxamide (36)

White solid; yield: 85.4 %; melting point: 167 °C-169 °C; IR (neat, cm^{-1}): 3391.91, 3213.49, 1682.49, 1607.81, 153781, 1492.43. ^{1}H NMR (500 MHz, DMSO-d_6): δ (ppm) 10.42 (s, 1H), 10.31 (s, 1H), 8.27 (d, *J* =

8.1 Hz, 1H), 7.73 (d, *J* = 8.5 Hz, 1H), 7.61 (t, *J* = 2.2 Hz, 1H), 7.59–7.49 (m, 4H), 7.36 (t, *J* = 7.8 Hz, 2H), 7.27 (t, *J* = 8.1 Hz, 1H), 6.70 (dd, *J* = 8.2, 2.4 Hz, 1H), 5.57 (s, 2H), 3.78 (s, 3H); MS (ESI+): exact mass calculated for C$_{23}$H$_{18}$Cl$_2$N$_4$O$_3$: 468.07, found: 469.25 [M+H]$^+$ and 491.30 [M+Na]$^+$; purity (HPLC): 100 %.

4.1.24. 1-(2-((4-bromophenyl)amino)-2-oxoethyl)-N-(3-methoxyphenyl)-1H-indazole-3-carboxamide (37)

White solid; yield: 80.1 %; melting point: 155 °C-157 °C; IR (neat, cm^{-1}): 3314.08, 1676.68, 1534.15, 1488.50, 1303.08, 753.47; ^{1}H NMR (500 MHz, DMSO-*d$_6$*): δ (ppm) 10.66 (s, 1H), 10.29 (s, 1H), 8.30–8.24 (m, 1H), 7.82 (d, *J* = 8.5 Hz, 1H), 7.62–7.45 (m, 8H), 7.42–7.32 (m, 1H), 7.25 (t, *J* = 8.1 Hz, 1H), 6.69 (dd, *J* = 8.2, 2.5 Hz, 1H), 5.53 (s, 2H), 3.77 (d, *J* = 1.1 Hz, 3H); MS (ESI+): exact mass calculated for C$_{23}$H$_{19}$BrN$_4$O$_3$: 478.06, found: 481.50 [M+2H]$^+$ and 503.30 [M+2H + Na]$^+$; purity (HPLC): 99.9 %.

4.1.25. N-(4-methoxyphenyl)-1-(2-((4-methoxyphenyl)amino)-2-oxoethyl)-1H-indazole-3-carboxamide (38)

White solid; yield: 80.7 %; melting point: 171 °C-173 °C; IR (neat, cm^{-1}): 3298.31, 1667.94, 1650.90, 1515.00, 1493.35; ^{1}H NMR (500 MHz, DMSO-*d$_6$*): δ (ppm) 10.38 (s, 1H), 10.23 (s, 1H), 8.27 (d, *J* = 8.1 Hz, 1H), 7.80 (d, *J* = 8.5 Hz, 3H), 7.51 (t, *J* = 9.0 Hz, 3H), 7.34 (t, *J* = 7.5 Hz, 1H), 6.92 (t, *J* = 8.9 Hz, 4H), 5.48 (s, 2H), 3.74 (d, *J* = 15.0 Hz, 6H); MS (ESI+): exact mass calculated for C$_{22}$H$_{16}$Cl$_2$N$_4$O$_2$: 430.16, found: 431.30 [M+H]$^+$ and 453.30 [M+Na]$^+$; purity (HPLC): 100 %.

4.1.26. 1-(2-((4-chlorophenyl)amino)-2-oxoethyl)-N-(4-methoxyphenyl)-1H-indazole-3-carboxamide (39)

White solid; yield: 83.0 %; melting point: 176 °C-178 °C; IR (neat, cm^{-1}): 3310.92, 3270.29, 1670.23, 1651.79, 1514.84, 1492.11; ^{1}H NMR (500 MHz, DMSO-*d$_6$*): δ (ppm) 10.67 (s, 1H), 10.22 (s, 1H), 8.27 (d, *J* = 8.1 Hz, 1H), 7.80 (dd, *J* = 8.8, 4.5 Hz, 3H), 7.64 (d, *J* = 8.5 Hz, 2H), 7.55–7.48 (m, 1H), 7.40 (d, *J* = 8.6 Hz, 2H), 7.34 (t, *J* = 7.5 Hz, 1H), 6.96–6.89 (m, 2H), 5.52 (s, 2H), 3.76 (s, 3H); MS (ESI+): exact mass calculated for C$_{23}$H$_{19}$ClN$_4$O$_3$: 434.11, found: 435.25 [M+H]$^+$ and 457.20 [M+Na]$^+$; purity (HPLC): 99.1 %.

4.1.27. 1-(2-((4-bromophenyl)amino)-2-oxoethyl)-N-(4-methoxyphenyl)-1H-indazole-3-carboxamide (40)

Yellow solid; yield: 80.9 %; melting point: 148 °C-150 °C; IR (neat, cm^{-1}): 3401.94, 3262.51, 1666.43, 1526.11, 1510.77, 1489.66; ^{1}H NMR (500 MHz, DMSO-*d$_6$*): δ (ppm) 10.66 (s, 1H), 10.22 (s, 1H), 8.27 (d, *J* = 8.1 Hz, 1H), 7.80 (dd, *J* = 8.7, 4.8 Hz, 3H), 7.58 (d, *J* = 8.6 Hz, 2H), 7.56–7.48 (m, 3H), 7.34 (t, *J* = 7.5 Hz, 1H), 6.97–6.89 (m, 2H), 5.52 (s, 2H), 3.76 (s, 3H); MS (ESI+): exact mass calculated for C$_{23}$H$_{19}$BrN$_4$O$_3$: 478.06, found: 481.20 [M+2H]$^+$ and 503.20 [M+2H + Na]$^+$; purity (HPLC); 99.0 %.

4.1.28. N-(3,4-difluorophenyl)-1-(2-((4-methoxyphenyl)amino)-2-oxoethyl)-1H-indazole-3-carboxamide (41)

White solid; yield: 85.8 %; melting point: 147 °C-150 °C; IR (neat, cm^{-1}): 3271.52, 2915.54, 1665.32, 1536.32, 1511.80, 1174.67, 745.77; ^{1}H NMR (500 MHz, DMSO-*d$_6$*): δ (ppm) 10.66 (s, 1H), 10.47 (s, 1H), 8.27 (d, *J* = 8.1 Hz, 1H), 8.07 (ddd, *J* = 13.4, 7.6, 2.6 Hz, 1H), 7.83 (d, *J* = 8.5 Hz, 1H), 7.74 (d, *J* = 9.0 Hz, 1H), 7.52 (d, *J* = 8.2 Hz, 3H), 7.43 (q, *J* = 9.6 Hz, 1H), 7.36 (t, *J* = 7.5 Hz, 1H), 6.91 (d, *J* = 8.6 Hz, 2H), 5.51 (s, 2H), 3.73 (s, 3H); MS (ESI+): exact mass calculated for C$_{23}$H$_{18}$ F$_2$N$_4$O$_2$: 436.13, found: 437.30 [M+H]$^+$ and 459.40 [M+Na]$^+$; purity (HPLC): 97.5 %.

4.1.29. 1-(2-((4-chlorophenyl)amino)-2-oxoethyl)-N-(3,4-difluorophenyl)-1H-indazole-3-carboxamide (42)

White solid; yield 85.8 %; melting point: 169 °C-171 °C; IR (neat, cm^{-1}): 3388.57, 3252.4, 1683.60, 1537.58, 1176.03, 747.84; ^{1}H NMR (500 MHz, DMSO-*d$_6$*): δ (ppm) 10.68 (s, 1H), 10.65 (s, 1H), 8.27 (d, *J* =

8.2 Hz, 1H), 8.13 (s, 1H), 8.07 (ddd, *J* = 13.8, 7.8, 2.9 Hz, 1H), 7.83 (d, *J* = 8.6 Hz, 1H), 7.74 (d, *J* = 9.1 Hz, 1H), 7.64 (d, *J* = 8.5 Hz, 2H), 7.53 (t, *J* = 7.8 Hz, 1H), 7.40 (ddd, *J* = 20.0, 14.5, 8.9 Hz, 4H), 5.55 (s, 2H); MS (ESI+): exact mass calculated for C$_{22}$H$_{15}$ ClF$_2$N$_4$O$_2$: 440.08, found: 441.30 [M+H]$^+$ and 463.35 [M+Na]$^+$; purity (HPLC): 100 %.

4.1.30. 1-(2-((4-bromophenyl)amino)-2-oxoethyl)-N-(3,4-difluorophenyl)-1H-indazole-3-carboxamide (43)

White solid; yield: 83.8 %; melting point: 153 °C-155 °C; IR (neat, cm^{-1}): 3388.04, 3250.65, 1683.89, 1537.58, 1176.01, 746.36; ^{1}H NMR (500 MHz, DMSO-*d$_6$*): δ (ppm) 10.66 (d, *J* = 16.4 Hz, 2H), 8.27 (d, *J* = 8.1 Hz, 1H), 8.06 (ddd, *J* = 13.4, 7.5, 2.6 Hz, 1H), 7.83 (d, *J* = 8.5 Hz, 1H), 7.77–7.71 (m, 1H), 7.61–7.49 (m, 5H), 7.43 (q, *J* = 9.6 Hz, 1H), 7.37 (t, *J* = 7.5 Hz, 1H), 5.54 (s, 2H); MS (ESI+): exact mass calculated for C$_{22}$H$_{15}$ BrF$_2$N$_4$O$_2$: 484.03, found: 487.15 [M+2H]$^+$ and 509.20 [M+2H + Na]$^+$; purity (HPLC): 100 %.

4.1.31. N-(4-chlorophenyl)-1-(2-((4-methoxyphenyl)amino)-2-oxoethyl)-1H-indazole-3-carboxamide (44)

Brown solid; yield: 84.15 %; melting point: 150 °C-152 °C; IR (neat, cm−1): 3263.47, 1666.17, 1529.16, 1492.16, 1241.85; ^{1}H NMR (500 MHz, DMSO-*d$_6$*): δ (ppm) 10.53 (s, 1H), 10.38 (s, 1H), 8.27 (d, *J* = 8.2 Hz, 1H), 7.96 (d, *J* = 8.4 Hz, 2H), 7.82 (d, *J* = 8.5 Hz, 1H), 7.52 (d, *J* = 8.3 Hz, 3H), 7.41 (d, *J* = 8.6 Hz, 2H), 7.36 (t, *J* = 7.5 Hz, 1H), 6.91 (d, *J* = 8.7 Hz, 2H), 5.50 (s, 2H), 3.73 (s, 3H); MS (ESI+): exact mass calculated for C$_{23}$H$_{19}$ClN$_4$O$_3$: 434.11, found: 435.35 [M+H]$^+$ and 457.40 [M+Na]$^+$; purity (HPLC): 100 %.

4.1.32. N-(4-chlorophenyl)-1-(2-((4-chlorophenyl)amino)-2-oxoethyl)-1H-indazole-3-carboxamide (45)

White solid; yield: 80.1 %; melting point: 170 °C-172 °C; IR (neat, cm^{-1}): 3386.47, 3288.53, 1666.29, 1527.53, 1247.41, 749.93; ^{1}H NMR (500 MHz, DMSO-*d$_6$*): δ (ppm) 10.67 (s, 1H), 10.53 (s, 1H), 8.27 (d, *J* = 8.2 Hz, 1H), 7.95 (d, *J* = 8.4 Hz, 2H), 7.82 (d, *J* = 8.6 Hz, 1H), 7.63 (d, *J* = 8.4 Hz, 2H), 7.53 (t, *J* = 7.7 Hz, 1H), 7.44–7.34 (m, 5H), 5.54 (s, 2H); MS (ESI+): exact mass calculated for C$_{22}$H$_{16}$Cl$_2$N$_4$O$_2$: 438.07, found: 439.30 [M+H]$^+$ and 461.35 [M+Na]$^+$; purity (HPLC): 98.7 %.

4.1.33. N-(2-bromophenyl)-1-(2-((4-chlorophenyl)amino)-2-oxoethyl)-1H-indazole-3-carboxamide (46)

White solid; yield: 84.1 %; melting point: 145 °C-147 °C; IR (neat, cm^{-1}): 3307.18, 1670.65, 1527.72, 1491.17, 1294.10, 742.35; ^{1}H NMR (500 MHz, DMSO-*d$_6$*): δ (ppm) 10.69 (s, 1H), 9.75 (s, 1H), 8.26 (d, *J* = 8.1 Hz, 1H), 8.14 (d, *J* = 8.0 Hz, 1H), 7.84 (d, *J* = 8.5 Hz, 1H), 7.73 (d, *J* = 8.0 Hz, 1H), 7.64 (d, *J* = 8.5 Hz, 2H), 7.55 (t, *J* = 7.7 Hz, 1H), 7.46 (t, *J* = 7.7 Hz, 1H), 7.40 (dd, *J* = 8.0, 5.4 Hz, 3H), 7.21–7.13 (m, 1H), 5.54 (s, 2H); MS (ESI+): exact mass calculated for C$_{22}$H$_{16}$BrClN$_4$O$_2$: 482.01, found: 485.15 [M+2H]$^+$ and 507.17 [M+2H + Na]$^+$; purity (HPLC): 100 %.

4.1.34. N-(4-bromophenyl)-1-(2-((2-methoxyphenyl)amino)-2-oxoethyl)-1H-indazole-3-carboxamide (47)

White solid; yield: 85.8 %; melting point: 173 °C-175 °C; IR (neat, cm^{-1}): 3305.34, 2935.06, 1672.36, 1590.43, 1531.91, 1494.81. 1462.00; ^{1}H NMR (500 MHz, DMSO-*d$_6$*): δ (ppm) 10.56 (s, 1H), 9.72 (s, 1H), 8.27 (d, *J* = 8.2 Hz, 1H), 7.97–7.87 (m, 3H), 7.83 (d, *J* = 8.6 Hz, 1H), 7.57–7.49 (m, 3H), 7.36 (t, *J* = 7.5 Hz, 1H), 7.09 (q, *J* = 5.8, 5.2 Hz, 2H), 6.90 (ddd, *J* = 8.6, 6.3, 2.7 Hz, 1H), 5.64 (s, 2H), 3.89 (s, 3H); MS (ESI+): exact mass calculated for C$_{23}$H$_{19}$BrN$_4$O$_3$: 478.06, found: 481.20 [M+2H]$^+$ and 503.30 [M+2H + Na]$^+$; purity (HPLC): 100 %.

4.1.35. N-(4-bromophenyl)-1-(2-((3-methoxyphenyl)amino)-2-oxoethyl)-1H-indazole-3-carboxamide (48)

Brown solid; yield: 85.8 %; melting point: 159 °C-161 °C; IR (neat, cm^{-1}): 3263.47, 1666.17, 1529.16, 1492.16, 1241.85; ^{1}H NMR (500 MHz, DMSO-*d$_6$*): δ (ppm) 10.53 (s, 1H), 10.52 (s, 1H), 8.46 (s, 1H), 8.27

(d, *J* = 8.1 Hz, 1H), 7.93–7.87 (m, 2H), 7.82 (d, *J* = 8.5 Hz, 1H), 7.53 (t, *J* = 8.3 Hz, 3H), 7.40–7.29 (m, 3H), 7.25 (t, *J* = 8.2 Hz, 1H), 7.12 (dd, *J* = 8.0, 1.9 Hz, 1H), 6.68 (dd, *J* = 8.3, 2.5 Hz, 1H), 5.53 (s, 2H), 3.72 (s, 3H); MS (ESI+): exact mass calculated for C$_{23}$H$_{19}$BrN$_4$O$_3$ 478.06, found: 481.20 [M+2H]$^+$ and 503.30 [M+2H + Na]$^+$; purity (HPLC): 100 %.

4.1.36. N-(4-bromophenyl)-1-(2-((4-methoxyphenyl)amino)-2-oxoethyl)-1H-indazole-3-carboxamide (49)

White solid; yield: 85.75 %; melting point: 171 °C-173 °C; IR (neat, cm^{-1}): 3386.47, 3288.53, 1666.29, 1527.53, 1247.41, 749.93; ^{1}H NMR (500 MHz, DMSO-*d$_6$*): δ (ppm) 10.53 (s, 1H), 10.38 (s, 1H), 8.27 (d, *J* = 8.1 Hz, 1H), 7.93–7.88 (m, 2H), 7.82 (d, *J* = 8.4 Hz, 1H), 7.53 (t, *J* = 9.2 Hz, 5H), 7.36 (t, *J* = 7.5 Hz, 1H), 6.91 (d, *J* = 8.6 Hz, 2H), 5.50 (s, 2H), 3.73 (s, 3H); MS (ESI+): exact mass calculated for C$_{23}$H$_{19}$BrN$_4$O$_3$: 478.06, found 481.20 [M+2H]$^+$ and 503.25 [M+2H + Na]$^+$; purity (HPLC): 97.9 %.

4.1.37. N-(4-bromophenyl)-1-(2-((2-chlorophenyl)amino)-2-oxoethyl)-1H-indazole-3-carboxamide (50)

White solid; yield: 81.69 %: melting point: 169 °C-171 °C; IR (neat, cm^{-1}): 3389.51, 3290.82, 1671.40, 1664.71, 1590.31, 1526.33, 1494.31 1475.66, 1445.53; ^{1}H NMR (500 MHz, DMSO-*d$_6$*): δ (ppm) 10.57 (d, *J* = 12.0 Hz, 1H), 10.06 (s, 1H), 8.27 (d, *J* = 8.9 Hz, 1H), 7.91 (d, *J* = 8.7 Hz, 2H), 7.87–7.81 (m, 1H), 7.78 (d, *J* = 8.3 Hz, 1H), 7.59–7.49 (m, 4H), 7.35 (dt, *J* = 14.4, 7.4 Hz, 2H), 7.23 (s, 1H), 5.65 (s, 2H); MS (ESI+): exact mass calculated for C$_{22}$H$_{16}$BrClN$_4$O$_2$: 482.01, found: 485.15 [M+2H]$^+$ and 507.25 [M+2H + Na]$^+$; purity (HPLC): 98.7 %.

4.1.38. N-(4-bromophenyl)-1-(2-((4-chlorophenyl)amino)-2-oxoethyl)-1H-indazole-3-carboxamide (51)

White solid; yield: 80.2 %; melting point: 162 °C-164 °C; IR (neat, cm^{-1}): 3400.00, 3262.00, 1665.74, 1523.07, 1492.50 1402.15, 747.83; ^{1}H NMR (500 MHz, DMSO-*d$_6$*) δ (ppm) 10.67 (s, 1H), 10.52 (s, 1H), 8.27 (d, *J* = 8.2 Hz, 1H), 7.90 (d, *J* = 8.7 Hz, 2H), 7.82 (d, *J* = 8.5 Hz, 1H), 7.64 (d, *J* = 8.4 Hz, 4H), 7.54 (d, *J* = 8.9 Hz, 3H), 7.40 (d, *J* = 8.4 Hz, 2H), 5.54 (s, 2H); MS (ESI+): exact mass calculated for C$_{22}$H$_{16}$BrClN$_4$O$_2$: 482.01, found: 485.15 [M+2H]+and 507.25 [M+2H + Na]$^+$; purity (HPLC): 99.3 %.

4.1.39. 1-(2-((4-chlorophenyl) amino-2-oxoethyl)-N-(pyridin-2-yl)-1H-indazole-3-carboxamide (52)

White solid; yield: 84.0 %; melting point: 162 °C-164 °C; IR (neat, cm^{-1}): 3262.20, 3057.44, 1672.60, 1526.18, 1434.98, 1300.94, 827.68; ^{1}H NMR (500 MHz, DMSO-*d$_6$*) δ (ppm) 10.73 (s, 1H), 9.72 (s, 1H), 8.38 (d, *J* = 4.8 Hz, 1H), 8.27 (d, *J* = 8.3 Hz, 2H), 7.94–7.82 (m, 2H), 7.64 (d, *J* = 8.6 Hz, 2H), 7.55 (t, *J* = 7.7 Hz, 1H), 7.40 (dd, *J* = 8.1, 5.4 Hz, 3H), 7.19 (dd, *J* = 7.3, 4.9 Hz, 1H), 5.55 (s, 2H); MS (ESI+): exact mass calculated for C$_{21}$H$_{16}$ClN$_5$O$_2$: 405.10, found: 406.30 [M+H]$^+$ and 428.25 [M+Na]$^+$; purity (HPLC): 98.0 %.

4.1.40. 1-(2-((2,5-dichlorophenyl)amino)-2-oxoethyl)-N-(pyridin-2-yl)-1H-indazole-3-carboxamide (53)

White solid; yield: 81.2 %; melting point: 147 °C-149 °C; IR (neat, cm^{-1}): 3384.7, 3274.87, 1685.22, 1589.93, 1532.93, 1436.1; ^{1}H NMR (500 MHz, DMSO-*d$_6$*): δ (ppm) 10.22 (s, 1H), 9.74 (s, 1H), 8.39 (d, *J* = 4.7 Hz, 1H), 8.27 (dd, *J* = 8.3, 3.3 Hz, 2H), 7.96–7.83 (m, 3H), 7.61–7.53 (m, 2H), 7.40 (t, *J* = 7.6 Hz, 1H), 7.29 (dt, *J* = 8.7, 1.9 Hz, 1H), 7.20 (dd, *J* = 7.2, 5.0 Hz, 1H), 5.67 (s, 2H); ^{13}C NMR (126 MHz, DMSO-*d$_6$*): δ 166.46, 160.44, 151.33, 148.78, 142.58, 138.97, 137.30, 135.99, 132.04, 131.40, 127.75, 126.55, 125.14, 124.77, 123.74, 122.59, 121.79, 120.40, 113.94, 111.60. MS (ESI+): exact mass calculated for C$_{21}$H$_{15}$Cl$_2$N$_5$O$_2$: 439.06, found: 440.25 [M+H] $^+$; purity (HPLC): 100 %.

4.1.41. 1-(2-((2,6-dichlorophenyl)amino)-2-oxoethyl)-N-(pyridin-2-yl)-1H-indazole-3-carboxamide (54)

Brown solid; yield: 83.9 %; melting point: 162 °C-164 °C; IR (neat, cm^{-1}): 3388.07, 3251.97, 1685.95, 1575.44, 1527.05, 1436.34; ^{1}H NMR (500 MHz, DMSO-*d$_6$*): δ (ppm) 10.42 (s, 1H), 9.73 (s, 1H), 8.40 (d, *J* = 4.8 Hz, 1H), 8.27 (t, *J* = 8.9 Hz, 2H), 7.91 (t, *J* = 7.8 Hz, 1H), 7.82 (d, *J* = 8.6 Hz, 1H), 7.56 (dd, *J* = 8.2, 3.9 Hz, 3H), 7.39 (dt, *J* = 20.7, 7.9 Hz, 2H), 7.20 (dd, *J* = 7.3, 4.9 Hz, 1H), 5.59 (s, 2H); MS (ESI+): exact mass calculated for C$_{21}$H$_{15}$Cl$_2$N$_5$O$_2$: 439.06, found: 440.25 [M+H]$^+$; purity (HPLC): 100 %.

4.1.42. 1-(2-((4-methoxyphenyl)amino)-2-oxoethyl)-N-(pyridin-2-yl)-1H-indazole-3-carboxamide (55)

White solid; yield: 80.2 %; melting point: 178 °C-180 °C; IR (neat, cm^{-1}): 3386.49, 3258.20, 1664.00, 1526.45, 1436.04, 1167.70, 772.78; ^{1}H NMR (500 MHz, DMSO-*d$_6$*): δ (ppm) 10.40 (s, 1H), 9.71 (s, 1H), 8.38 (dd, *J* = 5.0, 1.8 Hz, 1H), 8.27 (ddd, *J* = 8.3, 2.2, 1.0 Hz, 2H), 7.94–7.86 (m, 1H), 7.84 (d, *J* = 8.5 Hz, 1H), 7.59–7.49 (m, 3H), 7.40 (t, *J* = 7.5 Hz, 1H), 7.19 (dd, *J* = 7.3, 5.0 Hz, 1H), 6.95–6.87 (m, 2H), 5.50 (s, 2H), 3.73 (s, 3H). MS (ESI+): exact mass calculated for C$_{22}$H$_{19}$N$_5$O$_2$: 401.15, found: 402.35 [M+H]$^+$; purity (HPLC): 100 %.

4.1.43. 1-(2-((4-bromophenyl)amino)-2-oxoethyl)-N-(pyridin-2-yl)-1H-indazole-3-carboxamide (56)

White solid; yield: 86.2 %; melting point: 174 °C-176 °C; IR (neat, cm^{-1}): 3379.32, 3259.62, 1669.07, 1525.88, 1434.71, 1300.62, 771.36; ^{1}H NMR (500 MHz, DMSO-*d$_6$*): δ (ppm) 10.71 (s, 1H), 9.72 (s, 1H), 8.38 (dd, *J* = 5.0, 1.7 Hz, 1H), 8.26 (d, *J* = 8.2 Hz, 2H), 7.89 (td, *J* = 7.9, 1.9 Hz, 1H), 7.84 (d, *J* = 8.5 Hz, 1H), 7.62–7.49 (m, 6H), 7.40 (t, *J* = 7.5 Hz, 1H), 7.19 (dd, *J* = 7.3, 4.9 Hz, 1H), 5.54 (s, 2H); MS (ESI+): exact mass calculated for C$_{21}$H$_{16}$ BrN$_5$O$_2$: 449.04, found: 450.20 [M+H]$^+$ and 473.95 [M+Na]$^+$; purity (HPLC): 97.6 %.

4.1.44. 1-(2-((4-chlorophenyl) amino)-2-oxoethyl)-N-(pyridin-3-yl)-1H-indazole-3-carboxamide (57)

White solid; yield: 83.9 %; melting point: 157 °C-159 °C; IR (neat, cm^{-1}): 2937.36, 1682.68, 1539.44, 1490.53, 1167.77, 826.31; ^{1}H NMR (500 MHz, DMSO-*d$_6$*): δ (ppm) 10.71–10.67 (m, 1H), 10.64 (s, 1H), 9.07 (d, *J* = 2.9 Hz, 1H), 8.34–8.25 (m, 3H), 7.84 (d, *J* = 8.4 Hz, 1H), 7.67–7.56 (m, 2H), 7.54 (t, *J* = 7.7 Hz, 1H), 7.39 (dd, *J* = 12.5, 7.5 Hz, 4H), 5.56 (s, 2H); ^{13}C NMR (126 MHz, DMSO-*d$_6$*): δ 165.75, 161.32, 144.80, 142.56, 142.54, 137.92, 137.89, 135.94, 129.32, 127.81, 127.76, 127.54, 123.92, 123.37, 122.93, 122.08, 121.21, 111.41; MS (ESI+): exact mass calculated for C$_{21}$H$_{16}$ClN$_5$O$_2$: 405.09, found: 406.25 [M+H]$^+$; purity (HPLC): 97.9 %.

4.1.45. 1-(2-((4-bromophenyl)amino)-2-oxoethyl)-N-(pyridin-3-yl)-1H-indazole-3-carboxamide (58)

Brown solid; yield: 86.9 %; melting point: 182 °C-184 °C; IR (neat, cm^{-1}): 3254.18, 2933.90, 1673.40, 1537.82, 1487.45, 1279.10, 1164.61, 743.51; ^{1}H NMR (500 MHz, DMSO-*d$_6$*): δ (ppm) 10.70–10.66 (m, 1H), 10.64 (s, 1H), 9.06 (t, *J* = 2.0 Hz, 1H), 8.34–8.20 (m, 3H), 7.84 (d, *J* = 8.5 Hz, 1H), 7.58 (dd, *J* = 8.9, 1.6 Hz, 2H), 7.56–7.51 (m, 3H), 7.44–7.30 (m, 2H), 5.61 (s, 2H); MS (ESI+): exact mass calculated for C$_{21}$H$_{16}$BrN$_5$O$_2$, 449.05, found 450.20 [M+H]$^+$; purity (HPLC): 100 %.

4.1.46. N-phenyl-2-(3-phenyl-1H-indazol-1-yl)acetamide (59)

Yellow solid; yield: 72.3 %; melting point: 169 °C-171 °C; ^{1}H NMR (500 MHz, DMSO-*d$_6$*): δ (ppm) 10.48 (s, 1H), 8.30 (s, 1H), 8.09 (d, *J* = 8.2 Hz, 1H), 8.00–7.95 (m, 2H), 7.73 (d, *J* = 8.5 Hz, 1H), 7.63–7.57 (m, 2H), 7.57–7.39 (m, 3H), 7.36–7.24 (m, 3H), 7.07 (t, *J* = 7.4 Hz, 1H), 5.40 (s, 2H); MS (ESI+): exact mass calculated for C$_{21}$H$_{17}$N$_3$O: 327.13, found: 328.15 [M+H]$^+$; purity (HPLC): 99.8 %.

4.1.47. 2-(3-Phenyl-1H-indazol-1-yl)-N-(o-tolyl)acetamide (60)

Yellow solid; yield: 77.12; melting point: 169 °C-171 °C; ^{1}H NMR

(500 MHz, DMSO-d_6): δ (ppm) 8.06 (d, J = 8.2 Hz, 1H), 7.95 (d, J = 7.6 Hz, 2H), 7.70 (d, J = 8.5 Hz, 1H), 7.50 (t, J = 7.7 Hz, 3H), 7.38 (dd, J = 12.5, 7.6 Hz, 2H), 7.25–7.03 (m, 5H), 5.41 (s, 2H), 2.21 (s, 3H); MS (ESI+): exact mass calculated for $C_{22}H_{19}N_3O$: 341.15, found: 342.15 [M+H]$^+$; purity (HPLC): 98.8 %.

4.1.48. 2-(3-Phenyl-1H-indazol-1-yl)-N-(p-tolyl)acetamide (61)

White solid; yield: 72.2 %; melting point: 163 °C-165 °C; ^{1}H NMR (500 MHz, DMSO-d_6): δ (ppm) 8.26–8.06 (m, 3H), 8.02 (d, J = 8.1 Hz, 2H), 7.89 (s, 1H), 7.72 (d, J = 8.5 Hz, 1H), 7.45 (dd, J = 14.9, 7.7 Hz, 3H), 7.29 (d, J = 7.7 Hz, 1H), 7.07 (d, J = 8.1 Hz, 2H), 5.39 (s, 2H), 2.19 (s, 3H); MS (ESI+): exact mass calculated for $C_{22}H_{19}N_3O$: 341.15, found: 342.15 [M+H]$^+$; purity (HPLC): 99.8 %.

4.1.49. N-(4-fluorophenyl)-2-(3-phenyl-1H-indazol-1-yl)acetamide (62)

Beige solid; yield: 78.6 %; melting point: 189 °C-191 °C; ^{1}H NMR (500 MHz, DMSO-d_6): δ (ppm) 10.53 (s, 1H), 8.05 (d, J = 8.2 Hz, 1H), 7.97–7.90 (m, 2H), 7.69 (d, J = 8.5 Hz, 1H), 7.62–7.55 (m, 2H), 7.53–7.46 (m, 2H), 7.46–7.36 (m, 2H), 7.23 (t, J = 7.5 Hz, 1H), 7.13 (dd, J = 10.1, 7.7 Hz, 2H), 5.36 (s, 2H); MS (ESI+): exact mass calculated for $C_{21}H_{16}FN_3O$: 345.12, found: 346.10 [M+H]$^+$; purity (HPLC): 99.2 %.

4.1.50. N-(3,4-dichlorophenyl)-2-(3-phenyl-1H-indazol-1-yl)acetamide (63)

Beige solid; yield: 78.6 %; melting point: 189 °C-191 °C; ^{1}H NMR (400 MHz, DMSO-d_6): δ (ppm) 10.76 (s, 1H), 8.06 (d, J = 8.2 Hz, 1H), 7.97–7.90 (m, 3H), 7.69 (d, J = 8.5 Hz, 1H), 7.56 (d, J = 8.8 Hz, 1H), 7.53–7.36 (m, 4H), 7.23 (t, J = 7.5 Hz, 1H), 5.39 (s, 2H); MS (ESI+): exact mass calculated for $C_{21}H_{15}Cl_2N_3O$: 395.05, found: 396.00 [M+H]$^+$; purity (HPLC): 99.2 %.

4.1.51. 2-(3-(4-(methyl sulfonyl) phenyl)-1H-indazol-1-yl)-N-phenylacetamide (64)

Yellow solid; yield: 75.6 %; melting point: 174 °C-76 °C; ^{1}H NMR (400 MHz, DMSO-d_6): δ (ppm) 10.44 (s, 1H), 8.05 (d, J = 8.2 Hz, 1H), 7.94 (dt, J = 6.4, 1.4 Hz, 1H), 7.69 (dd, J = 8.5, 3.2 Hz, 1H), 7.59–7.30 (m, 6H), 7.28–7.18 (m, 1H), 7.08 (d, J = 8.0 Hz, 2H), 5.32 (d, J = 23.0 Hz, 2H), 2.21 (s, 3H); MS (ESI+): exact mass calculation for $C_{22}H_{19}N_3O_3S$: 405.11, found: 406.20 [M+H]$^+$; purity (HPLC): 99.1 %.

4.1.52. 2-(3-(4-(methyl sulfonyl) phenyl)-1H-indazol-1-yl)-N-(o-tolyl)acetamide (65)

Brown solid; yield: 77.3 %; melting point: 187 °C-189 °C; ^{1}H NMR (500 MHz, DMSO-d_6): δ (ppm) 9.77 (s, 1H), 8.29–8.17 (m, 3H), 8.08 (dq, J = 37.5, 8.3 Hz, 4H), 7.75 (d, J = 8.3 Hz, 1H), 7.66–7.36 (m, 2H), 7.34–7.01 (m, 3H), 5.47 (s, 1H), 3.24 (d, J = 4.3 Hz, 6H); MS (ESI+): exact mass calculated for $C_{23}H_{21}N_3O_3S$: 419.13, found: 420.20 [M+H]$^+$; purity (HPLC): 98.2 %.

4.1.53. 2-(3-(4-(methyl sulfonyl) phenyl)-1H-indazol-1-yl)-N-(p-tolyl)acetamide (66)

White solid; yield: 79.2 %; melting point: 169 °C-171 °C; ^{1}H NMR (500 MHz, DMSO-d_6): δ (ppm) 10.48 (s, 1H), 8.27–8.18 (m, 2H), 8.14 (d, J = 8.4 Hz, 1H), 8.06–7.99 (m, 2H), 7.73 (d, J = 8.5 Hz, 1H), 7.59–7.53 (m, 2H), 7.50–7.44 (m, 1H), 7.29 (td, J = 7.7, 3.7 Hz, 3H), 7.04 (t, J = 7.4 Hz, 1H), 5.42 (s, 2H), 3.22 (s, 3H); MS (ESI+): exact mass calculation for $C_{23}H_{21}N_3O_3S$, 419.13: found: 420.20 [M+H]$^+$; purity (HPLC): 100 %.

4.1.54. N-(4-fluorophenyl)-2-(3-(4-(methylsulfonyl)phenyl)-1H-indazol-1-yl) acetamide (67)

Yellow solid; yield: 75.2 %; melting point: 194 °C-196 °C; ^{1}H NMR (500 MHz, DMSO-d_6): δ (ppm) 10.54 (s, 1H), 8.27–8.21 (m, 2H), 8.14 (dt, J = 8.4, 1.1 Hz, 1H), 8.07–8.00 (m, 2H), 7.78–7.71 (m, 1H), 7.63–7.54 (m, 2H), 7.48 (ddd, J = 8.3, 7.0, 1.1 Hz, 1H), 7.35–7.26 (m, 1H), 7.17–7.10 (m, 2H), 5.41 (s, 2H), 3.23 (s, 3H); MS (ESI+): exact

mass calculated for $C_{22}H_{18}FN_3O_3S$: 423.10, found: 424.20 [M+H]$^+$; purity (HPLC): 97.6 %.

4.1.55. N-(3,4-dichlorophenyl)-2-(3-(4-(methylsulfonyl)phenyl)-1H-indazol-1-yl)acetamide (68)

Yellow solid; yield: 75.2 %; melting point: 182 °C-184 °C; ^{1}H NMR (500 MHz, DMSO-d_6): δ (ppm) 10.80 (s, 1H), 8.28–8.20 (m, 2H), 8.15 (d, J = 8.3 Hz, 1H), 8.08–8.00 (m, 2H), 7.93 (d, J = 2.5 Hz, 1H), 7.74 (d, J = 8.5 Hz, 1H), 7.55 (d, J = 8.9 Hz, 1H), 7.52–7.44 (m, 2H), 7.33–7.25 (m, 1H), 5.45 (s, 2H), 3.24 (s, 3H); ^{13}C NMR (126 MHz, DMSO-d_6): δ 166.92, 161.94, 140.13, 138.86, 133.74, 131.45, 131.33, 131.22, 129.65, 128.22, 127.75, 125.69, 121.30, 120.65, 120.14, 115.68, 44.35; MS (ESI+): exact mass calculated for $C_{22}H_{17}Cl_2N_3O_3S$: 473.03, found: 474.10 [M+H]$^+$; purity (HPLC): 99.7 %.

4.1.56. (E)-1-Benzyl-N'-benzylidene-1H-indazole-3-carbohydrazide (69)

White solid; yield: 70.2 %; melting point: 198 °C-200 °C; ^{1}H NMR (500 MHz, DMSO-d_6): δ (ppm) 11.98 (s, 1H), 8.59 (s, 1H), 8.23 (d, J = 8.1 Hz, 1H), 7.81 (d, J = 8.5 Hz, 1H), 7.71 (d, J = 7.2 Hz, 2H), 7.52–7.39 (m, 4H), 7.37–7.23 (m, 6H), 5.81 (s, 2H); MS (ESI+): exact mass calculated for $C_{22}H_{18}N_4O$: 354.14, found: 355.20 [M+H]$^+$ and 377.20 [M+Na]$^+$; purity (HPLC): 95.2 %.

4.1.57. (E)-N'-benzylidene-1-(4-fluorobenzyl)-1H-indazole-3-carbohydrazide (70)

White solid; yield: 71.5 %; melting point: 178 °C-180 °C; ^{1}H NMR (500 MHz, DMSO-d_6): δ (ppm) 11.98 (s, 1H), 8.59 (s, 1H), 8.22 (d, J = 8.2 Hz, 1H), 7.83 (d, J = 8.5 Hz, 1H), 7.72 (d, J = 7.1 Hz, 2H), 7.46 (h, J = 7.1 Hz, 4H), 7.34 (dt, J = 14.9, 7.1 Hz, 3H), 7.17 (t, J = 8.8 Hz, 2H), 5.80 (s, 2H); MS (ESI+): exact mass calculated for $C_{22}H_{17}FN_4O$: 372.13, found: 373.20 [M+H]$^+$ and 395.20 [M+Na]$^+$; purity (HPLC): 98.7 %.

4.1.58. 1-Benzyl-N'-((1E,2E)-3-phenylallylidene)-1H-indazole-3-carbohydrazide (71)

White solid; yield: 71.0 %; melting point: 165 °C-167 °C; ^{1}H NMR (500 MHz, DMSO-d_6): δ (ppm) 11.92 (s, 1H), 8.37 (d, J = 8.9 Hz, 1H), 8.21 (d, J = 8.1 Hz, 1H), 7.80 (d, J = 8.5 Hz, 1H), 7.63 (d, J = 7.5 Hz, 2H), 7.51–7.23 (m, 11H), 7.08 (dd, J = 16.2, 8.8 Hz, 1H), 6.99 (d, J = 16.1 Hz, 1H), 5.81 (s, 2H); MS (ESI+): exact mass calculated for $C_{24}H_{20}N_4O$: 380.16, found: 381.20 [M+H]$^+$ and 403.20 [M+Na]$^+$; purity (HPLC): 98.1 %.

4.1.59. 1-(4-fluorobenzyl)-N'-((1E,2E)-3-phenylallylidene)-1H-indazole-3-carbohydrazide (72)

White solid; yield: 76.2 %; melting point: 172 °C-174 °C; ^{1}H NMR (500 MHz, DMSO-d_6): δ (ppm) 11.91 (s, 1H), 8.37 (d, J = 8.8 Hz, 1H), 8.21 (d, J = 8.1 Hz, 1H), 7.82 (d, J = 8.5 Hz, 1H), 7.63 (d, J = 7.5 Hz, 2H), 7.48 (t, J = 7.8 Hz, 1H), 7.43–7.27 (m, 7H), 7.21–7.11 (m, 2H), 7.08 (dd, J = 16.2, 8.8 Hz, 1H), 6.99 (d, J = 16.1 Hz, 1H), 5.79 (s, 2H); MS (ESI+): exact mass calculated for $C_{24}H_{19}FN_4O$: 398.15, found: 399.20 [M+H]$^+$ and 421.20 [M+Na]$^+$; purity (HPLC): 98.2 %.

4.1.60. (E)-N'-(3,4-dihydroxybenzylidene)-1-(4-fluorobenzyl)-1H-indazole-3-carbohydrazide (73)

White solid; yield: 71.4 %; melting point: 183 °C-185 °C; ^{1}H NMR (500 MHz, DMSO-d_6) δ (ppm) 11.70 (s, 1H), 9.38 (s, 1H), 9.28 (s, 1H), 8.38 (s, 1H), 8.21 (d, J = 8.2 Hz, 1H), 7.82 (d, J = 8.5 Hz, 1H), 7.47 (t, J = 7.7 Hz, 1H), 7.34 (ddd, J = 17.4, 11.6, 6.6 Hz, 3H), 7.23 (d, J = 2.0 Hz, 1H), 7.16 (t, J = 8.1 Hz, 2H), 6.91 (dd, J = 8.3, 2.0 Hz, 1H), 6.78 (d, J = 8.1 Hz, 1H), 5.78 (s, 2H); MS (ESI+): Exact mass calculated for $C_{22}H_{17}FN_4O$: 404.13, found: 405.20 [M+H]$^+$ and 427.20 [M+Na]$^+$; purity (HPLC): 98.2 %.

4.1.61. (E)-1-Benzyl-N'-(3,4-dimethoxybenzylidene)-1H-indazole-3-carbohydrazide (74)

White solid; yield: 80.1 %; melting point: 185 °C-187 °C; ^{1}H NMR

(500 MHz, DMSO-d_6): δ (ppm) 11.86 (s, 1H), 8.50 (s, 1H), 8.22 (d, J = 8.1 Hz, 1H), 7.81 (d, J = 8.4 Hz, 1H), 7.47 (t, J = 8.0 Hz, 1H), 7.30 (dd, J = 17.4, 8.4 Hz, 8H), 7.16 (d, J = 8.3 Hz, 1H), 7.03 (d, J = 8.2 Hz, 1H), 5.80 (s, 2H), 3.81 (d, J = 9.3 Hz, 6H); MS (ESI+): Exact mass calculated for $C_{24}H_{22}N_4O_3$: 414.17, found: 415.20 [M+H]$^+$ and 437.20 [M+Na]$^+$; purity (HPLC): 97.4 %.

4.1.62. (E)-N'-(3,4-dimethoxybenzylidene)-1-(4-fluorobenzyl)-1H-indazole-3-carbohydrazide (75)

White solid; yield: 72.4 %; melting point: 188 °C-190 °C; ^{1}H NMR (500 MHz, DMSO-d_6): δ (ppm) 11.85 (d, J = 3.9 Hz, 1H), 8.51 (d, J = 3.8 Hz, 1H), 8.21 (d, J = 8.0 Hz, 1H), 7.83 (d, J = 8.3 Hz, 1H), 7.48 (t, J = 7.6 Hz, 1H), 7.34 (h, J = 7.5, 6.4 Hz, 4H), 7.22–7.11 (m, 3H), 7.03 (d, J = 8.1 Hz, 1H), 5.79 (d, J = 3.6 Hz, 2H), 3.82 (dd, J = 9.2, 3.6 Hz, 6H); MS (ESI+): exact mass calculated for $C_{24}H_{21}FN_4O_3$: 432.16, found: 433.20 [M+H]$^+$ and 454.20 [M+Na]$^+$; purity (HPLC): 96.8 %.

4.1.63. (E)-1-(4-fluorobenzyl)-N'-(4-fluorobenzylidene)-1H-indazole-3-carbohydrazide (76)

White solid; yield: 70.4 %; melting point: 162 °C-164 °C; ^{1}H NMR (500 MHz, DMSO-d_6): δ (ppm) 11.98 (s, 1H), 8.59 (s, 1H), 8.22 (d, J = 8.2 Hz, 1H), 7.83 (d, J = 8.5 Hz, 1H), 7.77 (dd, J = 8.5, 5.5 Hz, 2H), 7.48 (t, J = 7.7 Hz, 1H), 7.40–7.26 (m, 6H), 7.21–7.11 (m, 2H), 5.79 (s, 2H); MS (ESI+): exact mass calculated for $C_{22}H_{16}F_2N_4O$: 390.13, found: 391.15 [M+H]$^+$ and 413.15 [M+Na]$^+$; purity (HPLC): 97.2 %.

4.1.64. (E)-1-Benzyl-N'-(2-chlorobenzylidene)-1H-indazole-3-carbohydrazide (77)

White solid; yield: 70.1 %; melting point: 187 °C-189 °C; ^{1}H NMR (500 MHz, DMSO-d_6): δ (ppm) 12.32 (s, 1H), 9.02 (s, 1H), 8.23 (d, J = 8.2 Hz, 1H), 8.08–8.00 (m, 1H), 7.82 (d, J = 8.4 Hz, 1H), 7.56–7.41 (m, 4H), 7.31 (dq, J = 11.6, 5.8, 4.4 Hz, 6H), 5.82 (s, 2H); MS (ESI+): exact mass calculated for $C_{12}H_{17}ClN_4O$: 388.11; found: 389.15 [M+H]$^+$ and 411.5 [M+Na]$^+$; purity (HPLC): 95.9 %.

4.1.65. (E)-N'-(2-chlorobenzylidene)-1-(4-fluorobenzyl)-1H-indazole-3-carbohydrazide (78)

White Solid; yield: 76.2 %; melting point: 183 °C-185 °C; ^{1}H NMR (500 MHz, DMSO-d_6): δ (ppm) 12.32 (s, 1H), 9.02 (s, 1H), 8.22 (d, J = 8.1 Hz, 1H), 8.04 (t, J = 4.9 Hz, 1H), 7.84 (d, J = 8.5 Hz, 1H), 7.57–7.44 (m, 2H), 7.45 (dd, J = 6.4, 3.3 Hz, 2H), 7.41–7.29 (m, 3H), 7.17 (td, J = 8.9, 2.0 Hz, 2H), 5.80 (s, 2H).; MS (ESI+): exact mass calculated for $C_{22}H_{16}ClFN_4O$, 404.10, found: 407.15 [M+H]$^+$ and 429.15 [M+Na]$^+$; purity (HPLC): 97.3 %.

4.1.66. (E)-N'-(4-bromobenzylidene)-1-(4-fluorobenzyl)-1H-indazole-3-carbohydrazide (79)

White solid; yield: 70.4 %; melting point: 187 °C-189 °C; ^{1}H NMR (500 MHz, DMSO-d_6): δ (ppm)12.06 (s, 1H), 8.56 (s, 1H), 8.22 (d, J = 8.1 Hz, 1H), 7.84 (d, J = 8.5 Hz, 1H), 7.67 (s, 4H), 7.49 (t, J = 7.7 Hz, 1H), 7.34 (td, J = 11.6, 10.2, 6.5 Hz, 3H), 7.17 (t, J = 8.7 Hz, 2H), 5.80 (s, 2H).; MS (ESI+): exact mass calculated for $C_{22}H_{16}BrFN_4O$, 450.05, found: 451.10 [M+H]$^+$ and 473.10 [M+Na]$^+$; purity (HPLC): 100 %.

4.2. Biological evaluation

4.2.1. Materials

The reference MCT1 inhibitor **80** has been synthesized in-house [82]. The reference MCT1 inhibitor **81**, the ABCB1 and ABCA1 reference inhibitors **82**, the reference ABCG2 inhibitor **84**, as well as the ABCC10 reference inhibitor cepharanthine were obtained from Sigma-Aldrich (St. Louis, MO, USA). The ABCC1 reference inhibitor **83** was synthesized as reported previously [66]. The SLC and ABC transporter tracers 3-BP, rhodamine 123, Hoechst 33342, MPP$^+$, SR101, DHPDS, pyranine, and ASP$^+$ as well as the antineoplastic agents doxorubicin, SN-38, and paclitaxel as well as MTT were purchased from Sigma-Aldrich (St. Louis, MO, USA). The fluorescence dyes calcein AM, daunorubicin, and pheophorbide A were received from Calbiochem (EMD Chemicals, San Diego, USA), EMD Millipore (Billerica, MA, USA), and Cayman Chemicals (Ann Arbor, MI, USA), respectively. All other chemicals were obtained from Sigma Aldrich (St. Louis, MO, USA) and VWR (Radnor, PA, USA). Compounds **15–79** were stored at −20 °C as 10 mM stock solutions. Dilution series and the experimental cell culture were performed in either in DPBS (Cell Clone, Genetix Biotech Asia, India), phenol red-free Dulbecco's modified eagle media (DMEM; GE Healthcare, Chicago, IL, USA), phenol red-free RPMI-1640 (GE Healthcare, Chicago, IL, USA), or in-house produced PBD (Budapest, Hungary) without additional supplements.

4.2.2. Cell culture

The MCT1-expressing lung and breast cancer cell lines A-549 and MCF-7, the MCT4-expressing breast cancer cell line MDA-MB-231, as well as the non-MCT1-and non-MCT4-expressing, non-cancerous murine embryonic cell line NIH/3T3 were obtained from the National Centre for Cell Science (NCCS; Pune, India) [43]. The ABCB1-, ABCC1-, and ABCG2-expressing cell lines A2780/ADR, H69AR, and MDCK II BCRP as well as their sensitive counterparts were a generous gift from Prof. Dr. Finn K. Hansen and Prof. Dr. Gerd Bendas (Pharmaceutical and Cell-biological Chemistry, University of Bonn, Germany). The NAT-, DAT, SERT, OCT1, and OCT2-expressing HEK293 cells were generated by stable transfection using the Flp-In system (ThermoFisher Scientific, Waltham, MA, US) as described in the literature [83]. The OCT3-expressing cell line HEK293 OCT3 was a generous gift from Prof. Dr. Hermann Koepsell (Institute of Anatomy and Cell Biology, University of Würzburg, Germany) and Prof. Dr. Valentin Gorboulev (Julius-von-Sachs-Institute of Biosciences, University of Würzburg, Germany). The epidermoid carcinoma cell line A431 engineered with lentiviral transfection (OATP1A2, OATP1B1, OATP1B3) or transposon-mediated genome integration (OATP2B1) to stably overexpress OATP1A2, OATP1B1, OATP1B3 or OATP2B1, as well as their mock transfected controls were applied as described in the literature [65,84]. ABCA1-expressing murine J774A.1 cells were obtained from American Type Culture Collection (ATCC, Manassas, VA, USA). The ABCC10-expressing HEK293 MRP7 cells were established by transfection as reported earlier [41].

A-549 [43], MCF-7 [43], NIH/3T3 [43], MDCK II [17,26,28,43, 57–59,66], HEK293 [41,83], A431 [65,84], J774.A1 [27], as well as MDA-MB-231 [43] cells were cultured in DMEM cell culture media (Genetix Biotech Asia, New Delhi, India; Biowest, Nuaillé, France; Gibco, ThermoFisher Scientific, Waltham, MA, US; and Hyclone, Logan, UT, USA) supplemented with 10 % fetal bovine serum (FBS; HiMedia Laboratories Pvt. Ltd, Maharashtra, India; Biowest, Nuaillé, France; Sigma, Budapest, Hungary; and Hyclone, Logan, UT, USA). A2780/ADR [17,26,28,43,57–59,66] and H69AR [17,26,28,43,57–59,66] cells and their sensitive counterparts were cultivated using RPMI-1640 cell culture media (Biowest, Nuaillé, France) supplemented with 10 % and 20 % FBS (Biowest, Nuaillé, France), respectively. A-549, MCF-7, NIH/3T3, A2780/ADR, A2780, H69AR, H69, MDCK II BCRP, MDCK II, HEK 293 cells were also supplemented with streptomycin (50 μg/μL), penicillin G (50 U/mL; Genetix Biotech Asia, New Delhi, India; and Biowest, Nuaillé, France), while A431 and HEK293 cells were supplemented with streptomycin (100 μg/μL), penicillin G (100 U/mL; Sigma-Merck, Darmstadt, Germany; Hyclne, Logan, UT, USA; and ThermoFisher Scientific, Waltham, MA, US). All cells were additionally complemented with L-glutamine (2 mM; Genetix Biotech Asia, New Delhi, India; Biowest, Nuaillé, France; Sigma-Merck, Darmstadt, Germany; and ThermoFisher Scientific, Waltham, MA, US). The cells were stored under liquid nitrogen (media/FBS: 90 %; DMSO: 10 %) and cultivated at 37 °C under 5 % CO_2-humidified atmosphere. A trypsin-EDTA solution (0.05 %/0.02 %; HiMedia Laboratories Pvt. Ltd, Maharashtra, India; Biowest, Nuaillé, France; and ThermoFisher Scientific, Waltham, MA, US) was used to detach the cells for either sub-culturing or biological evaluation at a

confluence of ~90 %, followed by washing steps and addition of fresh cell culture media. Cell counting was performed with either a TC20 Automated Cell Counter (Bio-Rad, Berkeley, CA, USA), a Scepter handheld automated cell counter (60 µM capillary sensor; EMD Millipore, Billerica, MA, USA), or a Neubauer cell counting chamber (ThermoFisher Scientific, Waltham, MA, US).

4.2.3. Inhibitory activity against MCT1

A functional 3-BP cytotoxicity assay was performed as described previously [43]. Ten microliters of each test concentration of compounds **15–79** was pipetted into colourless flat-bottom 96-well microplates (SPL Life Sciences, Gyeonggi-do, Republic of Korea), supplemented with 180 µL of a A-549 cell suspension (5000 cells/well). After incubation for 12 h, 10 µL 3-BP (1 mM; final concentration: 50 µM per well) and the test compounds were added at various concentrations. After an incubation period of 72 h at 37 °C and 5 % CO_2-humidified atmosphere, the cell viability was assessed as described before [43] adding 20 µL MTT solution (5 mg/mL) into each well followed by 1 h incubation. After removal of the supernatant, 100 µL of DMSO was added into each well and the absorbance was determined at 570 nm using a SpectraMax® iD3 Multi-Mode Microplate Reader (Molecular Devices, San Jose, CA, USA) with a background correction at 690 nm.

4.2.4. Inhibitory activity against ABCB1, ABCC1, ABCG2, and ABCA1

Calcein AM (ABCB1) [17,26,28,43,56–59,66], daunorubicin (ABCB1 [26,28,43] and ABCC1 [26,28,43,56,57,66]), rhodamine 123 (ABCC1) [56], pheophorbide A (ABCG2) [17,26,28,43,56–59,66], Hoechst 33342 (ABCG2) [26,28,57–59], and 25-NBD-cholesterol (ABCA1) [27,35] assays were conducted as reported earlier. Twenty microliters of each test concentration of compounds **15–79** were pipetted into clear (calcein AM, daunorubicin, rhodamine 123, pheophorbide A, and 25-NBD-cholesterol) or black (Hoechst 33342) 96-well flat-bottom plates (Brand, Wertheim, Germany), followed by addition of 160 µL cell suspension containing either 30,000 cells/well (calcein AM and Hoechst 33342) or 45,000 cells/well (daunorubicin, rhodamine 123, pheophorbide A, and 25-NBD-cholesterol) in either phenol red-free RPMI-1640 (A2780/ADR and H69AR) or phenol red-free DMEM (MDCK II BCRP) without further supplements. In contrast, the J774A.1 cell suspension contained all supplements due to the long incubation period. The compounds were pre-incubated with the cells for 30 min (calcein AM, daunorubicin, pheophorbide A, and Hoechst 33342) or 24 h (25-NBD-cholesterol) followed by adding of the respective fluorescence dye [20 µL of calcein AM (3.125 µM), daunorubicin (30 µM), rhodamine (3 µM), pheophorbide A (5 µM), Hoechst 33342 (10 µM), or 25-NBD-cholesterol (10 µM)], resulting in final concentrations of 0.3125 µM (calcein AM), 3 µM (daunorubicin), 0.3 µM (rhodamine 123), 0.5 µM (pheophorbide A), 1 µM (Hoechst 33342), and 1 µM (25-NBD-cholesterol), respectively, in each well. The increase of fluorescence was assessed within 30 min in 30 s intervals in the calcein AM assay (excitation: 485 nm; emission: 520 nm) applying a Paradigm microplate reader (Beckman Coulter, Brea, CA, USA), while the average steady-state fluorescence per well was determined after incubation (180 min: daunorubicin, rhodamine 123, and pheophorbide A; Hoechst 33342: 120 min; 25-NBD-cholesterol: 48 h) at an excitation of 360 nm (Hoechst 33342) and 488 nm (daunorubicin, rhodamine 123, pheophorbide A, and NBD-cholesterol), as well as an emission of 530/30 (rhodamine 123 and 25-NBD-cholesterol) and 695/50 (daunorubicin and pheophorbide A), applying either an Attune NxT flow cytometer (Invitrogen, Waltham, MA, USA; daunorubicin, rhodamine 123, pheophorbide A, or 25-NBD-cholesterol) or a Paradigm microplate reader (Hoechst 33342).

4.2.5. Inhibitory activity against NAT, DAT, SERT, and OCT1–3

Forty-eight hours prior to the experiment, 300,000 transfected HEK293 cells per well were plated in poly-ᴅ-lysine pre-coated 24-well plates (Greiner Bio-One, Kremsmünster, Austria). Every plate contained two wells of empty vector-transfected cells as a control to account

for transporter-independent uptake of the probe substrate. On the day of the experiment, the cells were washed once with pre-warmed (37 °C) Hanks' Balanced Salt solution (HBSS; ThermoFisher Scientific, Darmstadt, Germany) supplemented with 10 mM HEPES at pH 7.4 (Sigma-Aldrich, Taufkirchen, Germany), hereafter referred to as HBSS$^+$. The cells were subsequently incubated with 2 µM of the probe substrates MPP$^+$ for NAT, DAT, and SERT or ASP$^+$ (Sigma-Aldrich, Taufkirchen, Germany) for OCT1–3 in the presence or absence of the test compound in HBSS$^+$ for 5 min. The incubation was stopped by adding ice-cold HBSS$^+$, and the cells were subsequently washed twice with ice-cold HBSS$^+$. The cells were then lysed using 80 % acetonitrile (LGC Standards, Wesel, Germany) for 10 min on a 3D platform shaker (Heidolph, Schwabach, Germany). For ASP$^+$, the lysate was then transferred into a black 96-well plate and fluorescence intensity was measured using a Tecan Ultra fluorescence microplate reader (Tecan, Crailsheim, Germany; excitation: 482 nM; emission: 612 nm). For MPP$^+$, the lysate was centrifuged for 15 min and 50 µL of the supernatant were transferred into a 96-well MTP-block. The 80 % acetonitrile was subsequently evaporated to dryness at 40 °C under nitrogen flow and the samples redissolved in 200 µL of 0.1 % (v/v) methanoic acid. MPP$^+$ isolation was achieved using a Brownlee SPP RP-amide column (4.6 × 100 mm inner dimension with 2.7 µm particle size) with a C18 pre-column in a Shimadzu Nexera HPLC system with a SIL-30AC autosampler, a CTO-20AC column oven, a LC-30AD pump, and a CBM-20A controller (Shimadzu, Kyoto, Japan). The mobile phase consisted to 80 % of 0.1 % (v/v) methanoic acid, 17.2 % (v/v) acetonitrile, and 2.8 % methanol (6:1) at a flow rate of 0.3 mL/min and an oven temperature of 40 °C. Detection was carried out with a coupled an API 4000 tandem mass spectrometer (AB SCIEX, Darmstadt, Germany) operating in MRM mode. The retention time was 3.5 min, the first quadrupole mass was 179.016 Da, the third quadrupole mass was 128.1 (102.2) Da, the declustering potential was 10 V, the collision energy 42 (63) V, and the collision cell exit potential 8 (6) V. Fenoterol was used as internal standard. Analyte peaks were integrated and quantified using the Analyst software (version 1.6.2, AB SCIEX, Darmstadt, Germany).

4.2.6. Inhibitory activity against OATP1A2, OATP1B1, OATP1B3, and OATP2B1

Inhibition of OATP-mediated transport was measured in the linear phase of the probe substrate uptake as described earlier [63,65]. Briefly, A431 cells with OATP expression or mock control (80,000 cell/well) were seeded into 96-well plates (SPL Life Sciences, Pocheon-si, Republic of Korea) in 200 µL cell culture medium. After 16–24 h, the cells were washed three times with 200 µL of in-house phosphate buffered saline (PBS) and pre-incubated with the tested compounds for 5 min at 37 °C in 50 µL HBSS, pH 7.4; OATP1A2, OATP1B1, OATP) or uptake buffer (pH 5.5; OATP2B1) [84]. The reaction was started by the addition of 50 µL of the probe substrates, SR101 (OATP1A; Sigma-Merck, Darmstadt, Germany; final concentration: 1 µM) DHPDS (OATP1B1 and OATP1B3; Sigma-Merck, Darmstadt, Germany; final concentration: 10 µM), and pyranine (OATP2B1; Sigma-Merck, Darmstadt, Germany; final concentration: 20 µM), and the cells were further incubated at 37 °C for 10 min (OATP1A2, OATP1B1, and OATP1B3) or 15 min (OATP2B1). The reaction was stopped by removing the supernatant, and then the cells were washed three times with ice-cold PBS. Fluorescence of the intracellularly accumulated dye was determined using an Enspire plate reader (PerkinElmer, Waltham, MA) at an excitation wave length of 586 nm (SR101) or 460 nm (DHPDS and pyranine) with an emission wave length of 605 nm (SR101) or 510 nm (DHPDS and pyranine).

4.2.7. MDR reversal assay against MCT1, ABCB1, ABCC1, ABCG2, MCT4, and ABCC10

The ability of compounds **15–16**, **18–20**, **53**, **57**, and **68**, as well as **31–32** to reverse MDR mediated by MCT1, ABCB1, ABCC1, ABCG2, MCT4 and ABCC10 toward doxorubicin (MCT1, ABCB1, ABCC1, MCT4) [43,59], SN-38 (ABCG2) [43,58,59,66], and paclitaxel (ABCC10) [85]

was assessed using A-549, A2780/ADR, H69AR, MDCK II BCRP, MDA-MD-231, and HEK293 MRP7 applying an MTT-based cell viability assay. Ten (MCT1 and MCT4) or 20 (ABCB1, ABCC1, and ABCG2) microliters of the test compounds at various concentrations were added to colourless flat-bottom 96-well microplates, followed by addition of 180 μL (MCT1 and MCT4) or 160 μM (ABCB1, ABCC1, and ABCG2) cell suspension containing 3000 (MDCK II BCRP), 5000 (A-549 and MDA-MB-231), 10,000 (A2780/ADR), or 20,000 (H69AR) cells per well. Ten (MCT1 and MCT4) or 20 (ABCB1, ABCC1, and ABCG2) microliters of the antineoplastic agents doxorubicin (MCT1, MCT4, ABCB1, and ABCC1), and SN-38 (ABCG2), were added at various concentrations. Incubation was performed for 72 h at 37 °C and 5 % CO_2-humidified atmosphere before cell viability was assessed using MTT as stated above. In case of the ABCC10 MDR reversal assay, 160 μL of a suspension containing either HEK293 MRP7 or HEK293/pcDNA3.1 cells (5000 cells per well) were pipetted into clear, flat-bottom 96-well plates and pre-incubated overnight before adding 20 μL of the test compounds and 20 μL of paclitaxel. After an incubation phase of 68 h, 20 μL μM MTT (4 mg/mL) was added and the mixture was further incubated for 4 h before spectrophotometric assessment of cell viability as described above.

4.2.8. Determination of cell toxicity of hit compounds against MCT1-expressing cancer cell lines

To determine growth inhibition by compounds **15–16**, **18–20**, **53**, **57**, and **68**, 20 μM of the respective compound at a concentration range between 1 μM and 100 μM (A-549 or MCF-7), or at a concentration of 10 μM and 50 μM (NIH/3T3) was transferred into colourless flat-bottom 96-well microplates. After addition of a cell suspension containing 5000 A-549, MCF-7, or NIH/3T3 cells per well (180 μL) an incubation period of 72 h followed at 37 °C under 5 % CO_2-humidified atmosphere. The cell viability as well as the GI_{50} values were determined as described above.

4.2.9. Blind molecular docking

In order to explore the proposed multitarget binding sites [17,23, 26–28] of the herein assessed indazoles, the cryo-EM structures of nine available transporters human MCT1 [67] (PDB ID 6LZ0), human ABCB1 [68] (PDB ID 7O9W), bovine ABCC1 [69] (PDB ID 8F4B), human ABCG2 [70] (PDB ID 8BHT), human OATP1B1 [71] (PDB ID 8K6L), human OATP1B3 [72] (PDB ID 8PG0), human OCT2 [73] (PDB ID 8ET9), human OCT3 [74] (PDB ID 7ZH6), and human ABCA1 [75] (PDB ID 7TDT)] were downloaded from the RCSB Protein Data Bank (https://www.rcsb.org) [86] and processed using CCG Molecular Operating Environment (MOE) version 2022.02 [87]. Co-crystallized molecules were removed and ionization states assigned. Hydrogen atoms were added using the Protonate-3D tool implemented in MOE. Subsequently, the structures were energy-minimized while keeping the heavy atoms fixed at their crystallographic positions, applying the Amber99 force field [88] until the root-mean-square of the conjugate gradient was less than 0.05 kcal mol^{-1} Å^{-1}. The docking calculations were performed using the particle swarm optimization (PSO) tool, PSO@AutoDock, implemented in AutoDock 4.2 [89,90]. The AutoDockTools package was used to generate the docking input files and to analyze the docking results. The search algorithm varCPSO-ls from PSO@AutoDock implemented in AutoDock 4.2 was employed for docking calculations. Three-dimensional energy scoring grids with a resolution of 0.375 Å and dimensions of 120 Å × 120 Å × 120 Å were generated, covering the entire transmembrane domain. The parameters of the varCPSO-ls algorithm, including the cognitive coefficient (c1) and social coefficient (c2), were set to 6.05, with a swarm size of 60 individual particles. Default values were applied for all other parameters. A total of 50 independent docking runs were conducted for each transporter, with the termination criterion set at 50,000 evaluation steps. The docked poses for compound **57** were visually inspected, and the most plausible binding poses were selected for further analysis.

4.2.10. Spectroscopic analyses of selected hit compounds

The selected hit molecules compounds **15–16**, **18–20**, **53**, **57**, and **68**, as well as **31–32** were evaluated regarding their autofluorescence using a Paradigm microplate reader (Beckman Coulter, Brea, CA, USA) at excitation and emission wave lengths between 400 nm and 800 nm.

4.2.11. Data analysis and processing

All experiments were conducted independently at least three times. Percentage inhibition was calculated using either the reference inhibitors **80** (MCT1), **82** (ABCA1 and ABCB1), **83** (ABCC1), or **84** (ABCG2), or empty vector-transfected cells (NAT, DAT, SERT, OATP1A2, OATP1B1, OATP1B3, OATP2B1, and OCT1–3) in absorbance-based MTT assays (MCT1, MCT4, ABCC10), fluorescence-based assays (ABCB1, ABCC1, ABCG2, OATP1A2, OATP1B1, OATP1B3, OATP2B1, and OCT1–3), as well as mass spectrometry-based assays (NAT, DAT, SERT). Compounds that showed at least 20 % [+ standard error of the mean (SEM)] inhibition in the screenings were assessed at different concentrations and their IC_{50} values were calculated by non-linear regression using GraphPad Prism (version 8.4.0., San Diego, CA, USA) considering both three- and four-parameter logistic equations, whichever was statistically preferred. Curve fits have been performed as follows: (i) fit to bottom value of 0 % of control mean; (ii) free extrapolation to maximal inhibition given clearly indicated plateau of effect-concentrations; (iii) if no plateau given by the effect-concentrations, fit to 100 % of control mean. Data was used as normally distributed negative decadic logarithm of the IC_{50} (pIC_{50}) values, as calculated by GraphPad Prism. After calculation of the mean and SEM, the data was delogarithmized to obtain the final numeric representation as IC50, as described earlier [22].

CRediT authorship contribution statement

Katja Stefan: Writing – review & editing, Validation, Investigation, Formal analysis. **Sachin Puri:** Writing – review & editing, Validation, Investigation, Formal analysis. **Muhammad Rafehi:** Writing – review & editing, Writing – original draft, Visualization, Validation, Supervision, Resources, Methodology, Investigation, Funding acquisition, Formal analysis, Conceptualization. **Ganesh Latambale:** Investigation. **Maria Neif:** Investigation. **Franziska Tägl:** Writing – review & editing, Investigation. **Nike Sophia Arlt:** Investigation. **Zeinab Nezafat Yazdi:** Investigation. **Éva Bakos:** Investigation. **Xiang Chen:** Writing – review & editing, Investigation. **Bohan Zhang:** Investigation. **Wouroud Ismail Al-Khalil:** Writing – review & editing. **Hauke Busch:** Resources, Funding acquisition. **Zhe-Sheng Chen:** Resources. **Csilla Özvegy-Laczka:** Validation, Formal analysis. **Vigneshwaran Namasivayam:** Writing – review & editing, Visualization, Validation, Methodology, Funding acquisition. **Kapil Juvale:** Writing – review & editing, Writing – original draft, Validation, Supervision, Resources, Project administration, Methodology, Investigation, Funding acquisition, Formal analysis, Conceptualization. **Sven Marcel Stefan:** Writing – review & editing, Writing – original draft, Validation, Supervision, Resources, Project administration, Methodology, Investigation, Funding acquisition, Formal analysis, Conceptualization.

Declaration of competing interest

The authors declare no competing financial interests.

Declaration of competing interest

The authors declare that they have no known competing financial interests or personal relationships that could have appeared to influence the work reported in this paper.

Acknowledgements

Appendix A. Supporting data

Supplementary data to this article can be found online, which contain (i) Supplementary Table 1 summarizing molecular formula strings and the biological data in a CSV format; (iii) Supplementary Figs. 1–231 providing analytical data (FTIR, ^{1}H NMR, ^{13}C NMR, MS, HPLC) of compounds **15**–**79** (pdf); (ii) Supplementary Figs. 232–270 visualizing the biological results of the selected hit compounds **15**–**16**, **18**–**20**, **53**, **57**, and **68** as well as **31**–**32** (pdf).

Appendix B. Supplementary data

Supplementary data to this article can be found online at https://doi.org/10.1016/j.ejmech.2024.117234.

Data availability

Data will be made available on request.

References

[1] A.M. Torres, A.V. Dnyanmote, J.C. Granados, S.K. Nigam, Renal and non-renal response of ABC and SLC transporters in chronic kidney disease, Expert Opin Drug Metab Toxicol 17 (5) (2021) 515–542.
[2] S.B. Rosenthal, K.T. Bush, S.K. Nigam, A Network of SLC and ABC Transporter and DME genes involved in remote sensing and signaling in the gut-liver-kidney axis, Sci. Rep. 9 (1) (2019) 11879.
[3] S.B. Al Rihani, L.I. Darakjian, M. Deodhar, P. Dow, J. Turgeon, V. Michaud, Disease-induced modulation of drug transporters at the blood-brain barrier level, Int. J. Mol. Sci. 22 (7) (2021) 3742.
[4] L. Lin, S.W. Yee, R.B. Kim, K.M. Giacomini, SLC transporters as therapeutic targets: emerging opportunities, Nat. Rev. Drug Discov. 14 (8) (2015) 543–560.
[5] R. Januchowski, P. Zawierucha, M. Andrzejewska, M. Rucinski, M. Zabel, Microarray-based detection and expression analysis of ABC and SLC transporters in drug-resistant ovarian cancer cell lines, Biomed. Pharmacother. 67 (3) (2013) 240–245.
[6] Z. Ye, Y. Lu, T. Wu, The impact of ATP-binding cassette transporters on metabolic diseases, Nutr. Metab. 17 (2020) 61.
[7] A.M. Elkhatib, M. Omar, Ichthyosis Fetalis, StatPearls, Treasure Island (FL), 2023.
[8] I.K. Biji, S. Yadav, S. Kulshrestha, R. Saxena, S. Kohli, I.C. Verma, B. Kumar, R. D. Puri, Computational biology insights into genotype-clinical phenotype-protein phenotype relationships between novel SLC26A2 variants identified in inherited skeletal dysplasias, Eur. J. Med. Genet. 65 (10) (2022) 104595.
[9] H. Jiang, A. Alahmad, S. Fu, X. Fu, Z. Liu, X. Han, L. Li, T. Song, M. Xu, S. Liu, J. Wang, B. Albash, A. Alaqeel, V. Catalina, H. Prokisch, R.W. Taylor, R. McFarland, F. Fang, Identification and characterization of novel MPC1 gene variants causing mitochondrial pyruvate carrier deficiency, J. Inherit. Metab. Dis. (2021) 264–277.
[10] X. Zhang, X. Wu, H. Liu, T. Song, Y. Jiang, H. He, S. Yang, Y. Xie, Christianson syndrome: a novel splicing variant of SLC9A6 causes exon skipping in a Chinese boy and a literature review, J. Clin. Lab. Anal. 36 (1) (2022) e24123.
[11] H. Nofal, R. AlAkad, A. Nofal, E. Rabie, T. Chaikul, F.P. Chiu, R. Pramanik, A. Alabdulkareem, A. Onoufriadis, H syndrome: a review of treatment options and a hypothesis of phenotypic variability, Dermatol. Ther. 34 (5) (2021) e15082.
[12] F. Bisaccia, P. Koshal, V. Abruzzese, M.A. Castiglione Morelli, A. Ostuni, Structural and functional characterization of the ABCC6 transporter in hepatic cells: role on PXE, cancer therapy and drug resistance, Int. J. Mol. Sci. 22 (6) (2021) 2858.
[13] F.P.M. Cremers, W. Lee, R.W.J. Collin, R. Allikmets, Clinical spectrum, genetic complexity and therapeutic approaches for retinal disease caused by ABCA4 mutations, Prog. Retin. Eye Res. 79 (2020) 100861.
[14] A.J. Hooper, R.A. Hegele, J.R. Burnett, Tangier disease: Update for 2020, Curr. Opin. Lipidol. 31 (2) (2020) 80–84.
[15] B.R. Turk, C. Theda, A. Fatemi, A.B. Moser, X-linked adrenoleukodystrophy: pathology, pathophysiology, diagnostic testing, newborn screening and therapies, Int. J. Dev. Neurosci. 80 (1) (2020) 52–72.
[16] K. Tuschl, P.T. Clayton, S.M. Gospe Jr., S. Gulab, S. Ibrahim, P. Singhi, R. Aulakh, R.T. Ribeiro, O.G. Barsottini, M.S. Zaki, M.L. Del Rosario, S. Dyack, V. Price, A. Rideout, K. Gordon, R.A. Wevers, W.K. Chong, P.B. Mills, Syndrome of hepatic cirrhosis, dystonia, polycythemia, and hypermanganesemia caused by mutations in SLC30A10, a manganese transporter in man, Am. J. Hum. Genet. 90 (3) (2012) 457–466.
[17] V. Namasivayam, K. Silbermann, J. Pahnke, M. Wiese, S.M. Stefan, Scaffold fragmentation and substructure hopping reveal potential, robustness, and limits of computer-aided pattern analysis (C@PA), Comput. Struct. Biotechnol. J. 19 (2021) 3269–3283.
[18] W.W. Wang, L. Gallo, A. Jadhav, R. Hawkins, C.G. Parker, The druggability of solute carriers, J. Med. Chem. 63 (8) (2020) 3834–3867.
[19] S.M. Stefan, M. Rafehi, Medicinal polypharmacology-a scientific glossary of terminology and concepts, Front. Pharmacol. 15 (2024) 1419110.
[20] M. Rafehi, M. Möller, W. Ismail Al-Khalil, S.M. Stefan, Medicinal polypharmacology in the clinic - Translating the polypharmacolome into therapeutic benefit, Pharm. Res. (N. Y.) (2024) 411–417.
[21] S.M. Stefan, M. Rafehi, Medicinal polypharmacology: exploration and exploitation of the polypharmacolome in modern drug development, Drug Dev. Res. (2023) e22125.
[22] S.M. Stefan, P.J. Jansson, J. Pahnke, V. Namasivayam, A curated binary pattern multitarget dataset of focused ATP-binding cassette transporter inhibitors, Sci. Data 9 (1) (2022) 446.
[23] V. Namasivayam, K. Stefan, J. Pahnke, S.M. Stefan, Binding mode analysis of ABCA7 for the prediction of novel Alzheimer's disease therapeutics, Comput. Struct. Biotechnol. J. 19 (2021) 6490–6504.
[24] A. Ivanyuk, F. Livio, J. Biollaz, T. Buclin, Renal drug transporters and drug interactions, Clin. Pharmacokinet. 56 (8) (2017) 825–892.
[25] M. Karlgren, A. Vildhede, U. Norinder, J.R. Wisniewski, E. Kimoto, Y. Lai, U. Haglund, P. Artursson, Classification of inhibitors of hepatic organic anion transporting polypeptides (OATPs): influence of protein expression on drug-drug interactions, J. Med. Chem. 55 (10) (2012) 4740–4763.
[26] V. Namasivayam, K. Stefan, L. Gorecki, J. Korabecny, O. Soukup, P.J. Jansson, J. Pahnke, S.M. Stefan, Physicochemistry shapes bioactivity landscape of pan-ABC transporter modulators: Anchor point for innovative Alzheimer's disease therapeutics, Int. J. Biol. Macromol. 217 (2022) 775–791.
[27] J. Pahnke, P. Bascunana, M. Brackhan, K. Stefan, V. Namasivayam, R. Koldamova, J. Wu, L. Möhle, S.M. Stefan, Strategies to gain novel Alzheimer's disease diagnostics and therapeutics using modulators of ABCA transporters, Free Neuropathol 2 (2021) 33.
[28] V. Namasivayam, K. Stefan, K. Silbermann, J. Pahnke, M. Wiese, S.M. Stefan, Structural feature-driven pattern analysis for multitarget modulator landscapes, Bioinformatics 38 (5) (2022) 1385–1392.
[29] V. Mohos, E. Fliszar-Nyul, O. Ungvari, K. Kuffa, P.W. Needs, P.A. Kroon, A. Telbisz, C. Özvegy-Laczka, M. Poor, Inhibitory effects of quercetin and its main methyl, sulfate, and glucuronic acid conjugates on cytochrome P450 enzymes, and on OATP, BCRP and MRP2 transporters, Nutrients 12 (8) (2020) 2306.
[30] C. Ambrus, E. Bakos, B. Sarkadi, C. Özvegy-Laczka, A. Telbisz, Interactions of anti-COVID-19 drug candidates with hepatic transporters may cause liver toxicity and affect pharmacokinetics, Sci. Rep. 11 (1) (2021) 17810.
[31] O. Koch, Use of secondary structure element information in drug design: polypharmacology and conserved motifs in protein-ligand binding and protein-protein interfaces, Future Med. Chem. 3 (6) (2011) 699–708.
[32] N.V. Grishin, Fold change in evolution of protein structures, J. Struct. Biol. 134 (2–3) (2001) 167–185.
[33] R.B. Russell, P.D. Sasieni, M.J. Sternberg, Supersites within superfolds. Binding site similarity in the absence of homology, J. Mol. Biol. 282 (4) (1998) 903–918.

[34] J. Haupenthal, M. Rafehi, A.M. Kany, A. Lespine, K. Stefan, A.K.H. Hirsch, S. M. Stefan, Target repurposing unravels avermectins and derivatives as novel antibiotics inhibiting energy-coupling factor transporters (ECFTs), Arch. Pharm. (2024) e2400267.

[35] K. Stefan, V. Namasivayam, S.M. Stefan, Computer-aided pattern scoring - a multitarget dataset-driven workflow to predict ligands of orphan targets, Sci. Data 11 (1) (2024) 530.

[36] G.R. Velma, M.S. Laham, C. Lewandowski, A.C. Valencia-Olvera, D. Balu, A. Moore, M. Ackerman-Berrier, P. Rychetsky, C. Penton, S.R. Musku, A. Annadurai, M.I. Sulaiman, N. Ma, J.T. Gr, Nonlipogenic ABCA1 inducers (NLAI) for Alzheimer's disease validated in a mouse model expressing human APOE3/ APOE4, J. Med. Chem. 67 (17) (2024) 15061–15079.

[37] T. Heinrich, A. Sala-Hojman, R. Ferretti, C. Petersson, S. Minguzzi, A. Gondela, S. Ramaswamy, A. Bartosik, F. Czauderna, L. Crowley, P. Wahra, H. Schilke, P. Bopple, L. Dudek, M. Les, P. Niedziejko, K. Olech, H. Pawlik, L. Wloszczak, K. Zuchowicz, J.R. Suarez Alvarez, J. Martyka, E. Sitek, M. Mikulski, J. Szczesniak, S. Jackel, M. Krier, M. Krol, A. Wegener, M. Galezowski, M. Nowak, F. Becker, C. Herhaus, Discovery of 5-2-[5-chloro-2-(5-ethoxyquinoline-8-sulfonamido) phenyl]ethynyl-4-methoxypyridine-2-carboxylic acid, a highly selective in vivo useable chemical probe to dissect MCT4 Biology, J. Med. Chem. 64 (16) (2021) 11904–11933.

[38] S. Puri, K. Juvale, Monocarboxylate transporter 1 and 4 inhibitors as potential therapeutics for treating solid tumours: a review with structure-activity relationship insights, Eur. J. Med. Chem. 199 (2020) 112393.

[39] N. Hay, Reprogramming glucose metabolism in cancer: can it be exploited for cancer therapy? Nat. Rev. Cancer 16 (10) (2016) 635–649.

[40] C.N. Teijaro, S. Munagala, S. Zhao, G. Sirasani, P. Kokkonda, E.V. Malofeeva, E. Hopper-Borge, R.B. Andrade, Synthesis and biological evaluation of pentacyclic strychnos alkaloids as selective modulators of the ABCC10 (MRP7) efflux pump, J. Med. Chem. 57 (24) (2014) 10383–10390.

[41] Z.S. Chen, E. Hopper-Borge, M.G. Belinsky, I. Shchaveleva, E. Kotova, G.D. Kruh, Characterization of the transport properties of human multidrug resistance protein 7 (MRP7, ABCC10), Mol. Pharmacol. 63 (2) (2003) 351–358.

[42] D.Q. Chen, Y. Xie, L.Q. Cao, J.S. Fleishman, Y. Chen, T. Wu, D.H. Yang, The role of ABCC10/MRP7 in anti-cancer drug resistance and beyond, Drug Resist. Updates 73 (2024) 101062.

[43] S. Puri, K. Stefan, S.L. Khan, J. Pahnke, S.M. Stefan, K. Juvale, Indole derivatives as new structural class of potent and antiproliferative inhibitors of monocarboxylate transporter 1 (MCT1; SLC16A1), J. Med. Chem. 66 (1) (2023) 657–676.

[44] A.S.A.B.B. Snovydovych, Recent advances in the chemistry of indazoles, Eur. J. Org Chem. (24) (2008) 4073–4095, 2008.

[45] S.G. Zhang, C.G. Liang, W.H. Zhang, Recent Advances in indazole-containing derivatives: synthesis and biological perspectives, Molecules 23 (11) (2018) 2783.

[46] H. Shirahashi, E. Toriihara, Y. Suenaga, H. Yoshida, K. Akaogi, Y. Endou, M. Wakabayashi, M. Takashima, The discovery of novel 3-aryl-indazole derivatives as peripherally restricted pan-Trk inhibitors for the treatment of pain, Bioorg. Med. Chem. Lett. 29 (16) (2019) 2320–2326.

[47] E.J. Park, R. Park, J.H. Jeon, Y.Y. Cho, J.Y. Lee, H.C. Kang, I.S. Song, H.S. Lee, Inhibitory effect of AB-PINACA, indazole carboxamide synthetic cannabinoid, on human major drug-metabolizing enzymes and transporters, Pharmaceutics 12 (11) (2020) 1036.

[48] Y. Chen, R. Zhu, F. Ma, J. Mao, E.C. Chen, E.F. Choo, S. Sahasranaman, L. Liu, Assessment of OATP transporter-mediated drug-drug interaction using physiologically-based pharmacokinetic (PBPK) modeling - a case example, Biopharm. Drug Dispos. 39 (9) (2018) 420–430.

[49] L. Liu, S. Cheeti, K. Yoshida, E. Choo, E. Chen, B. Chen, M. Gates, S. Singel, R. Morley, J. Ware, S. Sahasranaman, Effect of OATP1B1/1B3 inhibitor GDC-0810 on the pharmacokinetics of pravastatin and coproporphyrin I/III in healthy female subjects, J. Clin. Pharmacol. 58 (11) (2018) 1427–1435.

[50] K.M. Logan, W. Kaplan, V. Simov, H. Zhou, D. Li, L. Torres, G.J. Morriello, J. J. Acton, B. Pio, Y.H. Chen, M.H. Keylor, R. Johnson, S.D. Kattar, R. Chau, X. Yan, M. Ardolino, C. Zarate, K.M. Otte, R.L. Palte, T. Xiong, S.E. McMinn, S. Lin, S. F. Neelamkavil, P. Liu, J. Su, L.G. Hegde, J.D. Woodhouse, L.Y. Moy, P.J. Ciaccio, J. Piesvaux, M. Zebisch, C. Henry, J. Barker, H.B. Wood, M.E. Kennedy, E. F. DiMauro, M.J. Fell, P.H. Fuller, Discovery and optimization of N-heteroaryl indazole LRRK2 inhibitors, J. Med. Chem. 67 (18) (2024) 16807–16819.

[51] G. Furlotti, M.A. Alisi, C. Apicella, A. Capezzone de Joannon, N. Cazzolla, R. Costi, G. Cuzzucoli Crucitti, B. Garrone, A. Iacovo, G. Magaro, G. Mangano, G. Miele, R. Ombrato, L. Pescatori, L. Polenzani, F. Rosi, M. Vitiello, R. Di Santo, Discovery and pharmacological profile of new 1H-indazole-3-carboxamide and 2H-pyrrolo [3,4-c]quinoline derivatives as selective serotonin 4 receptor ligands, J. Med. Chem. 55 (22) (2012) 9446–9466.

[52] B. Nancolas, L. Guo, R. Zhou, K. Nath, D.S. Nelson, D.B. Leeper, I.A. Blair, J. D. Glickson, A.P. Halestrap, The anti-tumour agent lonidamine is a potent inhibitor of the mitochondrial pyruvate carrier and plasma membrane monocarboxylate transporters, Biochem. J. 473 (7) (2016) 929–936.

[53] S. Puri, K. Juvale, Facile synthesis of new N1-alkylated 1H-indazole-3-carboxamide derivatives as potential anticancer agents: in vitro, ADMET prediction, and SAR studies, J. Mol. Struct. 1269 (2022) 133727.

[54] M.V. Sigalov, A.V. Afonin, I.V. Sterkhova, B.A. Shainyan, 2H-indazole tautomers stabilized by intra- and intermolecular hydrogen bonds, J. Org. Chem. 84 (14) (2019) 9075–9086.

[55] J. Clemens, E.L. Bell, A.T. Londregan, Selective N2-alkylation of 1H-indazoles and 1H-azaindazoles, Synthesis 54 (14) (2022) 3215–3226.

[56] L. Möhle, K. Stefan, P. Bascunana, M. Brackhan, T. Brüning, I. Eiriz, A. El Menuawy, S. van Genderen, I. Santos-Garcia, A.M. Gorska, M. Villa, J. Wu, S.

[57] M. Stefan, J. Pahnke, ABC transporter C1 prevents dimethyl fumarate from targeting Alzheimer's disease, Biology 12 (7) (2023) 932.

[57] V. Namasivayam, K. Silbermann, M. Wiese, J. Pahnke, S.M. Stefan, C@PA: computer-aided pattern analysis to predict multitarget ABC transporter inhibitors, J. Med. Chem. 64 (6) (2021) 3350–3366.

[58] K. Silbermann, J. Li, V. Namasivayam, S.M. Stefan, M. Wiese, Rational drug design of 6-substituted 4-anilino-2-phenylpyrimidines for exploration of novel ABCG2 binding site, Eur. J. Med. Chem. 212 (2021) 113045.

[59] K. Silbermann, J. Li, V. Namasivayam, F. Baltes, G. Bendas, S.M. Stefan, M. Wiese, Superior pyrimidine derivatives as selective ABCG2 inhibitors and broad-spectrum ABCB1, ABCC1, and ABCG2 antagonists, J. Med. Chem. 63 (18) (2020) 10412–10432.

[60] Y. Budagaga, Z. Sabet, Y. Zhang, E. Novotna, I. Hanke, T. Rozkos, J. Hofman, Tazemetostat synergistically combats multidrug resistance by the unique triple inhibition of ABCB1, ABCC1, and ABCG2 efflux transporters in vitro and ex vivo, Biochem. Pharmacol. 216 (2023) 115769.

[61] A. Morell, Y. Budagaga, D. Vagiannis, Y. Zhang, L. Lastovickova, E. Novotna, A. Haddad, M. Haddad, R. Portillo, J. Hofman, V. Wsol, Isocitrate dehydrogenase 2 inhibitor enasidenib synergizes daunorubicin cytotoxicity by targeting aldo-keto reductase 1C3 and ATP-binding cassette transporters, Arch. Toxicol. 96 (12) (2022) 3265–3277.

[62] O. Jensen, M. Rafehi, L. Gebauer, J. Brockmöller, Cellular uptake of psychostimulants - are high- and low-Affinity organic cation transporters drug traffickers? Front. Pharmacol. 11 (2020) 609811.

[63] M. Poor, H. Kaci, S. Bodnarova, V. Mohos, E. Fliszar-Nyul, S. Kunsagi-Mate, C. Ozvegy-Laczka, B. Lemli, Interactions of resveratrol and its metabolites (resveratrol-3-sulfate, resveratrol-3-glucuronide, and dihydroresveratrol) with serum albumin, cytochrome P450 enzymes, and OATP transporters, Biomed. Pharmacother. 151 (2022) 113136.

[64] L. Gebauer, O. Jensen, M. Rafehi, J. Brockmöller, Stereoselective inhibition of high- and low-affinity organic cation transporters, Mol. Pharm. 20 (12) (2023) 6289–6300.

[65] E. Bakos, O. Nemet, I. Patik, N. Kucsma, G. Varady, G. Szakacs, C. Özvegy-Laczka, A novel fluorescence-based functional assay for human OATP1A2 and OATP1C1 identifies interaction between third-generation P-gp inhibitors and OATP1A2, FEBS J. 287 (12) (2020) 2468–2485.

[66] K. Stefan, S.M. Schmitt, M. Wiese, 9-Deazapurines as broad-spectrum inhibitors of the ABC transport proteins P-glycoprotein, multidrug resistance-associated protein 1, and breast cancer resistance protein, J. Med. Chem. 60 (21) (2017) 8758–8780.

[67] N. Wang, X. Jiang, S. Zhang, A. Zhu, Y. Yuan, H. Xu, J. Lei, C. Yan, Structural basis of human monocarboxylate transporter 1 inhibition by anti-cancer drug candidates, Cell 184 (2) (2021) 370–383.

[68] S. Urgaonkar, K. Nosol, A.M. Said, N.N. Nasief, Y. Bu, K.P. Locher, J.Y.N. Lau, M. P. Smolinski, Discovery and characterization of potent dual P-glycoprotein and CYP3A4 inhibitors: design, synthesis, cryo-EM analysis, and biological evaluations, J. Med. Chem. 65 (1) (2022) 191–216.

[69] H.L. Pietz, A. Abbas, Z.L. Johnson, M.L. Oldham, H. Suga, J. Chen, A macrocyclic peptide inhibitor traps MRP1 in a catalytically incompetent conformation, Proc. Natl. Acad. Sci. U. S. A. 120 (11) (2023) e2220012120.

[70] A. Rasouli, Q. Yu, S. Dehghani-Ghahnaviyeh, P.C. Wen, J. Kowal, K.P. Locher, E. Tajkhorshid, Differential dynamics and direct interaction of bound ligands with lipids in multidrug transporter ABCG2, Proc. Natl. Acad. Sci. U. S. A. 120 (1) (2023) e2213437120.

[71] Z. Shan, X. Yang, H. Liu, Y. Yuan, Y. Xiao, J. Nan, W. Zhang, W. Song, J. Wang, F. Wei, Y. Zhang, Cryo-EM structures of human organic anion transporting polypeptide OATP1B1, Cell Res. 33 (12) (2023) 940–951.

[72] A.D. Ciuta, K. Nosol, J. Kowal, S. Mukherjee, A.S. Ramirez, B. Stieger, A. A. Kossiakoff, K.P. Locher, Structure of human drug transporters OATP1B1 and OATP1B3, Nat. Commun. 14 (1) (2023) 5774.

[73] Y. Suo, N.J. Wright, H. Guterres, J.G. Fedor, K.J. Butay, M.J. Borgnia, W. Im, S. Y. Lee, Molecular basis of polyspecific drug and xenobiotic recognition by OCT1 and OCT2, Nat. Struct. Mol. Biol. 30 (7) (2023) 1001–1011.

[74] B. Khanppnavar, J. Maier, F. Herborg, R. Gradisch, E. Lazzarin, D. Luethi, J. W. Yang, C. Qi, M. Holy, K. Jantsch, O. Kudlacek, K. Schicker, T. Werge, U. Gether, T. Stockner, V.M. Korkhov, H.H. Sitte, Structural basis of organic cation transporter-3 inhibition, Nat. Commun. 13 (1) (2022) 6714.

[75] A.M. Plummer-Medeiros, A.T. Culbertson, C.L. Morales-Perez, M. Liao, Activity and structural dynamics of human ABCA1 in a lipid membrane, J. Mol. Biol. 435 (8) (2023) 168038.

[76] R.R. Schulte, R.H. Ho, Organic anion transporting polypeptides: emerging roles in cancer pharmacology, Mol. Pharmacol. 95 (5) (2019) 490–506.

[77] N. Brosseau, D. Ramotar, The human organic cation transporter OCT1 and its role as a target for drug responses, Drug Metab. Rev. 51 (4) (2019) 389–407.

[78] M. Heise, A. Lautem, J. Knapstein, J.M. Schattenberg, M. Hoppe-Lotichius, D. Foltys, N. Weiler, A. Zimmermann, A. Schad, D. Grundemann, G. Otto, P. R. Galle, M. Schuchmann, T. Zimmermann, Downregulation of organic cation transporters OCT1 (SLC22A1) and OCT3 (SLC22A3) in human hepatocellular carcinoma and their prognostic significance, BMC Cancer 12 (2012) 109.

[79] A. Bacq, L. Balasse, G. Biala, B. Guiard, A.M. Gardier, A. Schinkel, F. Louis, V. Vialou, M.P. Martres, C. Chevarin, M. Hamon, B. Giros, S. Gautron, Organic cation transporter 2 controls brain norepinephrine and serotonin clearance and antidepressant response, Mol. Psychiatr. 17 (9) (2012) 926–939.

[80] T. Wultsch, G. Grimberg, A. Schmitt, E. Painsipp, H. Wetzstein, A.F. Breitenkamp, D. Grundemann, E. Schomig, K.P. Lesch, M. Gerlach, A. Reif, Decreased anxiety in mice lacking the organic cation transporter 3, J. Neural. Transm. 116 (6) (2009) 689–697.

[81] C.S. Swenson, G. Mandava, D.M. Thomas, R.E. Moellering, Tackling undruggable targets with designer peptidomimetics and synthetic biologics, Chem. Rev. 124 (22) (2024) 13020–13093.

[82] S. Chakraborty, A.R. Paul, S. Majumdar, Base and metal free true recyclable medium for Knoevenagel condensation reaction in SDS-ionic liquid-aqueous miceller composite system, Results in Chemistry 4 (2022) 100294.

[83] L. Gebauer, N. Arul Murugan, O. Jensen, J. Brockmöller, M. Rafehi, Molecular basis for stereoselective transport of fenoterol by the organic cation transporters 1 and 2, Biochem. Pharmacol. 197 (2021) 114871.

[84] I. Patik, V. Szekely, O. Nemet, A. Szepesi, N. Kucsma, G. Varady, G. Szakacs, E. Bakos, C. Özvegy-Laczka, Identification of novel cell-impermeant fluorescent substrates for testing the function and drug interaction of organic anion-transporting polypeptides, OATP1B1/1B3 and 2B1, Sci. Rep. 8 (1) (2018) 2630.

[85] J.Q. Wang, Z.X. Wu, Y. Yang, J.S. Li, D.H. Yang, Y.F. Fan, Z.S. Chen, Establishment and characterization of a novel multidrug resistant human ovarian cancer cell line with heterogenous MRP7 overexpression, Front. Oncol. 11 (2021) 731260.

[86] H.M. Berman, J. Westbrook, Z. Feng, G. Gilliland, T.N. Bhat, H. Weissig, I. N. Shindyalov, P.E. Bourne, The protein data bank, Nucleic Acids Res. 28 (1) (2000) 235–242.

[87] Molecular Operating Environment (MOE), version 2022.02, Chemical Computing Group: Montreal, Quebec, Canada.

[88] J.C. Wang, P, P.A. Kollman, How well does a restrained electrostatic potential (RESP) model perform in calculating conformational energies of organic and biological molecules? J. Comput. Chem. 21 (12) (2000) 1049–1074.

[89] G.M. Morris, R. Huey, W. Lindstrom, M.F. Sanner, R.K. Belew, D.S. Goodsell, A. J. Olson, AutoDock4 and AutoDockTools4: automated docking with selective receptor flexibility, J. Comput. Chem. 30 (16) (2009) 2785–2791.

[90] V. Namasivayam, R. Gunther, pso@autodock: a fast flexible molecular docking program based on swarm intelligence, Chem. Biol. Drug Des. 70 (6) (2007) 475–484.